Charge-neutral muon centers in magnetic and non-magnetic materials: implications and applications

by

Martin Herbert Dehn

B. Sc. (Physics), Technische Universität München, 2013

M. Sc. (Physics), Technische Universität München, 2016

A THESIS SUBMITTED IN PARTIAL FULFILLMENT

OF THE REQUIREMENTS FOR THE DEGREE OF

DOCTOR OF PHILOSOPHY

in

THE FACULTY OF GRADUATE AND POSTDOCTORAL STUDIES

(Physics)

The University of British Columbia

(Vancouver)

October 2021

The following individuals certify that they have read, and recommend to the Faculty of Graduate and Postdoctoral Studies for acceptance, the thesis entitled:

Charge-neutral muon centers in magnetic and non-magnetic materials: implications and applications

submitted by **Martin Herbert Dehn** in partial fulfillment of the requirements for the degree of **Doctor of Philosophy** in **Physics**.

Examining Committee:

Robert F. Kiefl, Department of Physics and Astronomy, University of British Columbia
Research Supervisor

W. Andrew MacFarlane, Department of Chemistry, University of British Columbia
Co-Supervisor

Mona I. Berciu, Department of Physics and Astronomy, University of British Columbia
Supervisory Committee Member

Joshua A. Folk, Department of Physics and Astronomy, University of British Columbia
University Examiner

Edward R. Grant, Department of Chemistry, University of British Columbia
University Examiner

Roberto De Renzi, Department of Mathematical, Physical and Computer Sciences, Università di Parma
External Examiner

Additional Supervisory Committee Members:

Alireza Nojeh, Department of Electrical and Computer Engineering, University of British Columbia
Supervisory Committee Member

Ariel R. Zhitnitsky, Department of Physics and Astronomy, University of British Columbia
Supervisory Committee Member

Abstract

Spin polarized muons are widely known as extremely sensitive local probes of magnetism. Muon spin rotation (μSR) spectroscopy has made key contributions in the study of complex condensed matter systems such as frustrated and dilute magnetic systems and superconductors. Additionally, positively charged muons implanted into semiconductors and insulators often bind an electron to form muonium (Mu $= [\mu^+ e^-]$), a charge-neutral muon-electron bound state. Muonium has been studied extensively in a wide range of semiconducting and insulating materials, motivated by the fact that its electronic structure inside a material is virtually identical to that of isolated hydrogen defects, one of the most ubiquitous impurities in semiconductors. However, such measurements are thought to be limited to non-magnetic compounds; in magnetic materials, muonium is widely assumed to be unobservable, and charge-neutral muon states are generally not considered relevant.

Here, we present strong evidence that charge-neutral muon centers *do* exist in magnetic compounds. Detailed μSR investigations of the prototypical antiferromagnets Cr_2O_3, Fe_2O_3 and MnF_2 reveal that charge-neutral muon states can form and take on different shapes, including muon-polaron complexes and interstitial centers with large muon-electron hyperfine coupling. Crucially, we find that in magnetic materials, charge-neutral muon states do not display any signatures conventionally associated with muonium, effectively "hiding" their presence. Despite their inconspicuous signals, charge-neutral centers can significantly change how the muons interact with their host material and thus significantly alter the μSR signals. In addition, we clearly demonstrate for MnF_2 that the charge-state of the muon and the magnetic properties measured by μSR are closely related, and both aspects have to be considered when using μSR to determine the intrinsic magnetic properties. These results indicate that μSR may be useful to study not only the *electronic* impact of hydrogen defects, but also their role as *magnetic* impurities in non-conductive magnetic compounds.

For comparison, we also investigate charge-neutral muon-polaron complexes in non-magnetic TiO_2 as well as vacuum-like muonium diffusing through the voids of an amorphous silica aerogel. These examples are used to highlight the differences and similarities between charge-neutral muon states in magnetic and non-magnetic materials.

Lay Summary

Spin-polarized beams of muons μ^+, short-lived elementary particles that can be thought of as light-weight protons, are a powerful tool to study material properties, and are frequently used to investigate magnetic compounds. In addition, in semiconductors, muons often capture an electron to form a muon-electron bound state called muonium (μ^+e^-), which can be used as an analogue for hydrogen, one of the most important and elusive impurities in semiconductors. However, the study of magnetism and muonium are considered separate fields with little overlap; muonium is widely assumed to be unimportant in magnetic materials. In this thesis, we challenge this assumption and present strong evidence that muonium-like muon-electron bound states do exist in magnetic materials and significantly influence the observed signals. Crucially however, they do not display any signatures conventionally associated with muonium, concealing their presence. The implications and possibilities for the study of magnetic materials with muons are discussed.

Preface

A version of Chapter 3 (with exception of the theory review in Sec. 3.2) has been published:

- M. H. Dehn, R. Scheuermann, P.-X. Wang, Y. Cao, M. J. MacLachlan, V. M. Zamarion, D. G. Fleming, and R. F. Kiefl: Precision measurement of the muonium hyperfine interaction in mesoporous silica and aerogel" *Phys. Rev. Research* **3**, 013029 (2021)

Only one of two samples covered in this paper were included in this thesis for the sake of simplicity and brevity. The data was taken in 2015 (prior to the start of my PhD) at the Paul-Scherrer-Institute (PSI) in Switzerland by R. Scheuermann as part of a feasibility test. The μSR spectra were analyzed by R. Scheuermann. R. F. Kiefl and I analyzed and interpreted the fit results and wrote the manuscript in consultation with R. Scheuermann.

The data presented in Chapter 4 is unpublished. The rotatable sample holder was designed by me in consultation with G. D. Morris and R. F. Kiefl; M. McLay did the technical drawing. The experiment was conceived and designed by me in consultation with R. F. Kiefl. The data was taken by me with the help of TRIUMF scientists D. J. Arseneau and G. D. Morris. I analyzed and interpreted the data and wrote Chapter 4 which will form the basis for a manuscript. J. K. Shenton and R. F. Kiefl contributed to the discussion and the interpretation. I gratefully acknowledge a discussion with R. C. Vilao.

A version of Chapter 5 has been published

- M. H. Dehn, J. K. Shenton, S. Holenstein, Q. N. Meier, D. J. Arseneau, D. L. Cortie, B. Hitti, A. C. Y. Fang, W. A. MacFarlane, R. M. L. McFadden, G. D. Morris, Z. Salman, H. Luetkens, N. A. Spaldin, M. Fechner, and R. F. Kiefl: "Observation of a charge-neutral muon-polaron complex in antiferromagnetic Cr_2O_3" *Phys. Rev. X* 10, 011036 (2020)

Preliminary data was taken at PSI by S. Holenstein, M. Fechner, Z. Salman and H. Luetkens. The data shown here and in the publication were taken by me at TRIUMF with the help of TRIUMF scientists D. J. Arseneau, G. D. Morris and B. Hitti over several beamtimes with some initial involvement from D. L. Cortie and R. M. L. McFadden. I performed the data analysis and interpreted the data with the help of various models and simulations in consultation with R. F. Kiefl. J. K. Shenton did the DFT calculations. Experimental and theoretical results were discussed and interpreted by me and J. K.

Shenton in consultation with R. F. Kiefl and N. A. Spaldin. I wrote the manuscript, with contributions regarding the details of the DFT calculations and DFT-related figures from J. K. Shenton, with feedback from R. F. Kiefl, J. K. Shenton and N. A. Spaldin and most co-authors.

A version of Chapter 6 has been published:

- M. H. Dehn*, J. K. Shenton*, D. J. Arseneau, W. A. MacFarlane, G. D. Morris, A. Maigne, N. A. Spaldin, and R.F. Kiefl: "Local electronic structure and dynamics of muon-polaron complexes in Fe_2O_3" *Phys. Rev. Lett.* **126**, 037202 (2021) * authors contributed equally

This research was conceived and planned by me and R. F. Kiefl. The data was taken by me at TRIUMF with the help of D. J. Arseneau and G. D. Morris. I analyzed the data and modeled and simulated the dynamical processes. J. K. Shenton carried out the DFT calculations. Experimental and theoretical results were discussed and interpreted by me and J. K. Shenton in consultation with R. F. Kiefl and N. A. Spaldin. I wrote the manuscript, with contributions regarding the details of the DFT calculations and DFT-related figures from J. K. Shenton, with feedback from R. F. Kiefl, J. K. Shenton and N. A. Spaldin and most co-authors.

In Chapter 7 is unpublished, a manuscript based on the chapter is currently being prepared. This research was conceived and planned by me and R. F. Kiefl. The data was taken at PSI (Switzerland) by R. Scheuermann with the help of A. Suter and Z. Guguchia; personal attendance was discouraged by travel restriction due to the Covid-19 pandemic. I analyzed the data, interpreted it and wrote Chapter 7 in consultation with R. F. Kiefl, R. Scheuermann, J. K. Shenton, N. A. Spaldin and A. Suter.

The respective publishers grant permission for this material to be incorporated into this thesis.

Table of Contents

List of Tables

List of Figures

Acknowledgments

The work presented in this thesis benefited tremendously from the willingness of a great number of people to work collaboratively, share their knowledge and discuss ideas. Thank you.

First and foremost, I thank my wonderful supervisor Rob Kiefl, for his contagious enthusiasm and genuine excitement about our research, his invaluable insights, and for guidance and support while giving me the freedom to pursue various ideas and directions. I will miss our discussions and the laughter.

I am also thankful to my second supervisor Andrew MacFarlane, for valuable feedback and always being open for discussions, especially with regards to β-NMR projects. I would also like to thank the remaining committee members: Mona Berciu, Alireza Nojeh and Erik Zhitnitsky, for their feedback and support, and for taking the time to read this thesis.

I am very grateful to Don Fleming for his support, advice, and the many loud and fun discussions about science and politics. I will fondly remember our dinners at ISIS-RAL.

This thesis would look very different without the great collaboration with Nicola Spaldin's materials theory group at ETHZ, in particular Kane Shenton. Kane's DFT calculations were enormously helpful for the interpretation of the μSR data, and I happily acknowledge our countless discussions trying to figure out what's going on in both experiment and theory. I am also very thankful to Nicola for many insightful discussions, her positive feedback and support, and welcoming me twice in Zurich.

Special thanks to Robert Scheuermann at PSI, who took the data on the silica aerogel as part of an unexpectedly successful feasibility test, and who also took the MnF_2 data when travel to Switzerland was made difficult due to the Covid-19 pandemic; our many discussions are much appreciated. I also thank Andreas Suter and Zurab Guguchia for their help with the MnF_2 project, and Steve Blundell and Dharmalingam Prabhakaran for the MnF_2 single crystal.

"*What could possibly go wrong?*" I am indebted to the staff at the TRIUMF Center for Molecular and Material Science (CMMS), in particular Gerald Morris, Bassam Hitti and Donald Arseneau, for their incredible willingness to help and teach, assist with uncooperative beamlines, blocked cryostats, broken power supplies and experimental setups until very late at night, and for lending their expertise with the design and commissioning of experimental setups. Many thanks to Deepak Vyas and Rahim Abasalti for excellent technical support, and Mike McLay for all the technical drawings. I am also very grateful to Sarah Dunsiger, for teaching me my first steps in μSR and remaining a source of expertise and support ever since.

I would like to thank my present and former colleagues in the extended μSR and βNMR group: Ryan McFadden, Derek Fujimoto, David Cortie, Monika Stachura, John Ticknor, Victoria Kramer, Aris Chatzichristos, Alex Fang, Iain McKenzie and Kenji Kojima, for many fun and interesting conversations, advice and help with experiments.

I happily and gratefully acknowledge collaborators, including those involved in projects that are not included in this thesis: Alan Maigné for the EDX measurements on Fe_2O_3, Allanah Hallas for the pyrochlore samples, Bruce Davidson for the collaboration on strained $SrTiO_3$ films, Mark MacLachlan, Peixi Wang and Yuanyuan Cao for the silica samples, Steve Cottrell for the help with the RF-μSR study, Seyed Koohpayeh for the TiO_2 single crystal, and Stefan Holenstein, Michael Fechner, Zaher Salman and Hubertus Luetkens for sharing the Cr_2O_3 data. I also thank Rui Vilão for serveral stimulating discussions, and Johannes Herms for patient particle physics explanations.

Thanks to my close friends, both in Vancouver and abroad, for showing their interest and support, and taking my mind off of research. Special thanks to my cat for keeping me sane(ish) while writing this thesis from home during the Covid-19 pandemic. I would also like to thank my siblings and parents for their unconditional support and encouragement. Finally, I thank my partner Lisa for her unwavering support and love.

Chapter 1

Introduction

It seems possible that polarized positive and negative muons will become a powerful tool for exploring magnetic fields in nuclei [...], atoms and interatomic regions.
— R. L. Garwin *et al.*, *Physical Review* **105** 1415 (1957) [1]

This thesis reports on a novel investigation on how spin-polarized positive muons μ^+ interact with their local environment when implanted into non-conductive magnetic compounds. Muons are structureless spin-$\frac{1}{2}$ particles with a mass of $105.7\,\mathrm{MeV/c^2}$, about $\frac{1}{9}$ the mass of a proton or 207 times the mass of an electron. There are both positive and negative muons; this thesis, like most condensed matter applications, exclusively makes use of the positive muon μ^+. Muons are short-lived and decay with a mean lifetime of $\tau \approx 2.2\,\mu$s into two neutrinos and a positron:

$$\mu^+ \rightarrow \bar{\nu}_\mu + \nu_e + e^+ \tag{1.1}$$

This decay is governed by the weak interaction, which violates parity [2, 3], i.e the notion that every process in nature has a mirror process with equal probability. As an important consequence, the positron is not emitted isotropically, but preferentially *along* the muon spin direction, with an angular emission probability $P(\theta)$ proportional to

$$P(\theta) \propto 1 + a\cos(\theta), \tag{1.2}$$

where θ is the emission angle with respect to the muon spin and a is the decay anisotropy, see Fig. 1.1. Averaging over the range of positron energies possible for the three-body decay of the muon, a is found to be close to $\frac{1}{3}$ [1, 4]; twice as many positrons are emitted along ($\theta = 0°$) rather than opposite ($\theta = 180°$) to the muon spin. This anisotropic positron emission, first reported by Garwin *et al.* in 1957 [1], enables in principle the measurement of the spin polarization of an *ensemble* of polarized muons. Unlike positrons, neutrinos, (almost) massless spin-$\frac{1}{2}$ particles with no electric charge, hardly interact with matter and cannot be observed in the context of the experiments described in this thesis.

The muon was first discovered in cosmic radiation [5, 6]: high-energy protons hit the upper atmosphere of the earth and create pions [7, 8], spin-less ($S = 0$) particles which subsequently decay via the

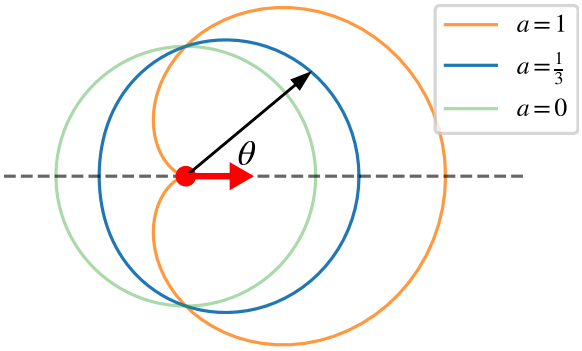

Figure 1.1: Anisotropic muon decay: the decay positron is emitted preferentially in the direction of the muon spin (red). The emission probability is proportional to $1+a\cos(\theta)$ (solid lines), where a is the decay anisotropy.

weak interaction into a muon and a neutrino:

$$\pi^+ \rightarrow \nu_\mu + \mu^+. \tag{1.3}$$

This two-body decay also violates parity; in fact, the weak interaction couples *only* to neutrinos with left-handed helicity, i.e. the neutrino spin vector projected on the direction of motion is always opposite to it ($m_s = -\frac{1}{2}$) [9–11]. In the rest-frame of the spin-0 pion, the muon and neutrino are emitted in opposite directions, and since the neutrino spin is always $m_s = -\frac{1}{2}$, conservation of angular momentum dictates that the muon spin is also *always* $m_s = -\frac{1}{2}$, i.e. opposite to its direction of motion. This process can be re-created in the lab to create a beam of almost fully spin-polarized muons: high-energy ($\geq 500\,\mathrm{MeV}$) protons are guided into a target of typically graphite or beryllium, creating large numbers of pions. Those muons that come from pions that decay at rest close to the target surface, so-called *surface muons*, have their spin opposite to their direction of motion; by selecting muons emitted in a certain direction, a nearly 100% spin-polarized muon beam can be formed. As recognized by Garwin *et al.* (see introductory quote), the ability to (1) *create* polarized muon beams and (2) *measure* the spin polarization via the anisotropic muon decay renders the muon a powerful tool to explore the magnetic fields *inside* materials: after implantation, the muon comes to rest on a short time scale ($< 100\,\mathrm{ps}$), and its spin evolves in its local magnetic environment, causing a time dependence of the spin polarization which can be measured and used to infer magnetic properties.

This forms the basis of muon spin spectroscopy or μSR, with the acronym standing for muon spin **r**otation, **r**elaxation and **r**esonance, covering different aspects of this technique [see e.g. Refs. [12, 13]]. Two major sub-fields emerged. On the one hand, μSR was developed into a sensitive probe[1] for magnetism [13–15] and superconductivity [16–21], including quantum phase transitions [22–24] and exotic forms of magnetism such as frustration and quantum spin ice [25–27], dilute spin systems [28],

[1] This sensitivity stems in part from the large muon magnetic moment, which is ~ 3.18 times larger than that of a proton

molecular magnets [29] and heavy fermion systems [30].

On the other hand, there is the study of muonium (Mu $= [\mu^+ e^-]$), an overall charge-neutral muon-electron bound state first discovered by Hughes *et al.* in 1960 [31]. Since the positive muon has the same charge and spin as a proton, and is much closer in mass to the proton than to the electron ($m_\mu \approx \frac{1}{9} m_p \approx 207 m_e$), Mu in vacuum closely resembles hydrogen - in fact, since the reduced mass of the electron is almost the same (within 0.5 %) for hydrogen and muonium, the electronic structure of the two systems, as well as the Bohr radius and binding energies, are virtually the same. This close correspondence makes Mu a unique probe for chemistry, allowing e.g. the study of isotope effects [32–35]. Furthermore, Mu also forms in most non-magnetic semiconductors and insulators, where it is conventionally referred to as a *paramagnetic* center since the bound electron is unpaired and its spin is only weakly coupled to the lattice. Importantly, the muon-proton analogy extends to charge-neutral centers *inside* materials. This is relevant since hydrogen is one of the most ubiquitous impurities in semiconductors [36–38], and can significantly influence their electronic properties. However, direct measurements of the electronic structure of isolated hydrogen defects in semiconductors are challenging due to their high reactivity with other defects, which is why most available information comes from the study of their Mu analogue. Consequently, Mu has been studied extensively to obtain detailed information on the dopant characteristics of isolated hydrogen defects in a wide range of non-conductive materials [39–42]. In contrast, Mu is generally not found in metals, since the positive muon is screened by and interacts with many conduction band electrons such that bound states with individual electrons are not possible.[2]

In the early days of μSR, the question was posed whether charge-neutral Mu centers also form in *magnetic* materials such as antiferromagnetic Fe_2O_3 [44]. However, no evidence for Mu formation was found with the singular exception of MnF_2 [45], where Uemura *et al.* observed a signal that could only be explained with a charge-neutral muon center. However, given the complete lack of evidence for paramagnetic Mu in other materials, charge-neutral centers are widely assumed to either simply not form or rapidly depolarize in the presence of magnetic moments [15, 41]. As a result, the possibility of charge-neutral muon states is generally not considered when interpreting μSR spectra taken in magnetic materials - the study of magnetism with μSR is largely considered to be an entirely separate field from research on paramagnetic Mu centers in non-magnetic materials, co-existing without significant overlap.

In this thesis, we present strong evidence that charge-neutral centers *do* exist in several magnetic semiconductors and insulators, suggesting that they are as prevalent in magnetic compounds as they are in non-magnetic materials. However, a crucial difference compared to Mu in non-magnetic semiconductors and insulators is that charge-neutral centers in magnetic compounds are *not paramagnetic* and therefore *distinct* from Mu, since the bound electron is strongly coupled to the unpaired electrons of the magnetic host. Therefore, no signatures conventionally associated with a charge-neutral state (i.e. paramagnetic Mu) are evident, which makes their identification difficult. We show that despite its inconspicuous signal, the formation of a charge-neutral center can significantly change how the muon

[2] Exceptions do exist, for example endohedral Mu in fullerene metals [43].

interacts with its host material; location and stability of the muon stopping sites, spin depolarization rates as well as the magnitude and temperature dependence of local magnetic fields - in short, all relevant μSR observables - are potentially affected. We demonstrate that the charge-state of the muon and the magnetic properties measured by μSR can be intricately intertwined, and both aspects should be considered when using μSR data to determine magnetic properties of the host.

This thesis is organized as follows: In **Chapter 2**, the method of time-differential μSR is introduced, and the general theoretical framework necessary to discuss the implications of the muon-electron coupling in charge-neutral muon states is presented. Next, in **Chapter 3**, the theory of Mu in vacuum is discussed. Analogous to hydrogen, the electron is in an 1s-orbital centered on the muon, which is why this *isotropic* Mu center is the simplest case of a charge-neutral muon state. As an example, we briefly present a study of Mu diffusing through the voids of an amorphous silica aerogel. Then, in **Chapter 4**, we explore paramagnetic Mu centers formed *inside* materials, where the electron wave-function can be significantly more complex and can take various shapes. As a result, the muon-electron coupling has in general an *anisotropic* contribution, the theoretical implications and experimental signatures of which are discussed. We then focus on the transition metal oxide TiO_2, in which the charge-neutral muon center is reported to take on a peculiar form: rather than centering on the muon, the bound electron localizes on a nearby Ti ion to from an overall charge-neutral muon-polaron complex [46–48]. We present and discuss a new detailed μSR study of the fully anisotropic charge-neutral muon center in TiO_2, which was motivated by several open questions regarding its precise electronic structure. **Chapter 5** reports a comprehensive μSR study of the antiferromagnetic transition metal oxide Cr_2O_3. We find the muon occupies several distinct interstitial sites, and displays a rich dynamic behavior involving local hopping, thermally activated site transitions and, importantly, the formation of a charge-neutral muon-polaron complex similar to that observed in non-magnetic TiO_2. Crucially, this charge-neutral muon state is *not paramagnetic* and therefore does not display signatures expected for Mu in non-magnetic compounds; nonetheless, it has a significant impact on the observed spectra. The discovery of this complex suggests charge-neutral muon centers can form in other magnetic compounds as well, which has implications for the interpretation of μSR spectra in a wide range of materials. Indeed, as we show in **Chapter 6**, there is strong evidence for charge-neutral muon-polaron complexes in antiferromagnetic Fe_2O_3 as well. In contrast to Cr_2O_3, we identify several muon-polaron complex configurations that are very close in energy and thus thermally accessible to the muon. This enables rapid transitions between various complex configurations, which has a significant impact on the measured μSR frequencies and depolarization rates. In **Chapter 7**, having established the presence of charge-neutral muon states in Cr_2O_3 and Fe_2O_3, we return to MnF_2, thus far the only published example of a magnetic material where any conclusive evidence for a charge-neutral center was reported. In new detailed μSR measurements, we investigate the charge-neutral center, and demonstrate that the presence of the additional charge significantly perturbs the local magnetic environment such that the μSR signal does not reflect the intrinsic magnetic properties. Lastly, in **Chapter 8**, the main findings and their implications for the interpretation of μSR spectra in magnetic semiconductors and insulators are summarized, and further work is suggested.

Chapter 2

Introduction to muon spin rotation

In this chapter, we first discuss a spin 1/2 particle in an applied magnetic field in order to introduce both the necessary terminology and the concept of spin precession. Then, we describe the principles of a μSR experiment and explain how the time-dependent muon spin polarization can be experimentally observed. Lastly, we present the theoretical framework for coupled spin systems, which forms the basis for discussing muon-electron bound states, i.e. muon centers where there is an additional electron in close vicinity to the implanted muon, forming an overall charge-neutral center.

2.1 Spin 1/2 particle in a magnetic field

To start, we consider the muon in the presence of a magnetic field $\mathbf{B}$, which interacts with the muon magnetic moment $\mathbf{m} = \gamma_\mu \mathbf{S} = \frac{\hbar}{2}\gamma_\mu \boldsymbol{\sigma}$. Here, $\gamma_\mu = 2\pi \cdot 135.5\,\mathrm{MHz/T}$ is the muon gyromagnetic moment and $\mathbf{S} = \frac{1}{2}\hbar\boldsymbol{\sigma}$ is the spin operator, expressed in Pauli spin matrices $\boldsymbol{\sigma} = \begin{pmatrix}\sigma_x\\ \sigma_y\\ \sigma_z\end{pmatrix}$. This system can be described by the Zeeman Hamiltonian [see for example Ref. [49]]

$$\mathrm{H} = -\mathbf{m}\cdot\mathbf{B} = -\frac{\hbar}{2}\gamma_\mu \boldsymbol{\sigma}\cdot\mathbf{B} = -\frac{\hbar}{2}\gamma_\mu(\sigma_x B_x + \sigma_y B_y + \sigma_z B_z) = -\frac{\hbar}{2}\gamma_\mu \begin{pmatrix} B_z & B_x - \mathrm{i}B_y \\ B_x + \mathrm{i}B_y & -B_z \end{pmatrix}, \tag{2.1}$$

where the spin operators and thus H are expressed in the following basis of the form $|S_z\rangle$: $|\uparrow\rangle = \binom{1}{0}$, $|\downarrow\rangle = \binom{0}{1}$. Typically, $\mathbf{B}$ is chosen along $\hat{z}$, and two different initial muon spin polarizations $\mathbf{P}_i$ are considered, either $\left|\Psi^\mu_{\mathrm{LF}}(0)\right\rangle = \binom{1}{0}$ ($\mathbf{P}_i \parallel \hat{z}$) or $\left|\Psi^\mu_{\mathrm{TF}}(0)\right\rangle = \frac{1}{\sqrt{2}}\binom{1}{1}$ ($\mathbf{P}_i \parallel \hat{x}$), corresponding to two distinct experimental geometries: (1) longitudinal field (LF), with $\mathbf{P}_i \parallel \mathbf{B}$, and (2) transverse field (TF) with $\mathbf{P}_i \perp \mathbf{B}$. In general, the choice of coordinate system is arbitrary, and while $\mathbf{B}$ is conventionally along $\hat{z}$, different coordinate systems may be advantageous under certain circumstances.

The most general mixed state of a quantum system at time t is fully described by the density matrix:

$$\rho(t) = \sum_i p_i |\Psi_i(t)\rangle \langle\Psi_i(t)|, \tag{2.2}$$

where the sum goes over the complete basis set and p_i are the associated probabilities. Spin-polarized

muons are initially in a pure state (i.e. $p_1 = 1$), and the initial density matrices (i.e. at $t = 0$) are

$$\rho^{\mu}_{\mathrm{LF}}(0) = \begin{pmatrix} 1 & 0 \\ 0 & 0 \end{pmatrix}, \text{ and } \rho^{\mu}_{\mathrm{TF}}(0) = \frac{1}{2}\begin{pmatrix} 1 & 1 \\ 1 & 1 \end{pmatrix} \tag{2.3}$$

For a given Hamiltonian, the time evolution of any spin state described by ρ is determined by the time evolution operator $\mathsf{U}(\mathsf{t})$:

$$\rho(t) = \mathsf{U}(\mathsf{t})\rho(0)\mathsf{U}(\mathsf{t})^{\dagger} \text{ where } \mathsf{U}(\mathsf{t}) = \mathrm{e}^{-i\mathsf{H}t/\hbar}. \tag{2.4}$$

Knowledge of $\rho(t)$ allows the calculation of the expectation value of any spin operator O: $\langle O(t)\rangle = \mathrm{Tr}[O\rho(t)]$. In a μSR experiment, the main observable is the spin polarization *along* the initial spin direction, i.e. $P_z(t) = \langle \sigma_z(t)\rangle$ for $\mathbf{P}_i \parallel \hat{z}$ (ρ^{μ}_{LF}) and $P_x(t) = \langle \sigma_x(t)\rangle$ for $\mathbf{P}_i \parallel \hat{x}$ (ρ^{μ}_{TF}). In general, the time evolution of the spin polarization along any direction $\hat{j}$ is simply

$$P_j(t) = \left\langle \sigma_j(t)\right\rangle = \mathrm{Tr}[\sigma_j \mathsf{U}(\mathsf{t})\rho(0)\mathsf{U}(\mathsf{t})^{\dagger}] \tag{2.5}$$

Straightforward calculation shows that for $\mathbf{P}_i \parallel \hat{z}$ and $\mathbf{B} = B_z\hat{z}$, the spin is in an eigenstate and there is no time evolution: $\left\langle \sigma^{\mu}_z(t)\right\rangle = 1$. Conversely, for $\mathbf{P}_i \parallel \hat{x}$ and $\mathbf{B} = B_z\hat{z}$, we obtain $\langle \sigma^{\mu}(t)\rangle = \cos\left(\gamma_{\mu}B_x t\right)$: the expectation value precesses in the applied field.

In general, for $\mathbf{P}_i \parallel \hat{z}$ and $\mathbf{B}$ enclosing an angle θ with the $\hat{z}$ axis, the time evolution of the spin polarization along $\hat{z}$ is given by

$$P_z(t) = \langle \sigma^{\mu}(t)\rangle = \cos(\theta)^2 + \sin(\theta)^2\cos\left(\gamma_{\mu}|\mathbf{B}|t\right). \tag{2.6}$$

We can decompose the spin polarization into a time-independent LF component and an oscillatory TF component precessing at the so-called Larmor frequency

$$\omega = \gamma_{\mu}|\mathbf{B}|, \tag{2.7}$$

i.e. at a frequency directly proportional to the *magnitude* of the magnetic field. We emphasize the close correspondence between the time evolution of the expectation values of an ensemble of spin 1/2 particles and the precession of a classical magnetic moment in a magnetic field or a gyrating top. This analogy is very useful when calculating frequencies and amplitudes of signal components, and even extends to coupled spin systems in certain cases.

2.2 Concept of μSR

The purpose of this section is to introduce the concept of time-differential μSR using a continuous muon source as relevant for this thesis. It is not meant as a detailed technical introduction, for which we refer to Ref. [13], but to provide some intuitive understanding of key concepts, parameters and constraints.

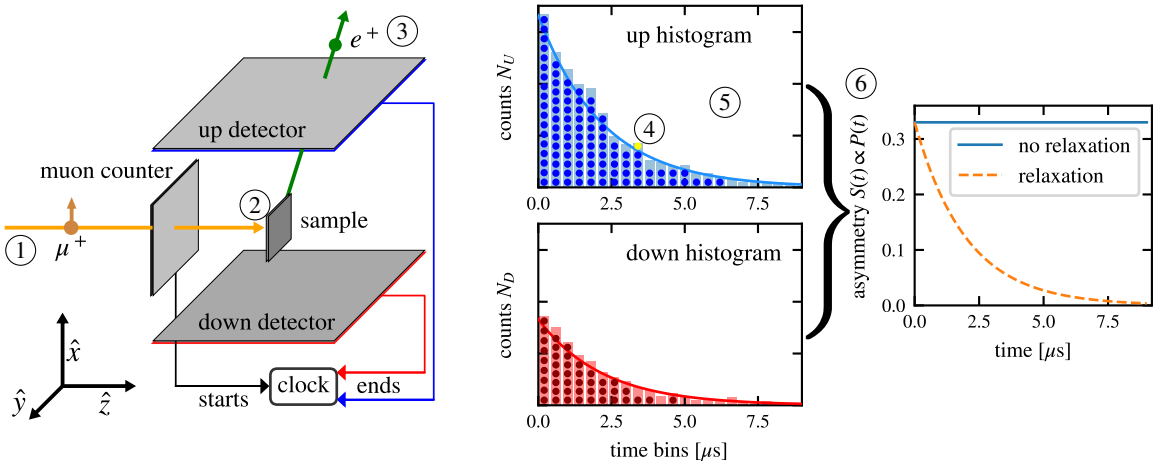

Figure 2.1: Schematic μSR setup: spin polarized muons are implanted into the sample, where they decay into two neutrinos (not detected) and a positron, which is preferentially emitted along the muon spin at the point of decay. Time-resolved observation of the positron in either of two detectors, placed along the direction of initial spin polarization, represents an event, which is recorded in the appropriate histogram. The count-rate normalized difference of a counter pair, $S(t)$, is directly proportional to the spin polarization along the detector axis. See text for details.

A schematic of a basic μSR setup is shown in Fig. 2.1. We will now go through the experimental procedure step by step, using the numbers in Fig. 2.1 as reference points. (1) Spin polarized muons are guided towards the sample in an evacuated beam pipe. In the example, the initial spin polarization $\mathbf{P}_i$ is along $\hat{x}$, rotated 90° with respect to the beam momentum $\hat{z}$; $\mathbf{P}_i$ can be selected by passing the beam through crossed magnetic and electric fields. Before reaching the sample, the muon passes through a thin plastic scintillator which triggers the start of a clock. (2) The muon is implanted into the sample and decelerates mainly via electron-hole pair and Frenkel pair (vacancy + interstitial) creation. It comes to rest much faster ($< 100\,\text{ps}$) than any timescale relevant to the experiment, and finds a stopping site which is typically close to the electrostatic minimum of the crystal lattice. The kinetic energy of "surface muons" originating from pions decaying at rest is 4.1 MeV, which requires a stopping power of about $180\,\text{mg/cm}^2$ or about $0.3-2\,\text{mm}$ of sample thickness (depending on the sample density). These sites are generally sufficiently far away from Frenkel pairs created in the muon deceleration process to consider the lattice vacancy-free; experimentally, the only observed muon-vacancy complexes originate from muon diffusion on a µs timescale [50]. In general, the muon spin interacts with its local environment; however, for this example, we chose a non-interacting sample such that the muon spin does not evolve in time: $P_x(t) = \langle \sigma_x(t) \rangle = 1$. (3) The muon decays with a mean lifetime of $\tau_\mu = 2.2\,\mu\text{s}$. The resulting decay positron is emitted preferentially along the muon spin direction [Fig. 1.1]. If it passes through either of two plastic-scintillator detectors placed along the intial spin direction, the clock is stopped, and an event is registered at the appropriate time in a histogram associated either with the 'up' or 'down'

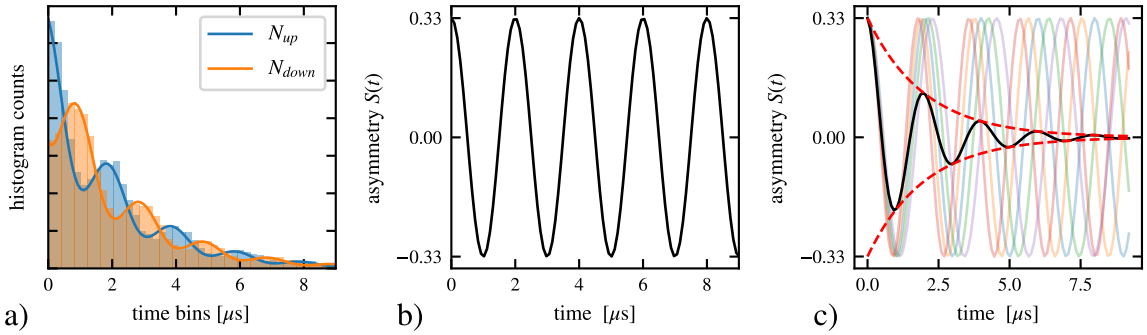

Figure 2.2: Effect of transverse fields ($\mathbf{P}_i \perp \mathbf{B}$). (a) The muon spin precession modulates the count-rate in both histograms; (b) the asymmetry signal $S(t)$ is directly proportional to the oscillatory spin expectation values along $\mathbf{P}_i$. (c) If the muons experience a distribution of magnetic fields, dephasing sets in; as a result, the overall signal is damped [black line].

detector. In the example, the 'up' detector is triggered after 3 μs, and an event is recorded accordingly (yellow sphere in the 'up' histogram ④). This process is repeated many times, until typically $N \sim 10^6$ counts / histogram are collected. Each muon is counted individually (schematically represented by the spheres in the histograms); the beam intensity is chosen such that on average, at most one muon is in the sample. If there is more than one muon in the sample at a given time, the event is discarded to avoid ambiguity. ⑤ Two aspects are of note: (1) The number of counts decreases exponentially with time; this is solely due to the nature of the muon radioactive decay. Typically, histograms are recorded up to 9-10 μs (about five muon lifetimes). (2) At *any* given time, there are (on average) twice as many counts in the 'up' histogram than in the 'down' histogram, reflecting the muon decay anisotropy [Fig. 1.1] and the fact that the spin does not evolve over time in this example. We can extract the asymmetry signal $S(t)$, the count-normalized difference of the counter pair, which is directly proportional to the spin polarization $P(t)$ along the detector axis:

$$S(t) = \frac{N_U(t) - N_D(t)}{N_U(t) + N_D(t)} = a\,P(t). \tag{2.8}$$

The right panel in Fig. 2.1 [solid blue line] shows the result for the example histogram; since the spin does not evolve with time, $S(t)$ is a straight line at an asymmetry value of $\frac{1}{3}$. Typical experimental asymmetries at $t = 0$ range between 0.2-0.3 due to a number of factors, including positron scattering, finite dimensions of positron detectors, energy dependence of the decay anisotropy and variations in the inital spin polarization. We note that Eq. (2.8) is oversimplified; in reality, uncorrelated background signals and detector efficiencies have to be considered [see Ref. [13]].

In short, μSR allows us to observe the time evolution of the spin polarization of an ensemble of initially polarized muons, providing a unique and direct window into the local magnetic and electronic environment near the stopping site of the muon. For example, if there is a source of spin-lattice relaxation such as spin fluctuations or magnon scattering, the muon spin polarization decays over time, which

is reflected in the asymmetry signal [see dashed orange line in right panel of Fig. 2.1].

Next, we consider spin precession [Eqs. (2.6) and (2.7)] in a magnetic field along $\hat{z}$, i.e. perpendicular to $\mathbf{P}_i$ (TF). As shown in Fig. 2.2 (a), the spin oscillations modulate the histogram counts, and can be extracted by constructing the asymmetry signal $S(t)$ [Eq. (2.8)]: the full signal oscillates at a frequency directly proportional to the magnitude of the magnetic field experienced by the muon [Fig. 2.2 (b)]. In Fig. 2.2 (c), we demonstrate the effect of a distribution of magnetic fields, i.e. field inhomogeneity: the muon spins precess with slightly different frequencies [faded lines], causing phase de-coherence, which leads to a damped oscillatory signal [solid black line]. The damping rate and shape of the signal envelope [dashed red line] are directly related to the field distribution; e.g. a Lorentzian field distribution of HWHM σ leads to an exponentially damped envelope envelope $\mathrm{e}^{-\lambda t}$ with damping rate $\lambda = 2\pi\sigma$.

When implanted in a crystal lattice, the muon usually stops in one or more distinct sites that minimize the overall energy. At a given temperature, several crystallographically distinct sites can be populated, each of which may cause a different time evolution of the spin polarization. For example in magnetic materials, muons may experience different internal fields at inequivalent sites, causing spin precession at different frequencies. In this case, the observed signal $S(t)$ is a sum of several components $S_i(t)$. In this thesis, oscillatory signal components are fit to

$$S_i(t) = a_i \cos(2\pi f_i t + \phi_i) \exp(-\lambda_i t), \tag{2.9}$$

where a_i, f_i, ϕ_i and λ_i are the signal amplitude, frequency, phase shift and depolarization rate, respectively. Likewise, non-oscillatory signals are parameterized by simple exponentials:

$$S_i(t) = a_i \exp(-\lambda_i t), \tag{2.10}$$

Lastly, we discuss the theoretical framework necessary to describe a charge-neutral bound state of a positive muon and an electron.

2.3 Hyperfine coupling and time evolution of a coupled spin system

The coupled spin system of muon-electron bound state is described by a combined wave function $|\Psi^{\mu e}\rangle$, since muon and electron spin interact with each other:

$$|\Psi^{\mu e}\rangle = |\psi^{\mu}\rangle \otimes |\psi^{e}\rangle\,. \tag{2.11}$$

Spin operators acting in this $2 \otimes 2 = 4$ - dimensional Hilbert space are expressed in the following basis $\left|S_z^{\mu} S_z^{e}\right\rangle$:

$$|\uparrow\uparrow\rangle = \begin{pmatrix}1\\0\\0\\0\end{pmatrix},\ |\uparrow\downarrow\rangle = \begin{pmatrix}0\\1\\0\\0\end{pmatrix},\ |\downarrow\uparrow\rangle = \begin{pmatrix}0\\0\\1\\0\end{pmatrix},\ |\downarrow\downarrow\rangle = \begin{pmatrix}0\\0\\0\\1\end{pmatrix} \tag{2.12}$$

where z designates the quantization axis, which is typically chosen either along $\mathbf{B}$ or $\mathbf{P}_i$. The operators are constructed via the tensor product in such a way that muon (electron) spin operators only act on the

muon (electron) subspace:

$$O^{\mu} = O \otimes \mathbb{1}_2, \;\; O^{e} = \mathbb{1}_2 \otimes O, \;\; \text{e.g. } \sigma_z^{\mu} = \sigma_z \otimes \mathbb{1}_2 \tag{2.13}$$

Here, the superscripts differentiating muon and electron operators implicitly indicate 4×4 matrices (rather than the 2×2 Pauli matrices in Section 2.1). An accessible introduction to tensor products can be found in Appendix A of Ref. [51].

In general, any interaction betwen the two spins can be described by a 3×3 tensor $\widetilde{\mathbf{A}}$[1], the so-called hyperfine coupling tensor:

$$\mathrm{H} = \mathbf{S}^{e} \cdot \widetilde{\mathbf{A}} \cdot \mathbf{S}^{\mu} 2\pi/\hbar = \tfrac{1}{4} h \boldsymbol{\sigma}^{e} \cdot \widetilde{\mathbf{A}} \cdot \boldsymbol{\sigma}^{\mu} = \tfrac{1}{4} h \left[A_{11} \sigma_x^{e} \sigma_x^{\mu} + A_{12} \sigma_x^{e} \sigma_y^{\mu} + \ldots + A_{33} \sigma_z^{e} \sigma_z^{\mu} \right]; \tag{2.14}$$

$\widetilde{\mathbf{A}}$ is usually expressed in units of frequency.

For muon-electron bound states formed in μSR experiments, the bound electron is initially *unpolarized*[2], i.e. $\langle \sigma_x(0) \rangle = \langle \sigma_y(0) \rangle = \langle \sigma_z(0) \rangle = 0$, corresponding to the following density matrix:

$$\rho^{e}(0) = \frac{1}{2} \begin{pmatrix} 1 & 0 \\ 0 & 1 \end{pmatrix}. \tag{2.15}$$

The density matrix for the combined muon-electron system is given by the tensor product, i.e.

$$\rho^{\mu e} = \rho^{\mu} \otimes \rho^{e}. \tag{2.16}$$

Using the muon density matrices defined in Eq. 2.3, the combined initial density matrices are simply

$$\rho_{\mathrm{LF}}^{\mu e}(0) = \rho_{\mathrm{LF}}^{\mu}(0) \otimes \rho^{e}(0) \;\; \text{and} \;\; \rho_{\mathrm{TF}}^{\mu e}(0) = \rho_{\mathrm{TF}}^{\mu}(0) \otimes \rho^{e}(0). \tag{2.17}$$

The time evolution for the combined spin system can be calculated using Eqs. (2.4) and (2.14); for example, the muon spin polarization along $\hat{z}$ is given by

$$P_z^{\mu}(t) = \left\langle \sigma_z^{\mu}(t) \right\rangle = \mathrm{Tr}[\sigma_z^{\mu} \rho_{\mathrm{LF}}^{\mu e}(t)] \tag{2.18}$$

Diagonalization of H [Eq. 2.14] yields four eigenenvalues. In general, i.e. for a arbitrary hyperfine tensor, the time evolution of the spin expectation values contains a non-oscillatory component and up to six oscillatory components at different frequencies ν corresponding to all possible transitions between

[1]Note that neither $\widetilde{\mathbf{A}}$ nor H contain any information on the spin states themselves, but only describe how spins *interact* once a spin state ρ has been specified. $\widetilde{\mathbf{A}}$ is not a spin operator (and notably a 3×3 matrix acting on the spin 3-*vectors*), but determines the weight of all possible spin operator combinations, see Eq. 2.14. Once a basis set is chosen, the spin operators (and H) can be expressed in 4×4 matrices (or 2×2 for single spin 1/2 in Section 2.1).

[2]There are exceptions: for example, in high magnetic fields at low temperatures, the ratio of electron Zeeman splitting and thermal energy can be sufficiently large to allow for a finite electron spin polarization, see e.g. Ref. [52]

the four energy levels $h\nu_{ij} = E_i - E_j$:

$$P_z^{\mu}(t) = \left\langle \sigma_z^{\mu}(t) \right\rangle = a_0 + \sum_{\substack{i=1 \\ i<j}}^{4} \sum_{j=1}^{4} a_{ij} \cos(2\pi\nu_{ij} + \phi_{ij}) \tag{2.19}$$

A (very lengthy) general expression for all amplitudes a, frequencies ν and phases ϕ for an arbitrary 4×4 Hamiltonian can be obtained and is very useful to understand and visualize the relative strengths of various signal contributions[3].

In this thesis, we discuss different forms of $\widetilde{\mathbf{A}}$, i.e. variations of muon-electron spin couplings, and discuss implications and applications arising from the formation of charge-neutral centers for the μSR technique. We begin with *isotropic* muonium, a hydrogen-like muon-electron bound state.

[3]This general expression can be calculated by transforming the density matrix into the diagonal system $\rho^D = T\rho T^{\dagger}$, where T has the eigenvectors as column vectors. Then, the unitary time evolution operator is simply

$$\mathsf{U}(\mathsf{t}) = \mathrm{e}^{-i\mathsf{H}t/\hbar} = \exp\left[-i \begin{pmatrix} E_1 & & \\ & \ddots & \\ & & E_4 \end{pmatrix} t/\hbar\right] = \begin{pmatrix} \mathrm{e}^{-iE_1 t/\hbar} & & \\ & \ddots & \\ & & \mathrm{e}^{-iE_4 t/\hbar} \end{pmatrix}, \tag{2.20}$$

which can be used to calculate $\rho^D(t)$. Transforming back into the lab coordinate frame and using e.g. Eq. 2.18 yields a lengthy general expression of terms proportional to $\mathrm{e}^{-i(E_i - E_j)t/\hbar}$, which can be collected and sorted in the form of Eqn. 2.19. The expressions are too long to use by hand and are therefore coded up in python.

Chapter 3

Isotropic muonium in a silica aerogel

3.1 Introduction

Muonium (Mu $= [\mu^+ e^-]$) may be considered the simplest atom in nature since both its constituents are structureless fundamental particles. As such, measurable properties of Mu, including its hyperfine interval [53, 54] and Lamb shift [55], provide stringent tests to predictions from quantum electrodynamics [56–59]. In addition, Mu may be used to create a beam of low energy muons by ionization of Mu in vacuum via two photon absorption [60, 61] and subsequent acceleration of the resulting μ^+. Such a beam has many applications covering a broad spectrum of experiments from fundamental physics (including the search for the muon electric dipole moment [62, 63] and next-generation muon g-2 measurements [62, 64]) to condensed matter physics, where spin-polarized μ^+ are used as a sensitive local probe for magnetism and superconductivity [13], and low-energy muons enable the investigation of thin films and heterostructures [65, 66]. However, in order to make such applications viable, intense slow muon beams are required, which motivates the search for an efficient source for Mu in vacuum.

Several approaches are being explored, including the emission of Mu from a hot (2300 K) tungsten foil placed in a muon beam [67, 68] and current efforts to extend this method to *n*-type silicon at low (100 K) temperatures [69]. The most encouraging results are obtained in silica (SiO_2) powders and aerogels. A large fraction of positive muons implanted into silica powders form Mu, and escape into the intergranular spaces with high likelihood [70]. If the powder grains are sufficiently small, this vacuum emission happens even at low temperatures, indicating that the escape occurs before the Mu is thermalized [71, 72]. Very similar behavior was found for mesoporous silica samples [73–76]. In recent years, amorphous silica aerogels with high porosity and ultra-low density [77, 78] have emerged as a promising candidate for producing Mu in vacuum at room temperature since they are self-supporting and can be drilled with micron sized holes, which improve the yield of Mu in vacuum [64, 79, 80]. However, there is little information about the temperature dependence of Mu production in aerogels and the role of surface interactions, which control Mu diffusion in the intergranular space and, in conjunction with sample morphology and geometry, the production rate of Mu in vacuum.

This chapter presents a muon spin rotation (μSR) study investigating the diffusive behavior of Mu in the voids of a silica aerogel. Using a fast-timing spectrometer capable of resolving high-frequency Mu precession signals in a 1.14 T magnetic field, the temperature dependence of the Mu hyperfine coupling is precisely measured. The observed signals are a sensitive monitor of the dynamics associated with the binding and unbinding of Mu from the silica surface, and are interpreted using a simple statistical mechanics model. This research was published in Ref. [81] as part of a comparative study between mesoporous silica (SBA-15) and a silica aerogel. For the sake of simplicity and brevity, only the aerogel results are presented here.

The chapter proceeds as follows. First, in Sec. 3.2, the theory of Mu in vacuum is discussed. Mu in vacuum is the simplest example of a charge-neutral muon state, since the electron is isotropically distributed around the muon. Therefore, it provides a good basis for the discussion of more complicated charge-neutral states *inside* materials (subsequent chapters), where the interaction between the muon and electron spins is often *anisotropic* and greatly reduced compared to Mu in vacuum. In Sec. 3.3, details on the aerogel sample and experimental conditions are given. Then, in Sec. 3.4, the results are presented and discussed.

3.2 Theory - Isotropic muonium

Both constituents of Mu, the positive muon μ^+ and the electron e^-, carry magnetic moments that interact with each other via the so-called hyperfine interaction. In general, this interaction has a dipolar and Fermi-contact contribution [82]. However, for *isotropic* muonium, where the bound electron occupies a spherically symmetric $1s$ atomic orbital, the dipolar contribution is averaged out, leaving only the rotationally invariant Fermi-contact term, which is directly proportional to the unpaired electron density at the muon position $|\psi^e(0)|^2$ [82–84]:

$$\mathrm{H} = \frac{2\mu_0}{3}\gamma_e\gamma_\mu \mathbf{S}^e\cdot\mathbf{S}^\mu|\psi^e(0)|^2 = \frac{1}{4}hA_{iso}\boldsymbol{\sigma}^e\cdot\boldsymbol{\sigma}^\mu = \tfrac{1}{4}h\boldsymbol{\sigma}^e\cdot\widetilde{\mathbf{A}}_{iso}\cdot\boldsymbol{\sigma}^\mu, \tag{3.1}$$

where the isotropic hyperfine tensor is proportional to the identity matrix, i.e $\widetilde{\mathbf{A}}_{iso} = A_{iso}\mathbb{1}_3$. The *strength* of the interaction is given by the isotropic hyperfine parameter A_{iso}, which is $A_{iso}^{vac} = 4\,463\,302\,765(53)$ Hz for Mu in vacuum in its ground state [53]. Expressing the spin operators in the basis defined in Eqn. (2.12), we obtain

$$\mathrm{H} = \tfrac{1}{4}hA_{iso}\boldsymbol{\sigma}^e\cdot\boldsymbol{\sigma}^\mu = \hbar\omega_{iso}\frac{1}{4}(\sigma_x^\mu\sigma_x^e + \sigma_y^\mu\sigma_y^e + \sigma_z^\mu\sigma_z^e) = \frac{\hbar\omega_{iso}}{4}\begin{pmatrix}1&0&0&0\\0&-1&2&0\\0&2&-1&0\\0&0&0&1\end{pmatrix}. \tag{3.2}$$

$|\uparrow\uparrow\rangle$ and $|\downarrow\downarrow\rangle$ are clearly eigenstates, whereas $|\uparrow\downarrow\rangle$ and $|\downarrow\uparrow\rangle$ are coupled by the off-diagonal elements originating from the $\sigma_x^\mu\sigma_x^e + \sigma_y^\mu\sigma_y^e$ terms. S_z^e and S_z^μ individually do not commute with H, however the total $S_z^{\mathrm{tot}} = S_z^e + S_z^\mu$ as well as $(S^{\mathrm{tot}})^2$ do, and are therefore conserved quantities. The eigenvalues of

this Hamiltonian (in units of $\frac{\hbar\omega_{iso}}{4}$) are $1,1,1,-3$, with corresponding eigenvectors $|1\rangle = |\uparrow\uparrow\rangle$, $|2\rangle = (|\uparrow\downarrow\rangle + |\downarrow\uparrow\rangle)/\sqrt{2}$, $|3\rangle = |\downarrow\downarrow\rangle$, $|4\rangle = (|\uparrow\downarrow\rangle - |\downarrow\uparrow\rangle)/\sqrt{2}$ [see Fig. 3.1 (a) at 0 T].

Specifying the initial spin state as $\rho_{\mathrm{LF}}^{\mathrm{Mu}}$ [Eq. (2.17)], i.e. with the initial muon spin polarization along $\hat{z}$ and the electron spin unpolarized, and using the time evolution operator [Eqn. (2.4)], $\rho^{\mathrm{Mu}}(t)$ and subsequently the time evolution of the muon spin expectation value along $\hat{z}$ can be calculated:

$$\left\langle \sigma_z^{\mu}(t) \right\rangle = \tfrac{1}{2}[1+\cos(\omega_{iso}t)], \tag{3.3}$$

Half of the muon spin polarization is time independent, and half oscillates at $\omega_{iso} = 2\pi A_{iso}$, the so-called "heartbeat" oscillation, due to the interaction with the electron spin[1]. We can also calculate the time evolution of the *electron* spin along $\hat{z}$:

$$\left\langle \sigma_z^{e}(t) \right\rangle = \tfrac{1}{2}[1-\cos(\omega_{iso}t)], \tag{3.4}$$

demonstrating that spin polarization is coherently transferred back and forth between the muon and the initially unpolarized electron such that S_z^{tot} is conserved, i.e. $\left\langle \sigma_z^{e}(t) \right\rangle + \left\langle \sigma_z^{\mu}(t) \right\rangle = 1$.

In the presence of magnetic fields, there are two additional terms in the Hamiltonian, accounting for the muon and electron Zeeman interaction:

$$\mathrm{H}/\hbar = \tfrac{\omega_{iso}}{4}\boldsymbol{\sigma}^{\mu}\cdot\boldsymbol{\sigma}^{e} + \tfrac{1}{2}\gamma_e\mathbf{B}\cdot\boldsymbol{\sigma}^{e} - \tfrac{1}{2}\gamma_{\mu}\mathbf{B}\cdot\boldsymbol{\sigma}^{\mu} = \begin{pmatrix} \gamma_- B + \frac{\omega_{iso}}{4} & 0 & 0 & 0 \\ 0 & -\gamma_+ B - \frac{\omega_{iso}}{4} & \frac{\omega_{iso}}{2} & 0 \\ 0 & \frac{\omega_{iso}}{2} & \gamma_+ B - \frac{\omega_{iso}}{4} & 0 \\ 0 & 0 & 0 & -\gamma_- B + \frac{\omega_{iso}}{4} \end{pmatrix}, \tag{3.5}$$

where $\gamma_{\pm} = \frac{|\gamma_e| \pm \gamma_{\mu}}{2}$ and $\mathbf{B} = B_z$ (without loss of generality) is used for the matrix expression. We emphasize that the hyperfine coupling itself (i.e. the muon - electron interaction described by $\widetilde{\mathbf{A}}$) is *not* modified by the magnetic field. However, the additional terms in the Hamiltonian compete with the off-diagonal terms that couple the muon and electron spins; how H acts on a given spin state depends on the relative strength of the electron Zeeman term and the hyperfine interaction. In this context, it is useful to introduce B_0, the effective hyperfine field of the muon acting on the electron, as well as x, the ratio of the applied and hyperfine field:

$$B_0 = \frac{\omega_{iso}}{2\gamma_+}, \qquad x = \frac{B}{B_0} = \frac{2\gamma_+ B}{\omega_{iso}}. \tag{3.6}$$

The eigenstates and eigenenergies, as well as the field-dependent prefactors of the eigenstates, $a(B)$ and $b(B)$, are given in Table 3.1. The applied field splits the eigenenergies into four non-degenerate levels, each with a distinct field dependence [Fig. 3.1 (a)].

[1] This can be understood intuitively as follows. The unpolarized electron ($\rho^e(0) = \frac{1}{2}\left(\begin{smallmatrix} 1 & 0 \\ 0 & 1 \end{smallmatrix}\right)$) is a classical mixture of $|\uparrow\rangle$ and $|\downarrow\rangle$ with equal probability for *any* chosen direction. Choosing the quantization axis along the initial muon polarization, the initial combined spin state is either $|\uparrow\uparrow\rangle$ or $|\uparrow\downarrow\rangle$. The former is an eigenstate, and there is no time evolution. The latter is a superposition of states $|2\rangle$ and $|4\rangle$ with energy difference $\hbar\omega_{iso}$, causing oscillation at ω_{iso}.

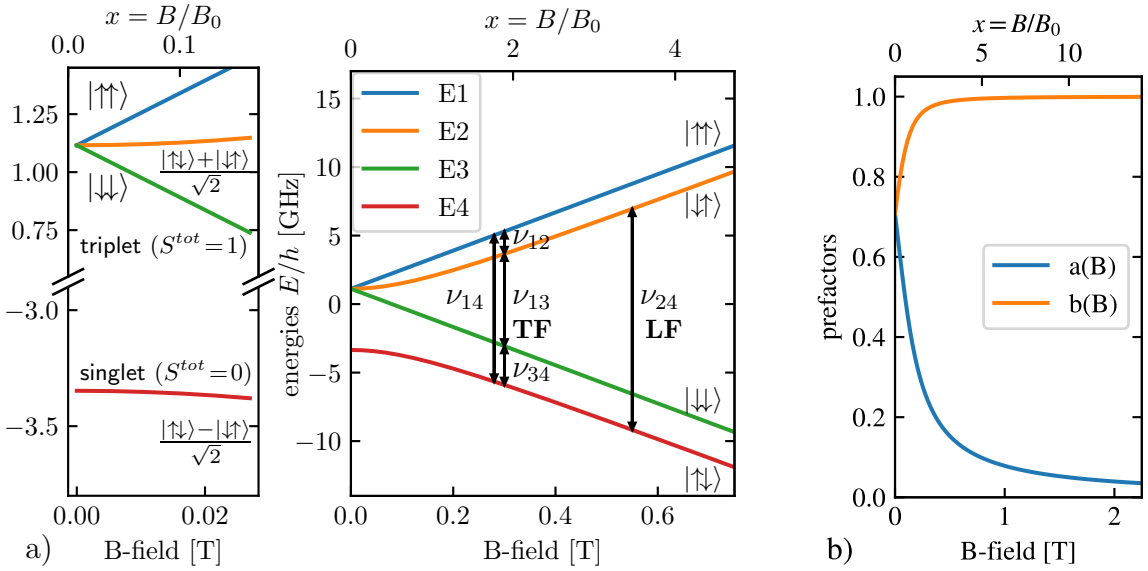

Figure 3.1: (a) Eigenenergies for isotropic Mu as a function of magnetic field. Arrows indicate allowed transitions $\nu_i = \omega_i/\pi$ in the transverse field (TF) and longitudinal field (LF) configuration. (b) Field dependence of the prefactors of eigenstates $|2\rangle$ and $|4\rangle$. For $x \gg 1$, the muon and electron spin decouple, and $b(B)$ approaches unity as S_z^e and S_z^μ become good quantum numbers.

$$
\begin{array}{r|l|l}
|1\rangle = |\uparrow\uparrow\rangle & E_1/\hbar = \gamma_- B + \frac{\omega_{iso}}{4} & \\
|2\rangle = a(B)\,|\uparrow\downarrow\rangle + b(B)\,|\downarrow\uparrow\rangle & E_2/\hbar = -\frac{\omega_{iso}}{4} + \sqrt{\gamma_+^2 B^2 + \frac{\omega_{iso}^2}{4}} & a(B) = \frac{1}{\sqrt{2}}\sqrt{1 - \frac{x}{\sqrt{1+x^2}}} \\
|3\rangle = |\downarrow\downarrow\rangle & E_3/\hbar = -\gamma_- B + \frac{\omega_{iso}}{4} & \\
|4\rangle = b(B)\,|\uparrow\downarrow\rangle - a(B)\,|\downarrow\uparrow\rangle & E_4/\hbar = -\frac{\omega_{iso}}{4} - \sqrt{\gamma_+^2 B^2 + \frac{\omega_{iso}^2}{4}} & b(B) = \frac{1}{\sqrt{2}}\sqrt{1 + \frac{x}{\sqrt{1+x^2}}}
\end{array}
$$

Table 3.1: Eigenstates and eigenenergies for isotropic Mu in a magnetic field of magnitude B. $a(B)$ and $b(B)$ are field-dependent prefactors of eigenstates $|2\rangle$ and $|4\rangle$. See e.g. Ref. [13] for a more detailed derivation.

For small applied fields ($x \ll 1$), the hyperfine interaction dominates, the eigenstates $|2\rangle$ and $|4\rangle$ remain superpositions ($a(B) \approx b(B) \approx \frac{1}{\sqrt{2}}$, see Fig. 3.1 (b)), and muon and electron spins are entangled.

Conversely, for large applied fields ($x \gg 1$), $a(B) \to 0$ and $b(B) \to 1$, the off-diagonal elements in Eq. (3.5) are small compared to the diagonal Zeeman terms, and muon and electron spins decouple. In this context, decoupling refers only to the spin states: S_z^e and S_z^μ rather than S_z^{tot} are now conserved quantities, and $|\uparrow\downarrow\rangle$ and $|\downarrow\uparrow\rangle$ eigenstates; the energy levels, however, are still affected by (mainly the diagonal contributions of) the hyperfine coupling. An intuitive interpretation of the Mu density matrix $\rho^{\mu e}(t)$ [Eq. (2.16)] in this limit is that the electron spin projects either along or opposite the applied field direction, while the muon spin evolves in the *combined* applied and hyperfine field.

The time evolution of the muon spin depends on its initial spin state with respect to the applied field.

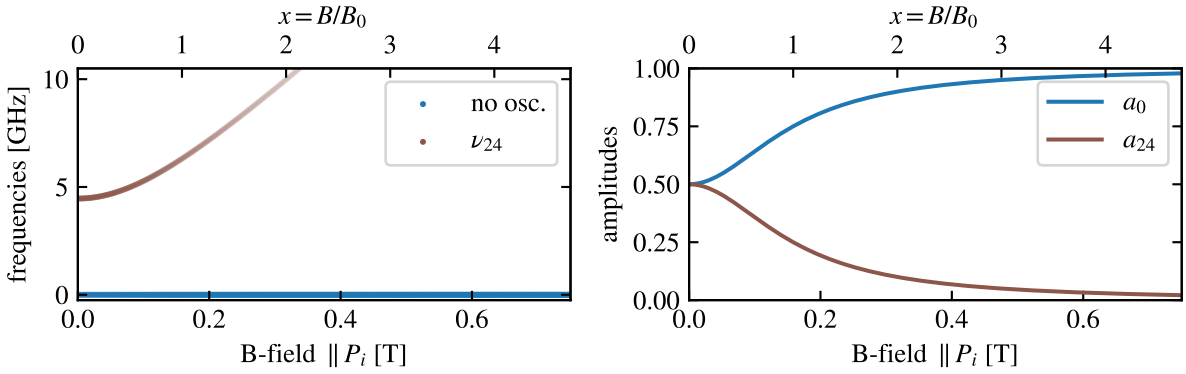

Figure 3.2: (a) Oscillation frequency $\nu_{24} = \omega_{24}/2\pi$ and (b) amplitudes for the oscillatory component (a_{24}) and non-oscillatory component (a_0) for isotropic Mu as a function of magnetic field along the initial muon polarization (i.e. longitudinal field geometry).

For the initial spin polarization $\mathbf{P}_i$ *along* the applied field (i.e. $\rho_{\mathrm{LF}}^{\mathrm{Mu}}(0)$), here $\mathbf{B} = B_z$, the time evolution of the muon spin polarization along $\hat{z}$ for isotropic Mu is [using Eqs. (3.5) and (2.4)]

$$\left\langle \sigma_z^{\mu}(t) \right\rangle = \tfrac{1}{2}\left[1 + \frac{x^2}{x^2+1} + \frac{\cos(\omega_{24} t)}{x^2+1}\right], \quad \text{with} \quad \omega_{24} = (E_2 - E_4)/\hbar = \sqrt{4(\gamma_+ B)^2 + \omega_{iso}^2} \tag{3.7}$$

There is a time-independent and an oscillating component, with the frequency and amplitudes shown in Fig. 3.2. For $x \to 0$, the zero field result [Eq. 3.3] is obtained. With increasing x, the back-and-forth transfer of spin polarization between muon and electron is suppressed as the two spins decouple and S_z^{tot} no longer is a good quantum number. The oscillating component decreases in amplitude until the ω_{24} transition is fully suppressed and the muon spin polarization is completely time independent.

In contrast, if $\mathbf{P}_i$ is perpendicular to the applied field ($\mathbf{P}_i^{\mu}(0) \parallel \hat{x} \perp \mathbf{B}$), $\rho_{\mathrm{TF}}^{\mathrm{Mu}}$ [Eq. (2.17)] is applicable and up to four distinct frequencies can be observed:

$$\left\langle \sigma_x^{\mu}(t) \right\rangle = \tfrac{1}{4}\left[\left(1 + \tfrac{x}{\sqrt{x^2+1}}\right)\left(\cos(\omega_{12} t) + \cos(\omega_{34} t)\right) + \left(1 - \tfrac{x}{\sqrt{x^2+1}}\right)\left(\cos(\omega_{23} t) + \cos(\omega_{14} t)\right)\right], \tag{3.8}$$

with frequencies given by $\omega_{ij} = (E_i - E_j)/\hbar$, see Table 3.1:

$$\begin{aligned}
\omega_{12} &= \gamma_- B + \tfrac{\omega_{iso}}{2} - \sqrt{\gamma_+^2 B^2 + \tfrac{\omega_{iso}^2}{4}} \\
\omega_{14} &= \gamma_- B + \tfrac{\omega_{iso}}{2} + \sqrt{\gamma_+^2 B^2 + \tfrac{\omega_{iso}^2}{4}} \\
\omega_{23} &= \gamma_- B - \tfrac{\omega_{iso}}{2} + \sqrt{\gamma_+^2 B^2 + \tfrac{\omega_{iso}^2}{4}} \\
\omega_{34} &= -\gamma_- B + \tfrac{\omega_{iso}}{2} + \sqrt{\gamma_+^2 B^2 + \tfrac{\omega_{iso}^2}{4}}
\end{aligned} \tag{3.9}$$

For small applied fields ($x \ll 1$), all four frequencies contribute [Fig. 3.3 (a)]. Since none of the experiments presented in this thesis are carried out for $x \ll 1$, a detailed discussion of this regime is out

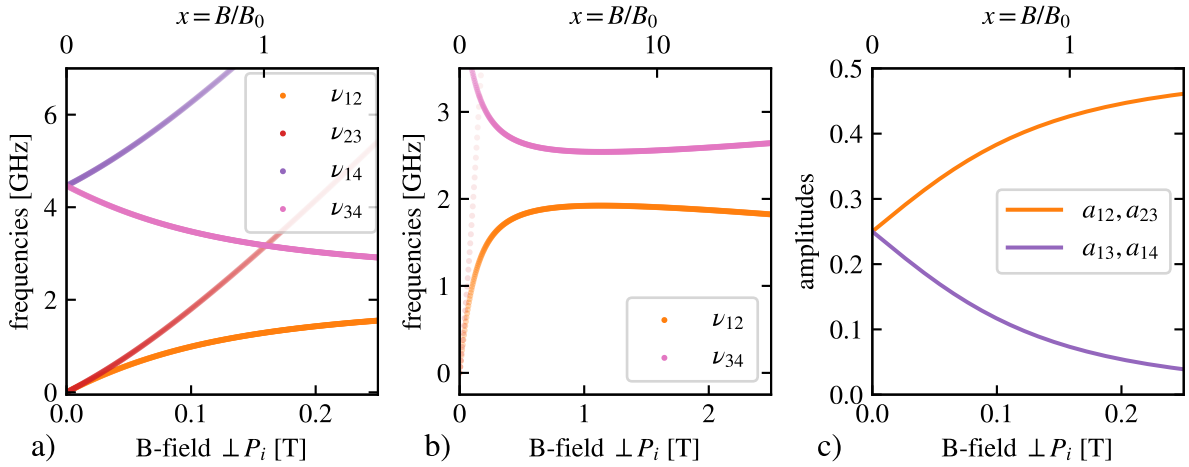

Figure 3.3: (a) and (b) Oscillation frequencies and (c) amplitudes for isotropic Mu as a function of magnetic field perpendicular to the initial muon polarization (i.e. transverse field geometry).

of scope, and we refer to Refs. [13, 32].

For $x \gg 1$, the muon and electron spins decouple and the signal is dominated by only two frequencies ω_{12} and ω_{34} [Fig. 3.3 (b)], corresponding to the muon precession frequencies in the *combined* applied and hyperfine field, with the electron spin projected either along or opposite to the applied field direction. Importantly, the relation [85]

$$\omega_{12} + \omega_{34} = \omega_{iso} \tag{3.10}$$

holds for all fields, and observation of ω_{12} and ω_{34} allows the accurate spectroscopic determination of the isotropic hyperfine coupling constant A_{iso}. This forms the basis of the experiment described on the following pages.

3.3 Experimental details

The aerogel sample was synthesized following Ref. [77] and had a density of $\sim 180\,\mathrm{mg/cm^3}$ and a specific surface area of $896\,\mathrm{m^2/g}$ as measured by the The Brunauer-Emmett-Teller method [86]. Prior to the experiment the sample was heated for $\sim 48\,\mathrm{h}$ at $\sim 150\,^\circ\mathrm{C}$ in a vacuum better than $10^{-3}\,\mathrm{mbar}$ to remove residual moisture from the surfaces. The sample was mounted in a Ti cell in a cold finger cryostat, and briefly exposed ($< 15\,\mathrm{min}$) to ambient conditions between bake-out and mounting. The μSR measurements were carried out at the Paul-Scherrer-Institute (Villigen, Switzerland) using the fast-timing high-field spectrometer HAL-9500, which is capable of resolving high-frequency ($> 1\,\mathrm{GHz}$) Mu signals. Spin polarized muons were implanted into the sample with the initial spin polarization $\mathbf{P}_i$ perpendicular to the external field $\mathbf{B}$ (transverse field geometry).

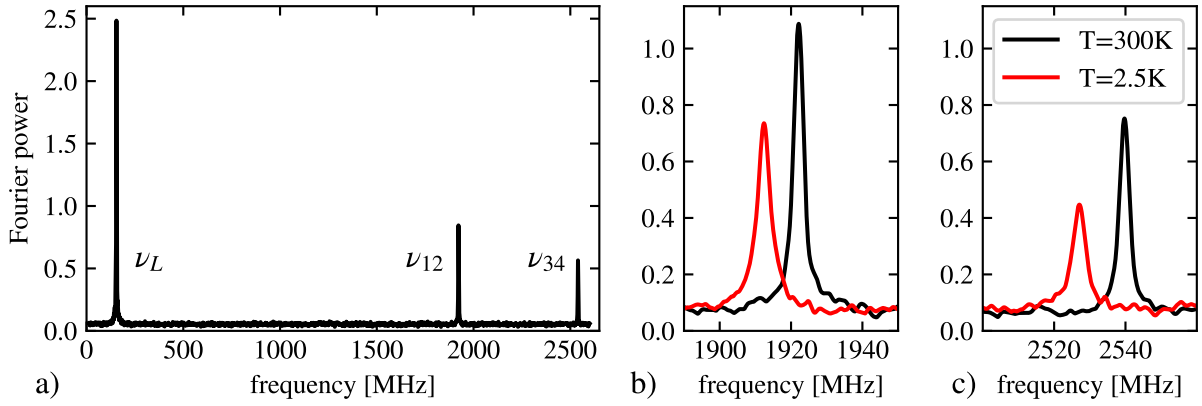

Figure 3.4: (a) Fourier transform of the precession signals in aerogel near 300 K. The two higher frequencies (ν_{12} and ν_{34}) originate from Mu. The difference in amplitudes is due to the finite time resolution of the detector system. (b) and (c) show expanded regions of the frequency spectrum in the vicinity of ν_{12} and ν_{34}, which originate from the electron hyperfine interaction either adding to or subtracting from the applied field. Adapted from Ref. [81].

3.4 Results and discussion

An example frequency spectrum in 1.14 T ($= 7.2 B_0$) at 300 K is shown in Fig. 3.4 (a). Both Mu frequencies ν_{12} and ν_{34} are well resolved; considering both the finite time resolution of the detector system (80 ps) and muons stopping in the sample cell, more than 60 % of the muons implanted into the aerogel form Mu, consistent with similar aerogel samples [80]. The frequency labeled ν_L is attributed to muons that do not form Mu and therefore precess at the Larmor frequency of the applied field. The data is consistent with previous studies in porous or powdered silica compounds, which reported that Mu is rapidly ejected into and diffuses through the pores and voids inside the material, only weakly interacting with the silica via surface interactions [70–76, 87]. Sharp narrow lines are evident at 300 K [Figs. 3.4 (b) and (c), black trace]. As the temperature is lowered, the Mu lines broaden and shift to lower frequencies by up to $\sim$12 MHz at 2 K [red trace]. All spectra were fit in the time domain to a sum of three exponentially damped cosines [Eq. (2.9)] using the analysis program musrfit [88–91]. Using Eq. (3.10), $A_{iso}(T)$ is determined [Fig. 3.5 (a)].

The temperature dependence observed in the aerogel allows for a simple interpretation [85]. Below 10 K, the Mu is weakly bound to the silica surfaces, which perturbs the spherical symmetry of the Mu $1s$ orbital such that anisotropic atomic orbitals such as $2p$ (which do not have any spin density for $\mathbf{r} = 0$, i.e. no contact term) are neccessary to describe the electron wavefunction, reducing the isotropic part of the hyperfine interaction. With increasing temperature, the Mu desorbs and undergoes cycling on and off the surface, leading to a weighted time-average of isotropic hyperfine parameters on (A_s) and off (A_f) the surface. At 300 K, the measured hyperfine interaction approaches a constant value A_f which is slightly below that of Mu in vacuum. This negative shift is attributed to Mu colliding freely with the

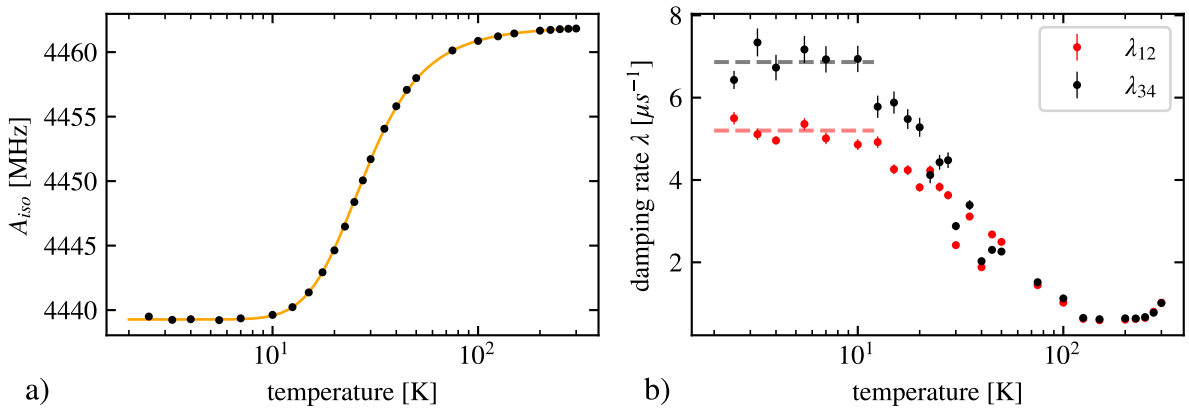

Figure 3.5: (a) Isotropic hyperfine coupling as a function of temperature for aerogel. Orange curve is a fit to the 2-state model [Eq. (3.12)] (b) Damping rates λ_{12} and λ_{34} versus temperature. At low temperatures, λ_{34} is larger than λ_{12} by a factor of 1.32 (dashed lines), indicating that a distribution of isotropic hyperfine parameters is the dominant source of broadening. Adapted from Ref. [81]. CC BY 4.0

silica surfaces, which perturbs the electronic wave function of Mu during the collision [92, 93].

The solid curve in Fig. 3.5 (a) is a fit to a statistical mechanics model for Mu confined to a box of volume V with surface area A, S_0 binding sites per unit area, and a total of $N_s = S_0 A$ surfaces states, each with a binding energy E_B [85, 94]. The single particle partition function for such a system is

$$Z = N_s \exp(E_B/k_B T) + V(mk_B T/2\pi\hbar^2)^{3/2}, \tag{3.11}$$

where the first term accounts for the surface bound states and the second for unbound states of Mu with mass m moving freely. At high enough temperatures where the system cycles fast through all microstates we expect to observe a mean hyperfine frequency [85]:

$$\begin{aligned} A_{iso}(T) &= [A_s N_s \exp(E_B/k_B T) + A_f V(mk_B T/2\pi\hbar^2)^{3/2}]/Z \\ &= [1-\alpha(T)]A_f + \alpha(T)A_s, \end{aligned} \tag{3.12}$$

where $\alpha(T) = 1/[1+\zeta T^{3/2}\exp(-E_B/k_B T)]$ is the probability that the Mu atom is on the surface and $\zeta = V(mk_B/2\pi\hbar^2)^{3/2}/AS_0$ is a constant depending on fundamental constants and material properties. This simple model agrees well with the aerogel data [Fig. 3.5 (a)], yielding fit parameters $A_f = 4461.99(1)$ MHz, $A_s = 4439.27(7)$ MHz , $E_B/k_B = 42(2)$ K and $\zeta = 0.030(1)\,\mathrm{K}^{-3/2}$; we note that the magnitude of E_B indicates a weak Van der Waals interaction with the surface rather than chemisorption.

The damping rates λ are shown in Fig. 3.5 (b). λ_{34} is significantly larger than λ_{12} at low temperatures. Differentiating ν_{12} and ν_{34} [Eq. (3.9)] with respect to A_{iso} shows that ν_{34} is more sensitive to small variations in A_{iso}, leading to a predictable ratio $\lambda_{34}/\lambda_{12}$ if the line broadening is due to a distribution of

isotropic hyperfine parameters A_s on the silica surface:[2]

$$\lambda_{34}/\lambda_{12} = [B/B_0 + 1]/[B/B_0 - 1] = 1.32, \tag{3.14}$$

In Fig. 3.5 (b), the dashed lines are plotted at this ratio, and show good agreement with the data, strongly indicating that a spread in A_{iso}, or more accurately A_s, is indeed the main source of broadening in this temperature regime. Parametrizing this spread in A_s with a Lorentzian of half width δA_s, we estimate 2.0(3) MHz [3]. In addition, anisotropic contributions to the electron wave function introduced by the surface interactions can, in general, influence both magnitude and distribution of the measured frequencies, and are expected to play a role here as well. However, since hyperfine anisotropy affects both frequencies equally (i.e. $\lambda_{34}/\lambda_{12} = 1$) and was furthermore found to play only a minor role in mesoporous silica [75, 81], it is very likely not the dominant source of line broadening, and not further discussed here.

The temperature dependence of the damping rates in Fig. 3.5 (b) further support the conclusions drawn from the simple statistical mechanics model described above, although there are indications that the real situation is more complex. The decrease in line width with increasing temperature is consistent with Mu cycling on and off the surfaces, sampling an increasing number of values from the A_s distribution, which leads to motional narrowing. However, compared to a simple box model, a slower approach to complete motional narrowing is expected for amorphous aerogel, i.e. highly porous media with multiple length scales, where a distribution of poorly connected boxes with varying dimensions may be a better description. For complete motional narrowing, Mu must rapidly average over all states in *all* the boxes, requiring higher cycle rates and thus higher temperatures, which leads to a more gradual approach to the motionally narrowed limit. Furthermore, we note that with increasing temperatures, the ratio $\lambda_{34}/\lambda_{12}$ decreases towards unity, indicating that once Mu becomes mobile, other mechanisms which affect both frequencies equally (e.g. spin exchange or chemical reaction with dangling bonds on the silica surface [95]) contribute to the observed line broadening.

3.5 Conclusion

In summary, we made precise measurements of the temperature dependence of the Mu hyperfine interaction in a silica aerogel. A simple statistical mechanics model was used to describe $A_{iso}(T)$ and estimate the binding energy of Mu to the silica surface. Above 30 K, Mu spends more time off than on the surface, and is mostly off the surface above 100 K, indicating the possibility to produce thermal Mu in vacuum far below room temperature. This is consistent with results by Antogini *et al.*, who reported

[2] Here, B_0 [Eq. (3.14)] is defined in terms of A_s. First, ν_{12} and ν_{34} [Eq. (3.9)] are expanded such that

$$\nu_j = A_{iso}/2 \mp \gamma_\mu B/(2\pi) \mp A_{iso}^2 2\pi/(8\gamma_+ B), \tag{3.13}$$

with the upper (lower) sign for $j = 12$ (34). Differentiation yields $\frac{\partial \nu_j}{\partial A_{iso}} = \frac{1}{2} \mp \frac{B_0}{B}$, which is proportional to the linewidth λ_j

[3] Expansion of Eq. (3.13) around a mean hyperfine frequency $\overline{A}_s$ yields an expression linear in A_s: $\nu_j(A_s)|_{A_{iso}=\overline{A}_s} \approx A_s(1 \mp B_0/B)/2 + \overline{A}_s/(4B/B_0) \mp \gamma_\mu B/(2\pi)$, allowing for an estimate of the damping rates for a given distribution of A_s: $\lambda_j = \pi(1 \mp B_0/B)\delta A_s$.

Mu emission from mesoporous silica thin films at 100 K, however using low-energy rather than surface muons [57]. In order to increase the Mu vacuum yield using readily available surface muons, structured silica compounds appear promising; for example, increased Mu emission rates were reported for aerogel with laser-drilled channels spaced $\sim 10^2$ μm apart [64, 80]. Even higher yields may be possible given recent advances in 3D printing of mesoporous silica [96] and silica aerogels [97, 98], which enable the fabrication of complex objects with μm precision, and thus silica structures with tightly packed ordered channels optimized for Mu emission.

The high-transverse-field technique used in this experiment is well suited to characterize the surface interactions and dynamics of Mu in highly porous materials, and thus may provide a way to test diffusion models for hierarchical and fractal materials where conventional theories for diffusion in homogeneous materials do not apply [99–101].

In the next chapter, we discuss charge-neutral muon-electron bound states *inside* materials, where the unpaired electron often has a more complex, anisotropic distribution and may not even be centered on the muon. Nonetheless, many aspects of isotropic Mu that were discussed in this chapter translate to such Mu defect centers in semiconductors and insulators.

Chapter 4

Anisotropic (polaronic) muonium in TiO_2

4.1 Introduction

When positively charged muons are implanted into semiconductors and insulators, they often bind an electron to form muonium defect centers. These are conventionally referred to as *paramagnetic* centers since the bound electron is unpaired and its spin is only weakly coupled to the lattice. Importantly, the aforementioned correspondence between hydrogen and Mu holds to good approximation for charge-neutral muon centers formed *within* semiconductors and insulators. This justifies the use of muonium as a probe for the behavior of isolated interstitial hydrogen, which is one of the most common and important impurities in semiconductors [36–38]. Unintentionally incorporated during growth and post-processing, hydrogen is very hard to control and detect, but can have a significant impact on the electronic properties. Understanding the dopant characteristics of such defects is critical for a precise control of charge carriers, upon which much of modern electronic technology is based. However, since isolated hydrogen defect centers in semiconductors are extremely hard to study directly, most experimental information about its dopant characteristics comes from the study of Mu, serving as a light hydrogen analog.

Following pioneering experiments on Mu in semiconductors by Gurevich *et al.* [102, 103], Brewer *et al.* investigated silicon, and observed aside from "normal" (isotropic) Mu an additional so-called "anomalous" signal that indicated the existence of an anisotropic Mu center with much lower hyperfine coupling [104]. Analogous signals were subsequently observed in a range of materials including isostructural germanium [105] and diamond [106], as well as GaAs and GaP [107]. It quickly became clear that inside a material, the bound electron is not well described by an isotropic 1s hydrogen-like orbital centered on the interstitial muon[1], but can have a more complicated distribution, which affects the muon-electron hyperfine interaction $\widetilde{\mathbf{A}}$ and consequently the observed spectra. The anomalous Mu center was determined to have a rotationally symmetric electron distribution with respect to the muon, however even more complicated, fully anisotropic Mu centers were reported, e.g. in quartz [108, 109]. Fol-

[1] In fact, since no stopping site inside a crystal is fully rotationally invariant, the true electron wavefunction is never fully isotropic. However, there are high-symmetry sites in cubic crystals such that the $\widetilde{\mathbf{A}}$ tensor is isotropic. For example, Mu in the tetrahedral site of a diamond lattice is well described by an isotropic $\widetilde{\mathbf{A}}$ matrix.

lowing significant theoretical efforts [110, 111], the anomalous signal in Si was experimentally shown by Kiefl *et al.* to originate from "bond-centered Mu", i.e. a muon located in the center of a Si - Si bond with the unpaired electron equally distributed over the two Si neighbors in a non-bonding orbital [112]. The muon is close to a node in spin density and therefore experiences a hyperfine coupling that is very different from that of isotropic Mu centers with a large hyperfine interaction. Following this discovery, for the first time in any semiconductor, the corresponding bond-centered hydrogen center was observed by several EPR (electron paramagnetic resonance) studies [113–115]. In parallel, Mu dynamics and transitions between various charge states, notably by Kreitzmann *et al.* in Si [116], were investigated, see reviews by Patterson (1988) [117], Chow, Hitti and Kiefl (1998) [39] and Cox (2009) [42] for a more detailed description. For group IV and III-V semiconductors, hydrogen was established as a compensating defect level located deep in the band gap, acting as an amphotheric impurity: in hole-doped (*p*-type) semiconductors, it behaves like a donor, whereas in electron-doped (*n*-type) materials, it acts as an acceptor, always counteracting the effects of the prevailing dopants rather than acting as a source of charge carriers [42, 118].

Therefore, it came as a surprise when van de Walle proposed in 2000 that in ZnO, hydrogen always acts as a shallow donor and thus as a source of *n*-type conductivity [119]. In this context, shallow refers to the close proximity of the donor level (in the band gap) to the conduction band, enabling thermal excitation of the bound electron into the conduction band. Van de Walle's predictions were confirmed with the observation of the corresponding shallow Mu donor state by Cox *et al.* [120] and subsequent ENDOR (electron-nuclear double resonance) studies [121]. These discoveries prompted both a flurry of experiments on shallow Mu centers in non-magnetic oxides, summarized in a review on "oxide muonics" by Cox *et al.* [40, 41], as well as a search for criteria to predict the dopant behavior and charge state of hydrogen impurities, leading to generalized principles for elemental and binary semiconductors [38] and oxides [40, 122–124].

More recent studies focus on Mu centers in transition metal (TM) oxides (TMOs) [125], where, facilitated by the multivalent character of the TM ions[2], excess electrons localize on a TM ion and cause both a change in valence and a local lattice distortion, forming what is called a small polaron [126–128]. In such materials, the charge-neutral muon states often defy classification as either deep or shallow defect states[3] [129], and are best described as polaronic Mu: an oxygen-bound, positive muon, and a small electron polaron located on a nearby TM ion form an overall charge-neutral muon-polaron complex. Such centers have been reported in non-magnetic TMOs including $SrTiO_3$ [130], ZrO_2 [131] and TiO_2 [47, 48].

Here, we focus on the charge-neutral muon center in TiO_2, which, despite detailed μSR and ENDOR studies [46–48], is not completely understood. This chapter was originally conceived as a straightforward introduction into anisotropic charge-neutral muon centers in non-magnetic materials, serving as

[2]ZnO with Zn^{2+} ($3d^{10}$) is an exception due to the completely filled $3d$ states

[3]Muon/H-polaron centers typically lie deep inside the band gap (characteristic of a deep defect). However, in some materials, the charge-neutral center undergoes thermally activated dissociation, i.e. the muon/H and polaron separate, and the electron is promoted into a polaron band and increases the overall carrier density (characteristic of a shallow donor).

a stepping stone for subsequent chapters that discuss analogous centers in magnetic compounds. However, Mu in TiO_2 turned out to be remarkably complex, necessitating a much more in-depth discussion than initially intended. We start by reviewing the theory of anisotropic Mu in Section 4.2. Then, in Section 4.3, the relevant literature on charge-neutral muon centers in TiO_2 is summarized and the open questions are outlined. A proper grasp of polaronic Mu in non-magnetic materials is particularly relevant in light of the main result of this thesis, the discovery of charge-neutral muon-polaron complexes in antiferromagnets (Chapters 5 and 6), where such centers do not exhibit the characteristic signatures of Mu, thus "hiding" their presence. Section 4.4 outlines the experimental details for new detailed μSR measurements on TiO_2, and the results are presented in Section 4.5. Lastly, in Section 4.6, these new data are compared to existing μSR and ENDOR results and previously proposed models, and several alternative models addressing the open questions are proposed and discussed.

4.2 Theory - Anisotropic muonium

In Chapter 3, we discussed a charge-neutral center that was very similar to Mu in vacuum, where the electron is in an atomic $1s$ orbital, and the hyperfine interaction is isotropic and proportional to the unpaired spin density at the muon site. As mentioned above, the electron wave function of charge-neutral centers inside materials is often anisotropic, and the hyperfine interaction has therefore both dipolar and isotropic contributions.

To start, we consider the dipolar interaction of a muon and localized point-like electron separated by the vector $\mathbf{r} = r\hat{\mathbf{n}}$ at distance r along the direction $\hat{\mathbf{n}} = \begin{pmatrix} \sin(\theta)\cos(\phi) \\ \sin(\theta)\sin(\phi) \\ \cos(\theta) \end{pmatrix}$, where θ is the polar angle between $\mathbf{r}$ and $\hat{z}$ and ϕ is the azimuthal angle in the $\hat{x}-\hat{y}$ plane:

$$\mathrm{H} = h\frac{1}{4}A_{dip}[3(\boldsymbol{\sigma}^{\mu}\cdot\hat{\mathbf{n}})(\boldsymbol{\sigma}^{e}\cdot\hat{\mathbf{n}}) - \boldsymbol{\sigma}^{\mu}\cdot\boldsymbol{\sigma}^{e}] = \frac{1}{4}h\boldsymbol{\sigma}^{e}\cdot\widetilde{\mathbf{A}}_{dip}\cdot\boldsymbol{\sigma}^{\mu}. \tag{4.1}$$

$$\text{Here,} \qquad A_{dip} = \frac{\mu_0}{8\pi^2 r^3}\gamma_{\mu}\gamma_{e}\hbar = \frac{250.5}{r[\text{Å}]^3}\,\text{MHz}, \tag{4.2}$$

indicating that the strength of the dipolar interaction is significantly lower than that of the isotropic hyperfine coupling[4]. The dipolar contribution to the hyperfine tensor can be expressed as a traceless symmetric matrix

$$\widetilde{\mathbf{A}}_{dip} = A_{dip}\left[3\begin{pmatrix} \sin(\theta)^2\cos(\phi)^2 & \sin(\theta)^2\cos(\phi)\sin(\phi) & \sin(\theta)\cos(\theta)\cos(\phi) \\ \sin(\theta)^2\cos(\phi)\sin(\phi) & \sin(\theta)^2\sin(\phi)^2 & \sin(\theta)\cos(\theta)\sin(\phi) \\ \sin(\theta)\cos(\theta)\cos(\phi) & \sin(\theta)\cos(\theta)\sin(\phi) & \cos(\theta)^2 \end{pmatrix} - \begin{pmatrix} 1 & 0 & 0 \\ 0 & 1 & 0 \\ 0 & 0 & 1 \end{pmatrix}\right] \tag{4.3}$$

For two interacting point-like particles, $\widetilde{\mathbf{A}}_{dip}$ contains all necessary information to describe the hyperfine coupling, namely the strength of the interaction A_{dip}, which is inversely proportional to the cube of the

[4]For example, for $r = 2$ Å, $A_{dip} = 31$ MHz, more than two orders of magnitude lower than $A_{iso} = 4463.3$ MHz, the hyperfine coupling of Mu in vacuum, where the electron is in an $1s$ atomic orbital.

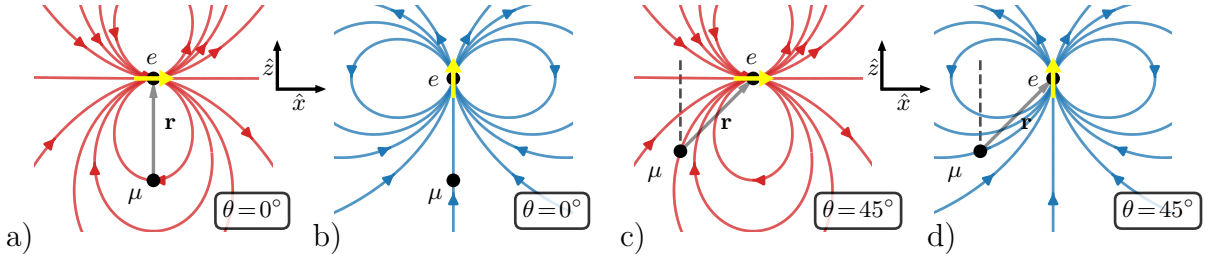

Figure 4.1: Visual representation of the dipolar magnetic field from the electron experienced by the muon for several directions of the electron spin and relative muon-electron positions (see text for details).

distance r, and the relative position of the two spins, parameterized by θ and ϕ. For *any* given spin state of muon and electron, $\widetilde{\mathbf{A}}_{dip}$ determines the dipolar field from the muon experienced by the electron *and* the dipolar field from the electron experienced by the muon.

We illustrate this from the perspective of the muon for two geometries: First we consider $\widetilde{\mathbf{A}}_{dip}$ [Eq. (4.3)] for $\theta = \phi = 0°$, see Fig. 4.1 (a) and (b).

$$\widetilde{\mathbf{A}}_{dip} = A_{dip} \begin{pmatrix} -1 & 0 & 0 \\ 0 & -1 & 0 \\ 0 & 0 & 2 \end{pmatrix} \quad (\theta = 0°) \tag{4.4}$$

If the electron spin points along $\hat{x}$ (i.e. $\langle \sigma_x^e \rangle = 1$, $\langle \sigma_y^e \rangle = \langle \sigma_z^e \rangle = 0$), the dipolar field is proportional to the row highlighted in red, and the muon experiences a field along $-\hat{x}$. If the electron spin points along $\hat{z}$, the dipolar field at the muon site is also along $\hat{z}$ and twice in magnitude [blue row in Eq. (4.4)]. On the other hand, for $\theta = 45°$ and $\phi = 0°$ [Fig. 4.1 (c) and (d)], the hyperfine tensor which describes this geometry has off-diagonal elements:

$$\widetilde{\mathbf{A}}_{dip} = A_{dip} \begin{pmatrix} 0.5 & 0 & 1.5 \\ 0 & -1 & 0 \\ 1.5 & 0 & 0.5 \end{pmatrix} \quad (\theta = 45°,\ \phi = 0°); \tag{4.5}$$

As a result, if the electron spin points along $\hat{x}$, the muon experiences a dipolar field with contributions along $\hat{x}$ *and* $\hat{z}$ [red row in Eq. (4.5), Fig. 4.1 (c)], and the same is true for the electron spin pointing along $\hat{z}$ [blue row in Eq. (4.5), Fig. 4.1 (d)]. We will return to this example in a moment.

Usually, the bound electron is not appropriately described as the point particle considered so far, but has a spatially distributed wave function with electron density $n(\mathbf{r}) = |\psi^e(\mathbf{r})|^2$ [normalized such that $\int^V dV n(\mathbf{r}) = 1$]. In general, the hyperfine tensor has an isotropic contribution, proportional to the electron density at the muon site $n(\mathbf{r}_\mu)$, and a dipolar term, which is essentially the sum over all

infinitesimal volume elements that contain a fraction of the electron spin:

$$\widetilde{\mathbf{A}} = \widetilde{\mathbf{A}}_{iso} + \int^{V} dV n(\mathbf{r}) \widetilde{\mathbf{A}}_{dip}(\mathbf{r}) \tag{4.6}$$

For *any* arbitrary electron wave function, $\widetilde{\mathbf{A}}$ is a real, symmetric matrix[5], and as such is always diagonalizable, i.e. it is possible to find a coordinate system $\hat{X}$, $\hat{Y}$, $\hat{Z}$ in which the hyperfine coupling is described by a diagonal tensor $\widetilde{\mathbf{A}}^D = \begin{pmatrix} A_1 & 0 & 0 \\ 0 & A_2 & 0 \\ 0 & 0 & A_3 \end{pmatrix}$. This so called *principal axis system* (PAS) and the lab frame $\hat{x}$, $\hat{y}$, $\hat{z}$ are linked via an Euler transform described by three rotation angles ϕ, θ, γ (about $\hat{Z}\hat{Y}\hat{Z}$, respectively):

$$\widetilde{\mathbf{A}} = \mathsf{E}(\phi,\theta,\gamma) \widetilde{\mathbf{A}}^D \mathsf{E}(\phi,\theta,\gamma)^{\mathrm{T}}. \tag{4.7}$$

Thus, *any* hyperfine interaction $\widetilde{\mathbf{A}}$ between a muon and an unpaired electron can be fully described by the three hyperfine parameters A_1, A_2 and A_3 and three Euler angles[6]. Experimental determination of these parameters provides detailed information about the electron distribution with respect to the muon and thus the electronic structure of a charge-neutral center. We note that in the example in Fig. 4.1, both geometries ($\theta = 0°$ and $\theta = 45°$) can be described by the *same* $\widetilde{\mathbf{A}}$ tensor; the difference between e.g. Fig. 4.1 (a) and (c) is the choice of coordinate system (affecting the *representation* of $\widetilde{\mathbf{A}}$) and the electron spin state relative to $\mathbf{r}$ (affecting which *components* of $\widetilde{\mathbf{A}}$ are relevant). Independent of the coordinate system, the isotropic part of $\widetilde{\mathbf{A}}$ is given by

$$A_{iso} = \frac{1}{3} \mathrm{Tr}\left(\widetilde{\mathbf{A}}\right). \tag{4.10}$$

For a general hyperfine coupling described by A_1, A_2, A_3, ϕ, θ, γ, and the initial muon spin polarization along $\hat{z}$, the time evolution of the polarization $\left\langle \sigma_z^{\mu}(t) \right\rangle$ in the absence of an applied magnetic field is

$$\begin{aligned} \left\langle \sigma_z^{\mu}(\phi,\theta,\gamma,t) \right\rangle \;=\; & \tfrac{\cos^2(\theta)}{2}\left[\cos\left(\tfrac{\omega_1-\omega_2}{2}t\right) + \cos\left(\tfrac{\omega_1+\omega_2}{2}t\right)\right] + \\ & \tfrac{\sin^2(\theta)}{2}\left(\tfrac{\cos^2(\gamma)}{2}\left[\cos\left(\tfrac{\omega_2-\omega_3}{2}t\right) + \cos\left(\tfrac{\omega_2+\omega_3}{2}t\right)\right] + \tfrac{\sin^2(\gamma)}{2}\left[\cos\left(\tfrac{\omega_1-\omega_3}{2}t\right) + \cos\left(\tfrac{\omega_1+\omega_3}{2}t\right)\right]\right), \end{aligned} \tag{4.11}$$

[5]The isotropic part is proportional to the identity matrix, and the dipolar contribution, as a sum of traceless real symmetric matrices, is a traceless real symmetric matrix.

[6]Often, symmetries in the electron wave function simplify $\widetilde{\mathbf{A}}$. For example, the dipolar contribution of a axially symmetric electron distribution (experienced e.g. by bond-centered muon in Si [112]) is mathematically equivalent to that of a single point-like electron located on the symmetry axis and can be fully determined by four parameters. In its principal axis system (defined by θ and ϕ), such rotationally symmetric center can be described by

$$\widetilde{\mathbf{A}} = A_{iso}\mathbb{1}_3 + A_{dip}\begin{pmatrix} -1 & 0 & 0 \\ 0 & -1 & 0 \\ 0 & 0 & 2 \end{pmatrix} = \begin{pmatrix} A_{iso}-A_{dip} & 0 & 0 \\ 0 & A_{iso}-A_{dip} & 0 \\ 0 & 0 & A_{iso}+2A_{dip} \end{pmatrix} = \begin{pmatrix} A_{\perp} & 0 & 0 \\ 0 & A_{\perp} & 0 \\ 0 & 0 & A_{\parallel} \end{pmatrix}, \tag{4.8}$$

i.e. measurement of the hyperfine coupling perpendicular ($A_{\perp}$) and parallel ($A_{\parallel}$) to the symmetry axis allows the determination of A_{iso} and A_{dip}:

$$A_{iso} = \tfrac{1}{3}(A_{\parallel} + 2A_{\perp}), \quad A_{dip} = \tfrac{1}{3}(A_{\parallel} - A_{\perp}) \tag{4.9}$$

where $\omega_i = 2\pi A_i$. Unlike in the isotropic case [Eq. (3.3)], there up to four degenerate energy levels and thus up to six distinct transition frequencies.

In the presence of applied magnetic fields, the Hamiltonian is simply

$$\mathrm{H} = \tfrac{h}{4}\boldsymbol{\sigma}^e \cdot \widetilde{\mathbf{A}} \cdot \boldsymbol{\sigma}^\mu + \tfrac{\hbar}{2}\gamma_e \mathbf{B}\cdot\boldsymbol{\sigma}^e - \tfrac{\hbar}{2}\gamma_\mu \mathbf{B}\cdot\boldsymbol{\sigma}^\mu. \tag{4.12}$$

We focus our discussion on the limit where the electron Zeeman term dominates over the muon-electron hyperfine interaction, i.e. the decoupled limit. Compared to Mu in vacuum the magnitude of the hyperfine interaction in anisotropic Mu centers is often orders of magnitudes smaller, and much lower magnetic fields are required for decoupling. For example, in TiO_2, the subject of this chapter, the hyperfine coupling is of the order of 1 MHz, and magnetic fields of the order of 1 mT (10 G) are sufficient for decoupling. In that limit, the unpolarized electron is time-independent and can take on one of two possible spin states; either along or opposite to the applied field direction $\mathbf{b} = \mathbf{B}/|\mathbf{B}|$. We can therefore replace the electron spin operator with its possible outcomes, which reduces the Hamiltonian to a 2×2 matrix describing the muon spin only; the effect of the electron spin on the muon can be expressed as an *effective* magnetic field [39, 105, 132], which acts in addition to the applied magnetic field:

$$\mathrm{H} = -\tfrac{\hbar}{2}\gamma_\mu \boldsymbol{\sigma}^\mu \cdot \mathbf{B} \pm \tfrac{h}{4}\mathbf{b}\cdot\widetilde{\mathbf{A}}\cdot\boldsymbol{\sigma}^\mu = -\tfrac{\hbar}{2}\gamma_\mu\boldsymbol{\sigma}^\mu\cdot(\mathbf{B}-\mathbf{B}^{\mathrm{eff}}), \tag{4.13}$$

$$\text{with} \quad \mathbf{B}^{\mathrm{eff}} = \pm\frac{2\pi}{\gamma_\mu}\frac{1}{2}\mathbf{b}^{\mathrm{T}}\cdot\widetilde{\mathbf{A}}, \tag{4.14}$$

where the $\pm$ corresponds to the electron spin vector either pointing along or opposite the magnetic field. In essence, the direction of the magnetic field $\mathbf{b}$ determines the electron spin state and thus the hyperfine field experienced by the muon [compare e.g. Fig. 4.1 (a) and (b)]. The muon spin precesses in the combined (total) magnetic field $\mathbf{B}^{\mathrm{tot}}$

$$\mathbf{B}^{\mathrm{tot}}_{\pm} = \mathbf{B} \mp \frac{2\pi}{\gamma_\mu}\frac{1}{2}\mathbf{b}^{\mathrm{T}}\cdot\widetilde{\mathbf{A}}, \text{ at a frequency } \nu_\pm = \frac{\gamma_\mu}{2\pi}|\mathbf{B}^{\mathrm{tot}}_{\pm}| = |\frac{\gamma_\mu}{2\pi}\mathbf{B} \mp \frac{1}{2}\mathbf{b}^{\mathrm{T}}\cdot\widetilde{\mathbf{A}}|. \tag{4.15}$$

In general, the relative orientation of the applied magnetic field $\mathbf{B}$ and hyperfine tensor informs which components of $\widetilde{\mathbf{A}}$ have an impact on the observable frequencies[7]. A systematic application of magnetic fields along various crystal directions can then be used to accurately determine the hyperfine tensor, as will be demonstrated later in this chapter.

Conventionally, $\hat{z}$ is chosen to coincide with the applied field direction and held fixed while $\widetilde{\mathbf{A}}$ is rotated to map out different projections of the hyperfine tensor. However, given the complexity of charge-neutral muon centers in TiO_2, we deviate from this convention and instead choose a coordinate system that coincides with the crystalline directions. For a given coordinate system $\hat{x}$, $\hat{y}$, $\hat{z}$, Eq. (4.15)

[7]Here, we consider a simple example: $\widetilde{\mathbf{A}} = 1\,\mathrm{MHz}\left(\begin{smallmatrix}2&0&0\\0&1&0\\0&0&0\end{smallmatrix}\right)$, with the principal axis system coinciding with the lab frame (i.e $\phi = \theta = \gamma = 0$). For $\mathbf{B} \parallel \hat{x}$ (i.e. $\mathbf{b} = \left(\begin{smallmatrix}1\\0\\0\end{smallmatrix}\right)$), the observable frequencies are $\nu_\pm = \frac{\gamma_\mu}{2\pi}|\mathbf{B}| \mp 1\,\mathrm{MHz}$; likewise, for $\mathbf{B} \parallel \hat{y}$,$\nu_\pm = \frac{\gamma_\mu}{2\pi}|\mathbf{B}| \mp 0.5\,\mathrm{MHz}$, while for $\mathbf{B} \parallel \hat{z}$ there is only a single frequency at $\nu = \frac{\gamma_\mu}{2\pi}|\mathbf{B}|$ since $A_3 = 0$.

is valid for *any* direction of the applied field $\mathbf{b} = \begin{pmatrix} \sin(\Theta)\cos(\Phi) \\ \sin(\Theta)\sin(\Phi) \\ \cos(\Theta) \end{pmatrix}$, where Θ and Φ are the conventional polar and azimuthal angles, and *any* direction of the hyperfine tensor $\widetilde{\mathbf{A}}$, parameterized by ϕ, θ, γ [Eq. (4.7)].

In general, the effective hyperfine field is *not* along the applied field direction. This can lead to somewhat counter-intuitive situations for non-magnetic materials, in which in LF geometry (where the magnetic field is applied along the initial spin polarization $\mathbf{P}_i$), no oscillatory signals are typically expected, whereas for TF geometry ($\mathbf{B} \perp \mathbf{P}_i$), the full signal is expected to oscillate. There are two possible scenarios. If the magnetic field is applied along a principal direction of the hyperfine tensor, the effective hyperfine field is *only* along the direction of the applied field, and the expectations are met: the TF signal fully oscillates at both ν_+ and ν_-, and the LF signal is non-oscillatory, see left side of Fig. 4.2. However, if the applied field is *not* along a principal component of $\widetilde{\mathbf{A}}$, the effective hyperfine field has a component perpendicular to the applied field [Eq. (4.5)]; as a result, there can be a sizable oscillatory component in LF and non-oscillatory component in TF [see right side of Fig. 4.2]. Fig. 4.1 also illustrates this point.

Lastly, we discuss a specific case for $\widetilde{\mathbf{A}}$ that is relevant for the analysis of the TiO_2 data: the A_3 principal axis is along $\hat{z}$ (i.e. $\theta = 0$ and $\gamma = 0$). In this case, the orientation of $\widetilde{\mathbf{A}}$ is fully determined by a single angle ϕ. This dramatically simplifies Eqs. (4.7) and (4.15), and for an applied field described by Θ and Φ, the total field experienced by the muon is given by:

$$\mathbf{B}_{\pm}^{\text{tot}} = |\mathbf{B}| \begin{pmatrix} \sin(\Theta)\cos(\Phi) \\ \sin(\Theta)\sin(\Phi) \\ \cos(\Theta) \end{pmatrix} \mp \frac{2\pi}{\gamma_\mu} \frac{1}{2} \begin{pmatrix} \sin(\Theta)[(A_1 - A_2)\cos(\phi)\sin(\phi)\sin(\Phi) + \cos(\Phi)(A_1\cos(\phi)^2 + A_2\sin(\phi)^2)] \\ \sin(\Theta)[A_2\cos(\phi)^2\sin(\Phi) + (A_1 - A_2)\cos(\Phi)\cos(\phi)\sin(\phi) + A_1\sin(\Phi)\sin(\phi)^2] \\ A_3\cos(\Theta) \end{pmatrix} \quad (4.16)$$

Rotating $\mathbf{B}$ in the $\hat{x} - \hat{y}$ plane corresponds to fixing $\Theta = \pi/2$ and changing Φ; the frequencies $\nu_\pm = \frac{\gamma_\mu}{2\pi}|\mathbf{B}_\pm^{\text{tot}}|$ are given by

$$\nu_\pm = \sqrt{(\tfrac{\gamma_\mu}{2\pi}|\mathbf{B}|)^2 \mp \tfrac{1}{2}(A_1 + A_2) \mp \tfrac{1}{8}\cos(2(\Phi - \phi))[(A_1 - A_2)(4B \mp (A_1 + A_2))] + \tfrac{1}{8}(A_1^2 + A_2^2)} \quad (4.17)$$

Likewise, the frequencies for rotating $\mathbf{B}$ in the $\hat{x} - \hat{z}$ plane are given by $\Phi = 0$ and variation of Θ:

$$\nu_\pm = \sqrt{\cos(\Theta)^2\left(B \mp \tfrac{1}{2}A_3\right)^2 + \sin(\Theta)^2\left((\tfrac{\gamma_\mu}{2\pi}|\mathbf{B}|) \mp \tfrac{1}{2}(A_1\cos(\phi)^2 + A_2\sin(\phi)^2)) + \tfrac{1}{16}(A_1 - A_2)^2\sin(2\phi)^2\right)} \quad (4.18)$$

We note that while the effective-field approximation is extremely helpful to gain intuition, the exact diagonalization of (4×4) Hamiltonians is computationally inexpensive. Therefore, the results for all theoretical models shown in this chapter are obtained from exact numeric solutions of the relevant Hamiltonians and subsequent transformations into the general expression of the muon spin polarization [Eq. (2.19)].

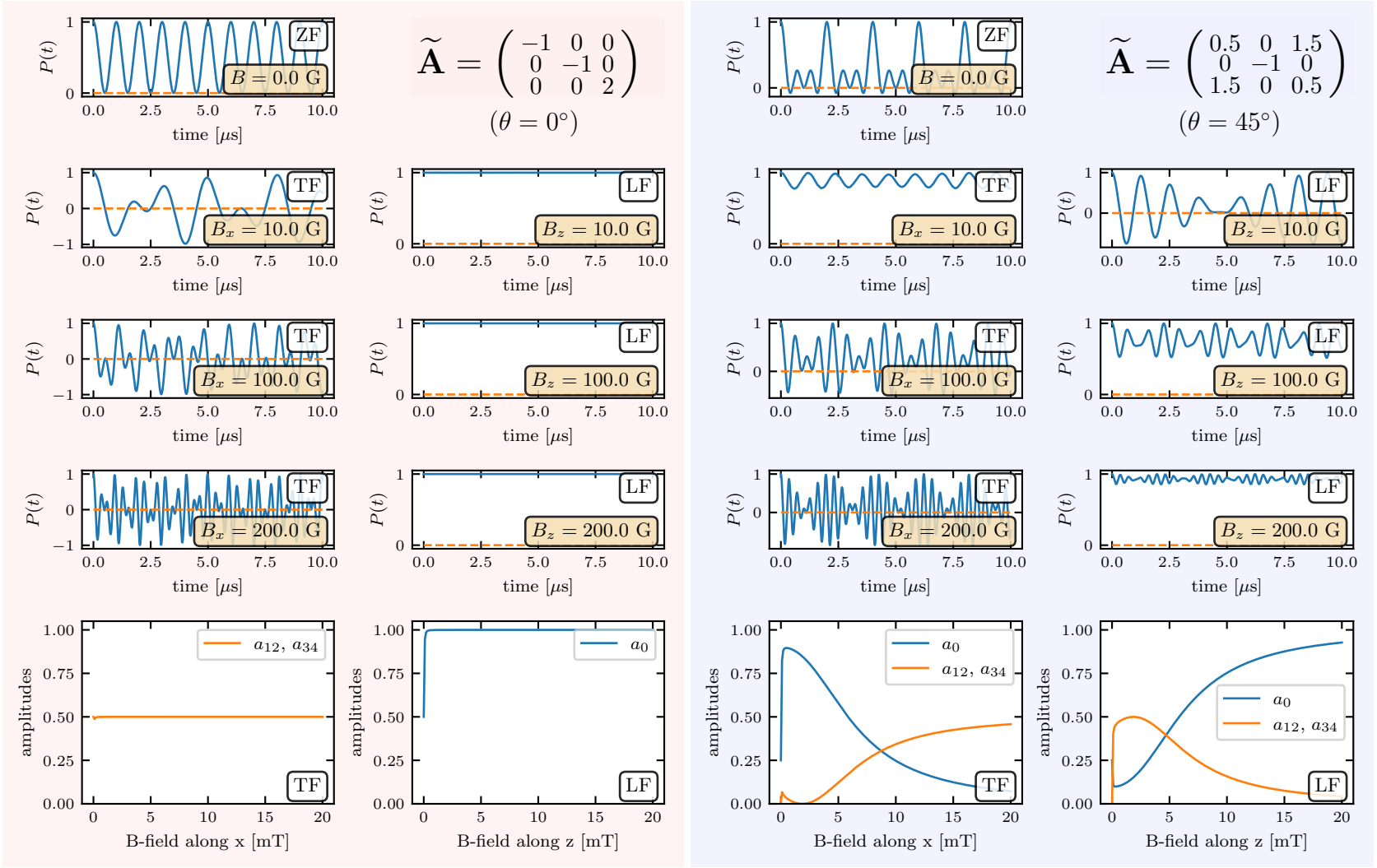

Figure 4.2: Polarization spectra with the initial polarization $\mathbf{P}_i$ along z in zero field (ZF) and for fields applied along x (TF) an z (LF) for dipolar tensors with $\theta = 0°$ (left side, red background) and $\theta = 45°$ (right side, blue background) [compare Fig. 4.1]. Additionally, the amplitudes of the oscillatory (a_{12}, a_{34}) and non-oscillatory (a_0) components are shown. For $\theta = 0°$, fields along x an z are along principal directions of $\widetilde{\mathbf{A}}$, the effective hyperfine field is along the direction of the applied field; typical behavior expected for TF (x) and LF (z) is displayed. For $\theta = 45°$, the effective hyperfine field has a significant component perpendicular to the applied field, causing oscillations in LF and non-oscillatory components in TF (see text for details).

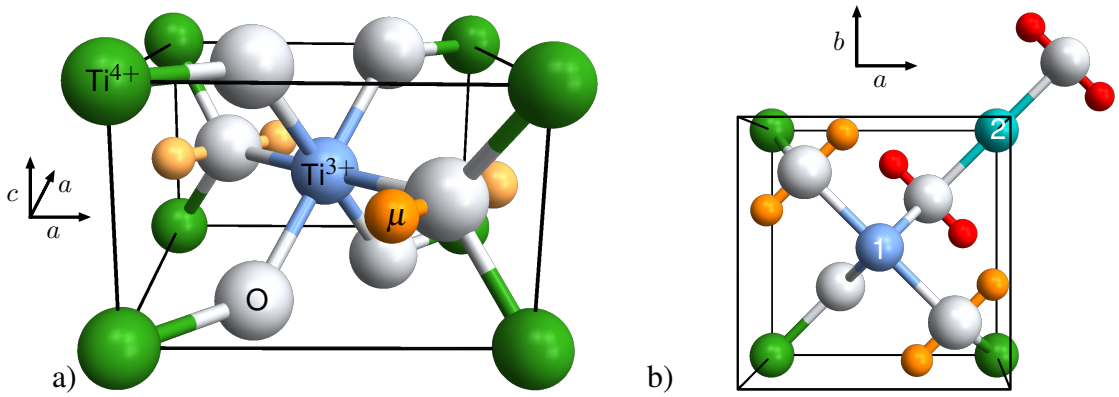

Figure 4.3: (a) Crystal structure of TiO_2, with likely muon (or hydrogen) site in orange and proposed location of the Ti^{3+} (polaron) ion in blue. Light orange spheres represent electrostatically equivalent muon stopping sites. (b) All Ti ions are electrostatically equivalent. The polaron may also localize on a corner Ti ion (Ti 2), resulting in an additional set of four possible muon sites (red spheres), rotated by 90° about the *c*-axis compared to the four possible (orange) sites if the polaron is localized on Ti 1.

.

4.3 Titanium oxide

Rutile titanium oxide (TiO_2), a semiconducting transition metal oxide with rutile structure (space group $P4_2/mnm$) [see Fig. 4.3], a large dielectric constant [133, 134] and a band gap of $\sim 3.0\,eV$ [135], has a wide range of technological applications, including photocatalysis [136], solar energy harvesting [137, 138] and lithium ion batteries [139, 140]. Furthermore, TiO_2 is widely considered as a prototypical polaronic material [128, 141, 142], in which small polaron formation is well established: excess electrons localize on one Ti ion, causing both a change in valence from Ti^{4+} ($3d^0$) to Ti^{3+} ($3d^1$) and a local lattice distortion. Like any semiconductor, the electronic properties of TiO_2 are sensitive to the presence of impurities (unintentional) and dopants (intentional). Hydrogen (H) is one of the most prevalent impurities, and there is wealth of literature discussing its dopant behavior [128, 143], based on both experiment [46–48, 144–153] and theory [129, 154–161]. There are strong indications that H causes *n*-type conductivity, however its precise role - e.g. whether interstitial H [144, 152, 153, 155] or H in an oxygen vacancy [158] is the main donor - is still under debate. This is further complicated by the observation that H may incorporate differently depending on *how* the sample is hydrogenated [147]; different experiments may therefore investigate different H-related defect centers.

Direct access to the electronic structure of charge-neutral hydrogen complexes was provided by Brant *et al.* using EPR and ENDOR [46]. A detailed ENDOR orientation dependence determined the hyperfine tensor of the charge-neutral center to have principal components of $A_1 = -0.40(1)\,MHz$, $A_2 = 0.62(1)\,MHz$, $A_3 = -0.34(1)\,MHz$, with A_3 directed along the crystalline *c*-axis and A_1 enclosing an angle of $\phi_0 = 22.9°$ with [110]. The authors conclude that "the unpaired electron is localized, to a first approximation, on one titanium ion immediately adjacent to the OH- ion" [46] and propose the structure

as shown in Fig. 4.3 (a). However, as discussed below, this model predicts a hyperfine interaction about 20 times larger than what is experimentally observed.

Two separate μSR studies, published near-simultaneously, followed the ENDOR measurements. Based on the correspondence between charge-neutral hydrogen and muon centers, a Mu center with an $\widetilde{\mathbf{A}}$ tensor with principal components $A_1 = -1.28(3)\,\mathrm{MHz}$, $A_2 = 1.96(3)\,\mathrm{MHz}$, $A_3 = -1.08(3)\,\mathrm{MHz}$ (scaled by $\gamma_\mu/\gamma_p = 3.18$, the ratio of the muon and proton gyromagnetic ratios) is expected, with possible deviations anticipated from the difference in mass and thus zero point motion (ZPM).

Vilão *et al.* [47] published a detailed temperature dependence of the Mu signal in 20 mT $\parallel$ [110]. The observed splittings at 1.2 K are within 15% of the predicted values based on the ENDOR A_1 and A_2 results. Measurements along [001] (c-axis) reveal A_3 being close to zero, which the authors attribute to the muon's larger ZPM. The authors conclude that the charge-neutral centers observed by μSR and ENDOR have an identical electronic structure within experimental uncertainties [Fig. 4.3 (a)]. A strong temperature dependence is observed - the four Mu satellite lines observed at 1.2 K merge into two above 4 K - and attributed to thermally activated muon hopping to excited states [see Fig. 3 in Ref. [47]].

Shimomura *et al.* [48] report a detailed orientation dependence of the Mu hyperfine coupling at 5 K. Although the data is not fully described by their model and there are indications of sample misalignment, they obtain an $\widetilde{\mathbf{A}}$ matrix with principal values $A_1 = -A_2 = 1.29\,\mathrm{MHz}$ in the c-plane enclosing $\phi_0 = 19.5°$ with [110], and $A_3 = 0.17\,\mathrm{MHz}$ along the c-axis. Given the discrepancies to the ENDOR results, the authors speculate that the ENDOR data originated from hydrogen in an oxygen vacancy, whereas the muon occupies an interstitial site; i.e. the two techniques observe different centers. Noting that an electron that is fully localized on the nearest Ti ion, as proposed by Brant *et al.* [46], would result in a hyperfine coupling that is considerably larger than what is experimentally observed, the authors suggest that the bound electron is significantly delocalized. The near-zero A_3 value is explained with a model where spin polarization of opposite sign is induced on the oxygen that the muon binds to. While elegant, this model only describes the data for a minute fraction (5%) of the bound electron localizing on the nearby Ti ion, and we are not aware of any theory results that support this model. In addition, we note that it is clear from the temperature dependence observed by Vilão, that at 5 K, dynamical processes significantly impact the μSR spectrum, and the $\widetilde{\mathbf{A}}$ matrix obtained by Shimomura *et al.* does not reflect the ground state of the observed charge-neutral center.

Reviewing the available μSR and ENDOR data, two main aspects of the observations remain unexplained:

- As Shimomura *et al.* note, the hyperfine coupling expected from a fully localized electron on an adjacent Ti ion is far larger than the observed coupling. Using a μ-Ti^{3+} distance of $\sim 2.2\,\text{Å}$, Eq. (4.3) predicts principal values of $A_1 \approx 46\,\mathrm{MHz}$, $A_2 \approx -23\,\mathrm{MHz}$ and $A_3 \approx -23\,\mathrm{MHz}$ for the muon center (scaled by $\frac{1}{3.18}$ for the hydrogen center), i.e. about 20 times larger than the actual observed magnitude for *both* the charge-neutral muon and hydrogen center. Even if partial delocalization of the electron is considered, the proposed electronic structure is incompatible with the μSR and ENDOR measurements.

- The A_3 principal component of the charge-neutral center is close to zero in the μSR experiments, but non-zero (and comparable to A_1) in the ENDOR measurement. Zero-point motion, as proposed in Ref. [47], cannot account for this difference in A_3, as we show below (in Section 4.6).

This leads to two unresolved questions: (1) What is the precise nature and electronic structure of charge-neutral muon and hydrogen centers in TiO_2, and (2) why do the μSR and ENDOR results differ?

Answering these questions is important since μSR is often used to characterize the electronic structure and dopant characteristics of isolated interstitial hydrogen. However, the correspondence is rarely shown directly, and TiO_2 is one of few cases where detailed information from *both* muon and H centers are available; a full explanation for the apparent discrepancy between μSR and ENDOR is therefore necessary. Furthermore, in Chapter 5 and 6, evidence for charge-neutral muon-polaron complexes in magnetic transition metal oxides is presented. Importantly, in contrast to Mu in non-magnetic materials, the characteristic Mu signatures are absent in magnetic compounds, which obscures the presence of charge-neutral centers. Given the muon's widespread use as a sensitive probe of magnetism, it is critical to develop a general understanding under what circumstances and in what form muon-polaron complexes form, both in magnetic and non-magnetic materials.

Aiming to address the open questions, we revisited TiO_2 and carried out a detailed orientation dependence and determine the $\widetilde{\mathbf{A}}$ matrix at 1.9 K, a temperature where Ref. [47] suggests that dynamics do not dominate the μSR spectra. The results of the orientation dependence were corroborated by the observation of characteristic longitudinal field oscillations in the effective hyperfine field of the bound electron spin. Noting the different experimental magnetic fields for ENDOR (0.35 T) and previous μSR experiments (< 0.04 T), we also carried out a field scan up to 0.4 T to exclude the possibility that the difference in A_3 is caused by differences in the external field.

4.4 Experimental details

The μSR experiments were carried out in the LAMPF spectrometer at the M20 beamline at TRIUMF (Vancouver, Canada). The temperature was controlled with a He gas-flow cryostat ("Miss Piggy"); all data presented here were acquired at 1.9 K. Two Verneuil grown single crystal TiO_2 specimens of dimensions $10 \times 10 \times 0.5\,\mathrm{mm}^3$, sourced from Crystal GmbH (Berlin, Germany), were used: $C1$ with [001] out of plane and [110] and [1$\bar{1}$0] aligned along the edges, and $C2$ with [100] out of plane, and [010] and [001] aligned along the edges. In the following, the [001] direction is also referred to as c-axis, whereas the equivalent [100] and [010] directions are also called a-axes. A dedicated sample holder that allows in-plane rotations of the sample [Fig. 4.4] was designed and built in order to study the orientation dependence of the μSR spectra. The measurements were taken in the spin-rotated mode, with the initial spin polarization $\mathbf{P}_i$ along $\hat{x}$ (perpendicular to the beam direction $\hat{z}$) and a magnetic field of 11.5 mT applied along $\hat{y}$, in the plane of the samples. Both crystals were investigated: $C1$ was rotated about the c-axis between $0-45°$ (i.e. in the $a-a$ plane), and $C2$ was rotated about an a-axis between $0-90°$ (i.e. in the $a-c$ plane). These crystal rotations in a fixed $\mathbf{B}$-field are equivalent to keeping the

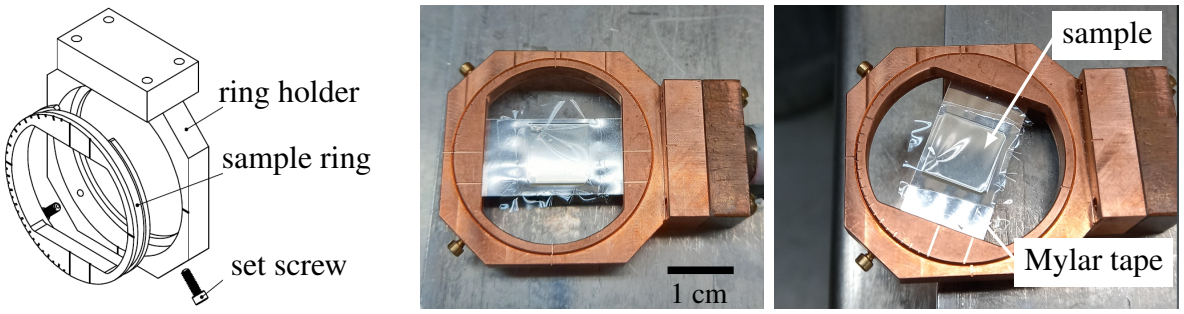

Figure 4.4: Rotatable sample holder: the sample is mounted on a piece of Mylar tape which is attached on a freely rotatable ring, allowing changes in the relative orientation between applied magnetic fields and crystal. Drawing by Mike McLay, pictures taken by the author.

.

crystal fixed and rotating **B** with respect to the crystal. We adopt this perspective for the analysis below and define Θ and Φ as the polar and azimuthal angles enclosed by **B** and the crystal coordinate system. The experimental uncertainties in the rotation angle are estimated to be within $\pm 1°$. Additionally, using the standard "Miss Piggy" sample holder, a transverse field scan between $0.01 - 0.4\,\mathrm{T}$ along the c-axis was carried out in $C1$ with the applied field along $\hat{z}$. Finally, a longitudinal field scan with both inital spin polarization and the applied field along $\hat{z}$ was carried out for fields up to 10 mT for $C1$ (**B** $\parallel$ [001]) and for fields up to 30 mT for $C2$ (**B** $\parallel$ [100]).

4.5 Results

Representative polarization spectra in the time domain for two different field directions are shown in Fig. 4.5. A characteristic beating pattern is observable for **B** $\parallel$ [100], indicating several frequency components, whereas only a weakly damped single-frequency spectrum is obtained for **B** $\parallel$ [001]. More insight can be gained from Fourier transforms (FT) of the μSR spectra, see Fig 4.6 (a) for rotations of **B** in the $a-a$ plane and Fig 4.7 (a) for rotations in the $a-c$ plane. Fig 4.6 (a) is consistent with eight individual (but sometimes overlapping) Mu satellite lines. These multiple frequencies can be explained as follows: for any given charge-neutral complex configuration, characterized by A_1, A_2, A_3, θ, ϕ, γ, there are several electrostatically equivalent sites based on symmetry considerations. A preliminary data analysis and inspection of Figs. 4.5 (b) and 4.7 (a) indicate that the A_3 principal component is along the c-axis, consistent with the previous μSR [47, 48] and ENDOR [46] experiments. Therefore, in the subsequent analysis, A_3 is set to be along c[8]. This greatly simplifies the description of electrostatically equivalent sites [see Eq. (4.16)]: A_1 and A_2 must then lie within the $a-a$ plane, and their direction is fully described by a single angle ϕ.

The example configurations in Fig. 4.3 (b) demonstrate that for a given center described by A_1, A_2,

[8]Other options were considered, but no satisfactory results could be obtained.

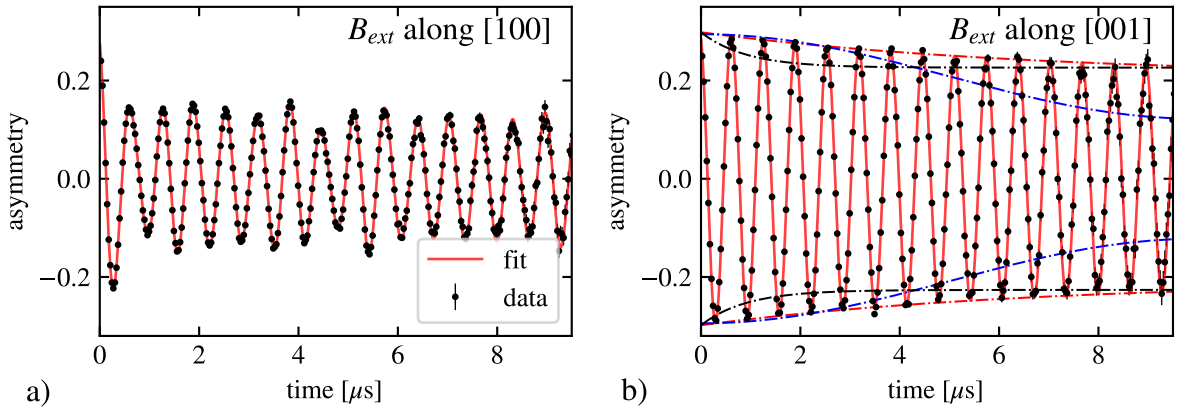

Figure 4.5: Muon spin polarization spectra at 1.9 K in 11.5 mT for (a) **B** ∥ [100] and (b) **B** ∥ [001]. Beating patterns characteristic for a frequency multiplet due to an anisotropic hyperfine interaction are evident for **B** ∥ [100], whereas the spectrum for **B** ∥ [001] only shows signs of weak depolarization. The dash-dotted lines represent various models detailed in the text.

.

A_3 and ϕ_0, there are a total of eight electrostatically equivalent configurations with possible angles

$$\phi = \pm\phi_0, \pm\phi_0 + \frac{\pi}{2}, \pm\phi_0 + \pi, \pm\phi_0 + \frac{3\pi}{2}, \tag{4.19}$$

where ϕ_0 is defined as the angle enclosed by A_1 and the [110] direction. In an applied field of 11.5 mT, the electron spin is fully decoupled; for a given charge-neutral center, two frequencies are expected $\nu_\pm$ [Eq. (4.15)] corresponding to the electron spin vector either pointing along or opposite to the applied field (i.e. ν_{12} and ν_{34}). However, since the induced hyperfine field depends on the *relative* orientation of the hyperfine tensor of a given charge-neutral center and the field direction, the hyperfine splitting is different for various electrostatically equivalent sites, explaining the observed multiplet splitting. For the case where the A_3 principal axis is along c, Eqs. (4.17) and (4.18) indicate that angles ϕ and $\phi + \pi$ result in the same frequencies; there are only up to four unique configurations described by $\phi = \pm\phi_0, \pm\phi_0 + \frac{\pi}{2}$, resulting in up to eight distinct Mu lines.

The data set describing the $a - a$ plane rotations [Fig. 4.6] is fit to a sum of exponentially damped oscillatory signal components [Eq. (2.9)]. Additionally, a small exponentially relaxing non-oscillatory signal [Eq. (2.10)] accounting for a small component of the effective field along the initial muon spin polarization was included. All oscillatory components share a common phase. The Mu satellite lines are described by up to eight oscillatory signals with a common relaxation rate and individual amplitudes. A non-relaxing component at the Larmor frequency accounts for those muons that do not form a charge-neutral center. However, no satisfactory fit could be obtained unless an additional, broad ($\sim 1\,\mu\mathrm{s}^{-1}$) component at the Larmor frequency is included. The fitted Mu frequencies are shown in Fig. 4.6 (b). The Hamiltonian for anisotropic Mu [Eq. (4.12)] was solved numerically for the ensemble of symmetry equivalent sites; the solid lines in Fig. 4.6 (b) represents the best match following a numeric minimiza-

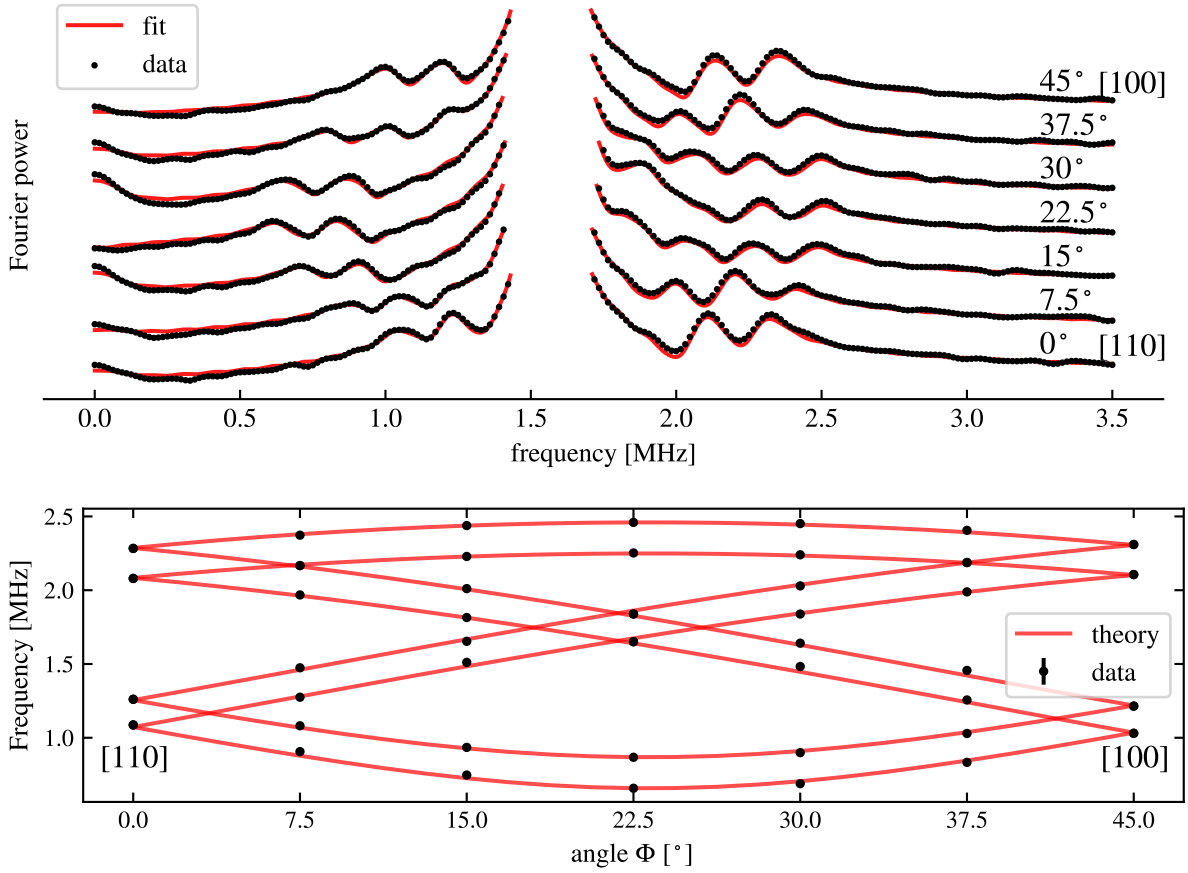

Figure 4.6: (a) Fourier transforms of μSR spectra at various angles of **B** within the $a-a$ plane. (b) Fitted frequencies (black dots) alongside theoretical description (red lines); see text for details. Statistical uncertainties are smaller than the marker size.

.

tion (optimizing A_1, A_2 and ϕ_0), yielding $A_1 = 1.81(1)$ MHz and $A_2 = -1.37(1)$ MHz, with A_1 enclosing an angle $\phi_0 = 23.2(1)°$ with the [110].

For the rotation in the $a-c$ plane, the spectra are fit to up to four oscillatory components [Eq. (2.9)] with shared amplitudes and relaxation rates accounting for the Mu lines, and two signals at the Larmor frequency, one non-relaxing and one relaxing component, the latter accounting for the unexpected additional component previously mentioned. All oscillatory signals share the same phase. The model constraints on the Mu lines are intentionally restrictive to allow extraction of relevant parameters for large rotation angles where the lines merge into a single signal. Additionally, at 67.5° and 90° the Mu amplitude and relaxation rate, as well as the amplitude of the non-relaxing component at the Larmor frequency, were fixed to the value obtained for **B** $\parallel$ [100] (0°). The obtained frequencies are shown in Fig. 4.7 (b), alongside theory predictions [solid lines]. Unlike the lines in Fig. 4.6 (b), the lines here are not obtained from a numeric minimization but are simply the calculated frequencies for the full

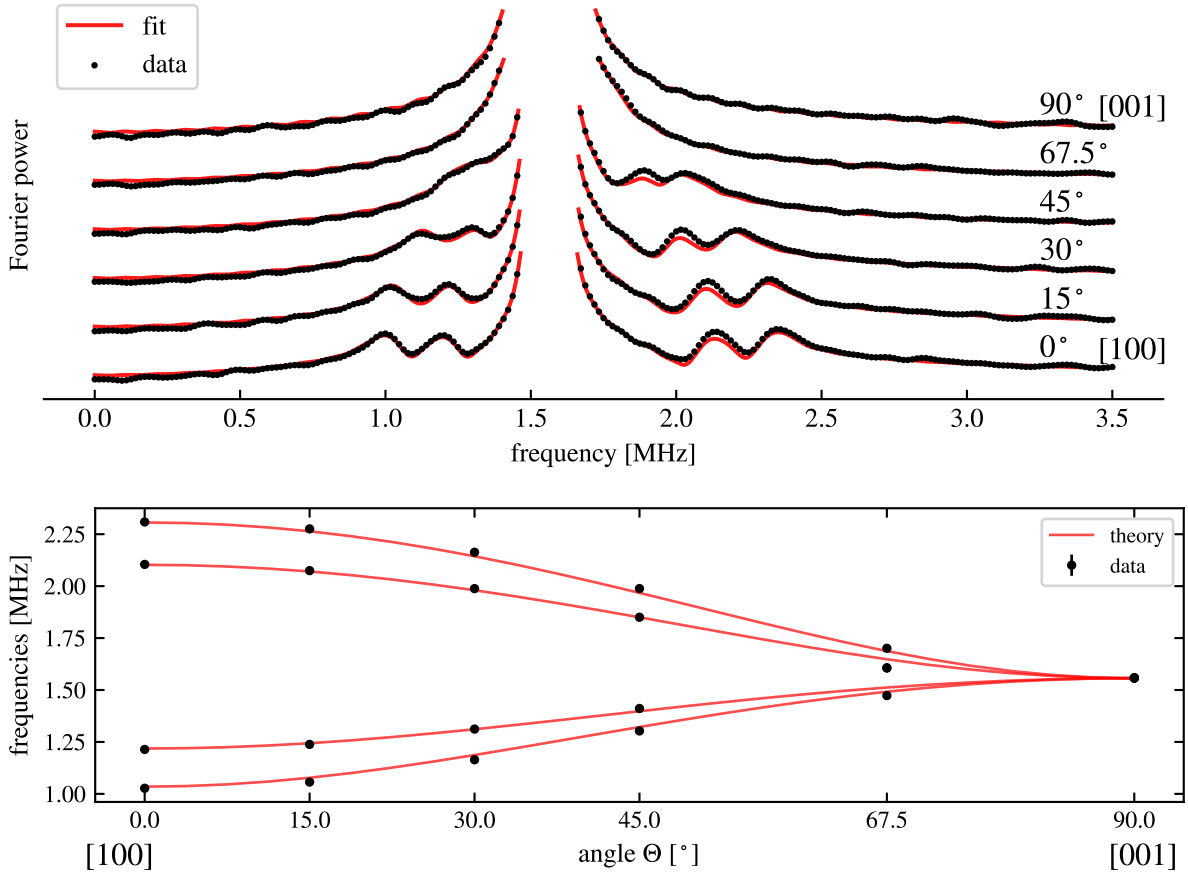

Figure 4.7: (a) Fourier transforms of μSR spectra at various angles of **B** within the $a-c$ plane. (b) Fitted frequencies (black dots) alongside theoretical model (red lines); see text for details. Statistical uncertainties are smaller than the marker size.

Hamiltonian using $A_3 = 0$ and the A_1, A_2 and ϕ_0 values obtained the $a-a$ rotation. Good agreement is obtained, indicating a consistent model.

The run with $\mathbf{B} \parallel c$ [Fig. 4.5 (b)] warrants further discussion. If A_3 were non-zero, a splitting into a single pair of Mu satellite lines would be expected [Eq. (4.18) for $\Theta = 0°$], causing a characteristic frequency beating. This is not observed: only a single frequency is evident. To further illustrate this point, the blue dash-dotted line represents the signal envelope for a hypothetical value for $A_3 = 0.1\,\mathrm{MHz}$ assuming the same signal amplitude ratios as obtained for $\mathbf{B} \parallel [100]$ and that there is *no* damping for any component. This model clearly misses the data, and we can confidently conclude that $A_3 < 0.1\,\mathrm{MHz}$. Furthermore, we note that the observed small damping could either be due to the relaxing Mu component or the broad component at the Larmor frequency, however *not* both: The dash-dotted black line shows the envelope for only the Larmor component relaxing, whereas the dash-dotted red line only shows the envelope for only the Mu component being damped; for both, the amplitude ratios and damping rates obtained for $\mathbf{B} \parallel [100]$ were used. It is evident that the data is better described by the relaxing

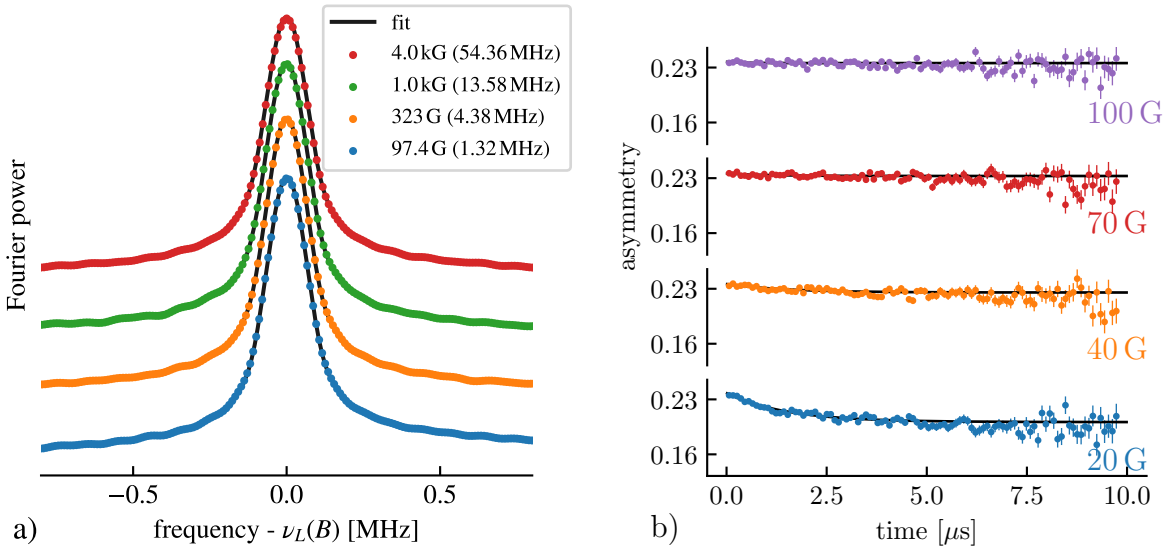

Figure 4.8: (a) Fourier transforms of TF-μSR spectra at various fields applied along c, each centered at the respective Larmor frequency. It is evident that the line width does not change with field, excluding the possibility of a field-dependent A_3 component. (b) Longitudinal field scan for $\mathbf{B} \parallel [001]$

Mu component, indicating that the damping rate of the Larmor component must be much smaller for $\mathbf{B} \parallel [001]$ than for $\mathbf{B} \parallel [100]$. This apparent orientation-dependent change in the damping rate of the Larmor component suggests that the broadening of this component is of electronic origin.

The small value of A_3 is consistent with previous μSR studies but contrary to the expectations from the ENDOR experiment. Noting that the ENDOR data were taken at 0.35 T whereas all available μSR data were acquired in fields smaller than 0.035 T, a field scan with $\mathbf{B} \parallel [001]$ was taken between $0.1 - 0.4$ T to exclude the possibility of a field-induced modification to the hyperfine coupling which could explain the discrepancy in A_3. The results are shown in Fig. 4.8 (a); no significant change in line width could be observed.

Lastly, longitudinal field scans with fields along [001] [Fig. 4.8 (b)] and along [100] [Fig. 4.9] were taken, providing an independent check on the $\widetilde{\mathbf{A}}$ matrix obtained above: for B along [001], the field is expected to be along a principal axis, and the induced field should only have a component *along* the magnetic field and initial muon polarization. In contrast, for B along [100], the field is expected to *not* be along a principal axis (since A_1 encloses an angle $\phi_0 = 23.2(1)^\circ$ with [110]), the induced field should therefore have a component perpendicular to the applied field, resulting in a component of the resulting vector sum of applied and effective hyperfine fields that is perpendicular to the spin polarization, which causes spin precession. Consistent with these expectations, no oscillations are observed for B along [001] [Fig. 4.8 (b)], whereas clear oscillations are visible for B along [100] [Fig. 4.9 (a)]. The fitted frequencies are shown in Fig. 4.9 (b) alongside theoretical predictions based on the $\widetilde{\mathbf{A}}$ matrix obtained above, showing excellent agreement and corroborating the measured hyperfine matrix.

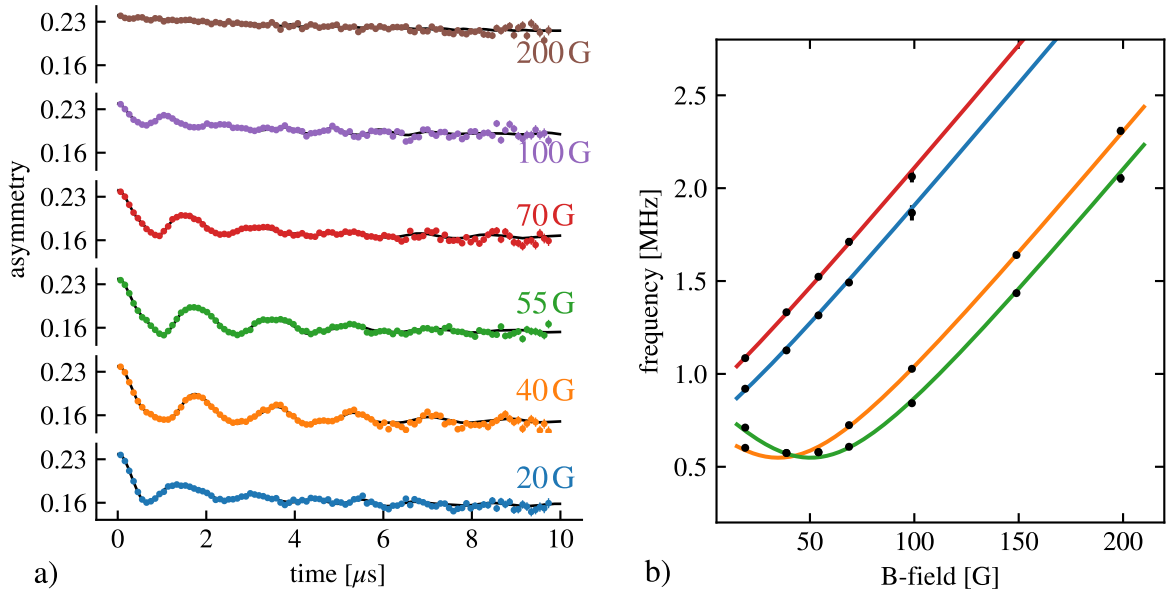

Figure 4.9: (a) Longitudinal field spectra for **B** ∥ [100]. Since the applied field is not along a principal axis of the hyperfine tensor, the induced hyperfine field has a component perpendicular to the applied field and to the initial spin polarization, causing spin precession. (b) Fitted frequencies alongside with theoretical predictions based on the hyperfine tensor obtained from the orientation dependence.

.

In summary, we find that μSR spectra obtained from a detailed orientation dependence in an applied field of 11.5 mT at 1.9 K are well described by a hyperfine tensor with $A_1 = 1.81(1)$ MHz and $A_2 = -1.37(1)$ MHz, $A_3 < 0.1$ MHz, with A_1 enclosing an angle $\phi_0 = 23.2(1)^\circ$ with the [110] direction and A_3 along the c-axis. Characteristic LF oscillations in the effective magnetic field of the unpaired electron were observed and corroborated the obtained $\widetilde{\mathbf{A}}$ matrix.

4.6 Discussion

The orientation of the hyperfine tensor as well as A_1 and A_2 are within 10% of the (scaled) ENDOR results, whereas A_3 is close to zero, which is consistent with previous μSR studies and in contrast with the ENDOR value ($A_3 = -1.076(3)$ MHz, scaled). Our results are fully consistent with the satellite frequencies observed in 20 mT along [110] by Vilão *et al.* [47]: the experiment (2.12(2), 2.30(2), 3.20(2), 3.43(2), all in MHz) agrees well with the calculated values from our $\widetilde{\mathbf{A}}$ (2.14(1), 2.34(1), 3.21(1), 3.41(1), all in MHz). However, our $\widetilde{\mathbf{A}}$ matrix at 1.9 K is clearly different from that obtained at 5 K ($A_1 = -A_2 = 1.29$ MHz, $A_3 = 0.17$ MHz) by Shimomura *et al.* [48]. This difference is attributed to dynamic processes at 5 K and discussed in more detail below.

In the following, we explore some aspects of polaronic charge-neutral centers with the help of a simple point-charge model [Eq. (4.3)] which does not take into account any spatial extent of the electron

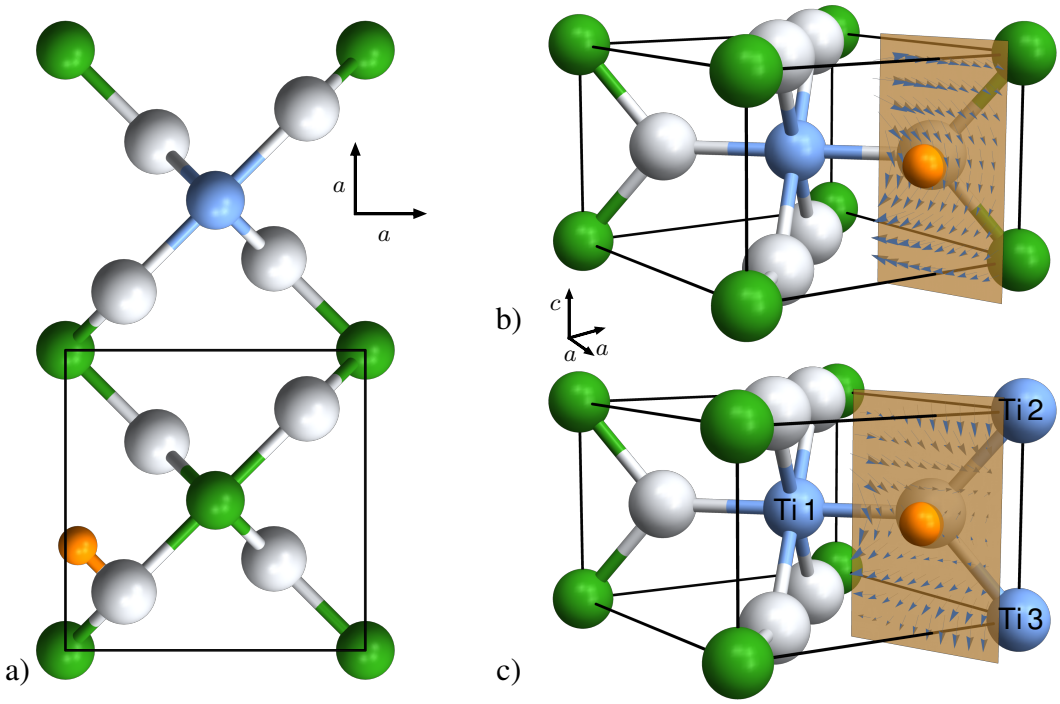

Figure 4.10: (a) Alternative muon/H - polaron complex configuration with the polaron (blue) localizing one lattice site over. This configuration is consistent with both magnitude and orientation of the $\widetilde{\mathbf{A}}$ tensor measured by ENDOR. (b) Demonstration that zero-point motion cannot cancel out the A_3 component: blue arrows represent the direction of the dipolar field for the electron spin along c; A_{33} does not change *direction* in the vicinity of the muon. Note that for visualization purposes, the magnitude of the dipolar field drops off with $\frac{1}{r}$ instead of $\frac{1}{r^3}$ in this subfigure. (c) If the polaron is spread over three Ti ions, the individual contributions to A_3 can cancel out, resulting in $A_3 = 0$ (see text for details). Here, the blue arrows represent both the direction and magnitude of the dipolar field for the electron spin along c.

wave function nor distortions induced by either the muon or the polaron. However, comparison to DFT calculations [159] indicate that the magnitude of the interaction is captured sufficiently well to be useful for a general discussion. First, we re-iterate the point made in the introduction: neither the μSR nor the ENDOR results agree with the model of a polaron predominantly localized on the Ti ion adjacent to the oxygen-bound muon (or H). For a μ-Ti^{3+} distance of $\sim 2.2\,\text{Å}$, the dipolar tensor has principal values of the order of $A_1 = 46\,\text{MHz}$, $A_2 = -23\,\text{MHz}$ and $A_3 = -23\,\text{MHz}$, i.e. about a factor of 20 larger than what is observed. The same argument applies to the ENDOR results.

Brant *et al.* appear to make their site proposal based solely on the *orientation* of their measured $\widetilde{\mathbf{A}}$, with no consideration for the magnitude. We note that there is a complex configuration with the polaron localizing one lattice site over [see Fig. 4.10 (a)] that yields the correct order of magnitude *as well as* the correct orientation for the hydrogen-polaron hyperfine coupling, $A_1 = 0.86\,\text{MHz}$, $A_2 = -0.43\,\text{MHz}$

and $A_3 = -0.43\,\mathrm{MHz}$, with A_3 along the c-axis and $\phi_0 = 23.2°$ with respect to [110], fully consistent with the ENDOR results. However, we note that the proposed site is only one of many possible polaron complex configurations, and apart from its apparent agreement with the experimental results, we do not have a compelling reason why this configuration should be preferred over the other possibilities. In general, the muon-electron Coulomb attraction alone tends to favor electron localization at the nearest possible Ti ion, however the polaronic (as well as the muon-induced) lattice distortions can modify the overall energy balance such that other sites have lower energy. In addition, the kinetic energy gain of delocalization also competes with the localization so that the stable site is potentially some compromise between all contributions. Given the observed tendency of the electron to localize on one or two Ti ions in the presence of a vacancy or defect [162–164], it appears plausible that the reduction in the observed hyperfine coupling is caused by the polaron localizing further away from the muon (H) rather than by a strong electron delocalization with the electron spread over many lattice sites, as suggested in e.g. Ref. [48].

This proposal, however, does not explain why A_3 is close to zero for the muon center. We note that zero-point motion (ZPM), as suggested in Ref. [47], cannot account for the vanishing A_3 principal component. In order to explore this aspect, we go back to the model where the polaron is predominantly localized on the nearby Ti ion. As shown in Fig. 4.10 (b), the A_{33} component does not change sign nor varies significantly in magnitude in the vicinity of the muon; thus $A_3 = 0$ cannot be plausibly caused by ZPM-induced averaging. The same argument applies to muon hopping along the c-axis, unless hopping over several lattice constants is considered. It is also not possible that an isotropic (Fermi contact) contribution of opposite sign cancels out A_3, since the overall isotropic part [Eq. (4.10)] of $\widetilde{\mathbf{A}}$ is $\frac{1}{3}(1.81 - 1.37)\mathrm{MHz} = 0.15\,\mathrm{MHz}$, which is too small to cancel $A_3 \approx 1.1\,\mathrm{MHz}$ as expected from the ENDOR results. Furthermore, we can exclude the possibility that the difference in the applied magnetic field ($\leq 32.5\,\mathrm{mT}$ for μSR, 350 mT for ENDOR) causes any change to the hyperfine coupling that could explain the difference in A_3 [Fig. 4.8 (b)]. Therefore, under the assumption that the observed charge-neutral center originates from a bound state with a single electron in an otherwise defect-free lattice, an electron localizing on a single Ti ion cannot explain the data; instead it must be distributed (at least on average) over several Ti sites such that (1) the individual contributions to A_3 cancel out and (2) the A_3 principal axis is along the c-axis. An example configuration for which $A_3 = 0$ is shown in Fig. 4.10 (c) [based loosely on Fig. 1 (a) in Ref. [157]]. We emphasize that the depicted arrangement is not an actual proposal for the observed center since the predicted hyperfine coupling is too large in magnitude ($A_1 \sim 11\,\mathrm{MHz}$, $A_2 \sim -11\,\mathrm{MHz}$ and $A_3 \sim 0\,\mathrm{MHz}$, for 28% of the electron density on Ti 1 and the remainder equally split over Ti 2 and Ti 3), and the real situation is likely more complicated with the electron spread out over further Ti ions, likely above and below Ti 2 and Ti 3. However, Fig. 4.10 (c) demonstrates that (1) in principle, a distribution of the electron over several neighbouring Ti sites can result in $A_3 = 0 \parallel c$, and that (2) any charge that is not within the $a-a$ plane of the muon has to be symmetrically arranged with respect to that plane (i.e. $\pm\theta$) such that A_{31} and A_{32} cancel out [see Eq. (4.3)], thus ensuring that the A_3 principal axis is along the c-axis.

The incompatibility of the model of an electron predominantly localized on a Ti ion adjacent to the muon (H) with both the μSR (ENDOR) data appears at odds with DFT predictions: the consensus among otherwise sometimes contradictory studies is that in the presence of interstitial H, the polaron predominately localizes on an adjacent Ti [129, 154–159]. There appear two possible explanations. (1) Either all DFT calculations determine an incorrect ground-state configuration for the charge-neutral muon (H) center, a possibility that should at least be considered since polaronic ground states are notoriously challenging to accurately predict [128, 165–167]. (2) Alternatively, *both* μSR *and* ENDOR do not observe a charge-neutral complex comprised of an interstitial muon (H) and a single electron in an otherwise pristine TiO_2 lattice, but instead a more complicated configuration, for example involving an oxygen vacancy. We note the possibility that implanted muons self-trap in an excited metastable state and do not reach equilibrium before they decay and contribute to the μSR signal [168, 169]. However, ENDOR most likely observes the H center in its lowest-energy configuration since the H is incorporated into the sample well before the measurement. Since both μSR and ENDOR observe a similar hyperfine coupling of the *same* low magnitude contrary to the DFT predictions, we conclude that even if the muon was self-trapped in a non-equilibrium state, this cannot explain the discrepancy in magnitude.

The origin of the additional, broad component at the Larmor frequency observed in the orientation dependence is currently not understood. Despite careful analysis we cannot fully exclude the possibility that it is an artifact introduced by erroneous assumptions for the model used to fit the complicated μSR spectra. The damping rate appears to be orientation dependent and vanishes along the *c*-axis, suggesting an electronic origin. Possible explanations include (1) the presence of a highly delocalized state coexisting with polaronic Mu, analogous to the proposed dual behavior of unbound excess electrons [160]. (2) A fraction of polarons may not be able to fully reach the muon to form the bound state, but stop further away, causing line broadening. (3) More speculatively, the μSR spectrum may originate from a negatively charged center comprised of the muon and *two* exchange-coupled excess electrons localized as polarons on nearby Ti ions. If the triplet state (S=1) is the ground state, $m_S = \pm 1$ could account for the satellite lines, mimicking a single bound electron, whereas the hyperfine coupling for $m_S = 0$ cancels out, resulting in a component at Larmor frequency. A variation of this model includes a neutral oxygen vacancy, which has two bound polarons in the triplet ground state [164]. The muon (H) may be trapped in the oxygen vacancy [158], resulting in a similar scenario.

Lastly, we discuss the discrepancies in the $\widetilde{\mathbf{A}}$ matrices measured with the two techniques and at different temperatures. The hyperfine coupling obtained at 5 K with μSR (Shimomura *et al.*, Ref. [48]) is clearly different from both the ENDOR results (measured at 5 K) [46] and the μSR data taken at 1.9 K (Ref. [47] and present study). We attribute these discrepancies at least partially to dynamic processes: detailed μSR measurements in 20 mT $\parallel$ [110] between 1.2 K and 10 K (Vilão *et al.*, Ref. [47]) clearly show that the μSR signal is highly temperature-dependent: the four Mu satellite lines observed below 3 K merge into two lines at higher temperatures [Fig. 3 in Ref. [47]], which is consistent with the observation of $A_1 = -A_2$ at 5 K [48]. The evolution with temperature is attributed to thermally activated muon hopping between nearby sites [47]. Importantly, at 1.9 K, i.e. the temperature of the

present study, the μSR spectra are mostly unaffected by such dynamic processes. Likewise, for ENDOR experiments, thermally activated hydrogen hopping is not expected to play a role even at 5 K due to the hydrogen's larger mass and lower zero-point motion. This absence of muon / H dynamics may explain the aforementioned similarities in the hyperfine tensor for μSR (at 1.9 K) and ENDOR (at 5 K), however the disagreement in the A_3 value (and only in A_3!) between the two techniques remains unresolved. One possible explanation for this discrepancy is that at low temperatures, the lattice does not fully relax on a µs timescale following the muon implantation, and that the two techniques observe slightly different polaron configurations as a consequence. Alternatively, the ENDOR spectra at 5 K may be affected by *polaron* dynamics, i.e. thermally activated transitions between polaron configurations that are very close in energy. Infrared (IR) absorption spectroscopy data on the charge-neutral (heavy H isotope) deuterium center were interpreted in this context by Bekisli *et al.* [146], and an excited state only 0.5 meV above the ground state was obtained, allowing for thermal accessibility even at 5 K. *If* the difference in A_3 is due to thermally activated polaron hopping between different low-lying configurations, it should be possible to freeze out those dynamics. Therefore, an ENDOR measurement of A_3 at 1.9 K or lower temperatures could help answer the question whether ENDOR and μSR observe the same ground state.

4.7 Conclusion

In summary, the precise nature of the muon-polaron complex in TiO_2, as well as the reason for the discrepancy between μSR and ENDOR, remain unresolved. However, we clearly show that the hyperfine coupling of the charge-neutral muon (H) center is significantly more complicated than suggested by the simple picture of the bound electron predominantly localizing on the Ti ion adjacent to the oxygen-bound muon (H). Several alternative models were discussed, however the data presently available does not allow for a conclusive determination of the electronic structure. A joint μSR and ENDOR investigation over the same temperatures and on the same set of well-characterized samples, ideally including pristine, de-oxygenated, and *n*-type doped crystals, could help resolve the questions that originally motivated the present study as well as elucidate the origin of the broad Larmor component observed in transverse field geometry.

This chapter also illustrated the hallmarks of a paramagnetic Mu center, in particular in the decoupled regime. Since the bound electron is unpolarized and its spin is decoupled from all other electrons, the electron spin vector aligns either along or opposite to the direction of the magnetic field if the electron Zeeman term is much larger than the muon-electron hyperfine interaction. In this limit, each Mu center gives rise to a characteristic pair of Mu satellite lines, with the splitting determined by the *relative* orientation of the principal directions of the hyperfine tensor and the applied field.

In the next chapter, we discuss a charge-neutral center where the simple picture of a muon-polaron complex *does* hold - however, contrary to the common assumption that charge-neutral centers cannot be observed in magnetic materials, we present strong evidence for their existence in the antiferromagnet Cr_2O_3.

Chapter 5

Charge-neutral muon-polaron complexes in Cr_2O_3

5.1 Introduction

The isomorphic transition metal oxides Cr_2O_3 [170, 171] and Fe_2O_3 [44, 172] were the first antiferromagnetic materials to exhibit observable zero-field muon precession signals, thus enabling the first detailed μSR investigation of the magnetic properties of antiferromagnets. An explicit motivation of these early studies was the question whether paramagnetic Mu forms in magnetic insulators just like it does in its non-magnetic counterparts. However no evidence for paramagnetic Mu was found, and in subsequent years, the study of such charge-neutral states was limited to non-magnetic materials. Paramagnetic Mu was widely assumed to be subject to strong depolarization in the presence of magnetic moments [41], and, with the exception of MnF_2 [45], no conclusive evidence for a charge-neutral muon state had been confirmed in magnetic materials.

In this chapter, we present strong evidence for a charge-neutral muon state in the antiferromagnet Cr_2O_3. In particular, our data, in conjunction with detailed density functional theory (DFT) calculations carried out by collaborators at ETH Zurich, make a compelling case for the existence of a muon-polaron complex, where the positive muon is bound to an oxygen and an excess electron localizes on a nearby Cr ion, changing its valence from Cr^{3+} ($3d^3$) to Cr^{2+} ($3d^4$). The degeneracy of the now occupied e_g orbital is lifted via a lattice distortion, leading to a Jahn-Teller (JT) polaron [126, 173, 174] on the Cr ion. Crucially, the resulting JT-stabilized muon-polaron complex is *not paramagnetic*[1] and *distinct from Mu*, since the bound electron is strongly coupled to the $3d$ electrons of the Cr host ion. Therefore, no signatures conventionally associated with a charge-neutral state are displayed, concealing its existence. However, in spite of its inconspicuous signal, the presence of such a complex has a significant impact on the location and stability of muon stopping sites, and the local fields experienced there.

This discovery of a charge-neutral muon-polaron complex in Cr_2O_3 suggests that neutral charge

[1] paramagnetic in the sense that the electron spin is unpaired and at most weakly coupled to all other electrons in the system

states could form in other insulating magnetic materials as well, which has implications for the interpretation of a wide range of μSR data. Furthermore, analogous to Mu in semiconductors, the study of muon-polaron complexes in magnetic oxides may provide detailed information on the dopant characteristics of interstitial hydrogen, a good understanding of which is crucial for a precise control of charge carriers in such materials.

The chapter proceeds as follows. In Section 5.2, the experimental conditions and basic properties of Cr_2O_3 are summarized. Next, in Section 5.3, we report the results of a comprehensive μSR study of Cr_2O_3 under zero-field conditions and in applied magnetic fields which significantly expands on the studies from the early days of μSR [170, 171, 175, 176]. The data are presented in three parts: (1) In zero field, up to three spin precession frequencies are observed, indicating three distinct muon environments with different internal magnetic fields $\mathbf{B}_{int}$. (2) Weak external fields $\mathbf{B}_{ext}(\ll \mathbf{B}_{int})$ split the observed frequencies into multiplets, providing detailed information on the orientation of the internal fields. (3) Large applied fields ($\mathbf{B}_{ext} > \mathbf{B}_{int}$) corroborate the weak field results and reveal an additional frequency. Together, the data exhibit a rich variety of dynamic phenomena that we explain in terms of site metastability and muon dynamics (Section 5.4). Most importantly, above ~ 150 K, we observe both highly dynamic muons undergoing locally restricted hopping and muons that remain static in their site. In order to explain this surprising behavior, we turn to DFT to identify candidate muon sites for all three environments, and conclude that the coexistence of site-stable and dynamic muons can be explained with the formation of a charge-neutral Jahn-Teller-stabilized muon-polaron complex (Section 5.5). Finally, in Section 5.6, we discuss the implications of charge-neutral states in Cr_2O_3 and its relevance for other magnetic oxides.

The research presented in this chapter was published in Ref. [177].

5.2 Experimental details

The μSR experiments reported on here were carried out at the Centre for Molecular and Materials Science at TRIUMF (Vancouver, Canada), although initial spectra were taken with the GPS instrument at PSI (Villigen, Switzerland). The zero and low magnetic field measurements were taken with the LAMPF spectrometer and the high magnetic field data were acquired in the NuTime spectrometer. All data were acquired with the initial muon spin polarization $\mathbf{P}_i$ perpendicular to the beam direction ($\hat{z}$).

In a crystal lattice, the charged muon usually stops in one or more distinct sites that minimize the overall energy. At a given temperature, several crystallographically distinct sites may be populated, each of which causes a different time evolution of the spin polarization. In magnetic materials, muons may experience different internal fields at inequivalent sites, causing spin precession at different frequencies $f_i = \gamma_\mu/2\pi \cdot |\mathbf{B_i}|$, each directly proportional to the magnitude of the magnetic field experienced at that particular site. In this case, the observed signal $S(t)$ is a sum of several components $S_i(t)$. In this chapter, oscillatory signals are fit to exponentially damped cosines [Eq. (2.9)], and non-oscillatory components are parametrized by simple exponentials [Eq. (2.10)].

Several single crystal specimens sourced from SurfaceNet (Rheine, Germany) were used: a $10 \times$

$10 \times 0.5\,\mathrm{mm}^3$ single crystal (C1) with the c-axis in plane and $[11\bar{2}0]$ out of plane, and $8 \times 8 \times 0.5\,\mathrm{mm}^3$ (C2) and $5 \times 5 \times 0.5\,\mathrm{mm}^3$ (C3) single crystals with the c-axis out of plane. The ZF data were taken on C1 with the c-axis oriented along $\hat{x}$ to coincide with the initial spin direction. Small external fields were applied to C1 ($\mathbf{B}_{ext} \parallel [11\bar{2}0]$) and C2 ($\mathbf{B}_{ext} \parallel c$). High field experiments were carried out on C3 ($\mathbf{B}_{ext} \parallel c$).

The primitive unit cell of Cr_2O_3 is rhombohedral (space group $R\bar{3}c$) and contains 4 Cr atoms and 6 O atoms, see inset 1 in Fig. 5.1 (c). The Cr are arranged in two pairs along the rhombohedral 111-axis (c-axis), with the oxygens forming two triangles, rotated 60° with respect to each other, between the Cr pairs. In the absence of magnetic order, the primitive unit cell is inversion symmetric, and there is three-fold rotation symmetry with respect to the c-axis. Below the Néel temperature $T_N = 307\,\mathrm{K}$, the magnetic moments associated with the unpaired electrons on the Cr^{3+} ($3d^3$) ions align pairwise opposite to each other along the c-axis [inset 1 in Fig. 5.1 (c)], and the inversion symmetry is broken.

5.3 Results

5.3.1 Preliminary considerations

In oxides, muons are generally found to stop $\approx 1\,\text{Å}$ away from an oxygen, similar to the hydrogen in a hydroxyl OH bond [178, 179]. Assuming this holds for Cr_2O_3, we can use symmetry arguments to make some general statements about potential muon stopping sites. All six oxygens are crystallographically equivalent, thus any given muon sites close to one oxygen can be projected by either inversion or 120° rotations about c into another equivalent site. Consequently, there are at least six (or integer multiples thereof) electrostatically equivalent stopping sites within the primitive unit cell, which, when projected onto the c-plane through the inversion center, form a hexagon, see inset 2 in Fig. 5.1 (c) and Fig. 5.8.

Below the Néel temperature, the magnetic moments order, resulting an internal magnetic field $\mathbf{B}_{int}$ at the muon stopping sites. The magnetic structure breaks the inversion symmetry such that $\mathbf{B}_{int}(\mathbf{r}) = -\mathbf{B}_{int}(-\mathbf{r})$. As a consequence, the *direction* of the internal fields associated with the various electrostatically equivalent sites is different. However, as the Cr moments are parallel to the c, the *magnitude* $|\mathbf{B}_{int}|$ at each of the sites is the same. Since only the magnitude determines the precession frequency, muons that stop in any one of the equivalent sites in zero external field precess with the same frequency and contribute to the same signal $S_i(t)$. From now on, we refer to an ensemble of electrostatically equivalent sites that have the same $|\mathbf{B}_{int}|$ as a *muon environment*. Note that at a given temperature, muons may stop in *different* environments with distinct $|\mathbf{B}_{int}|$.

We start with a presentation of the zero-field (ZF) results. Then, the effects of external magnetic fields $\mathbf{B}_{ext}$ are described, first for fields small compared to the internal field ($\mathbf{B}_{ext} \ll \mathbf{B}_{int}$), then for large fields ($\mathbf{B}_{ext} > \mathbf{B}_{int}$).

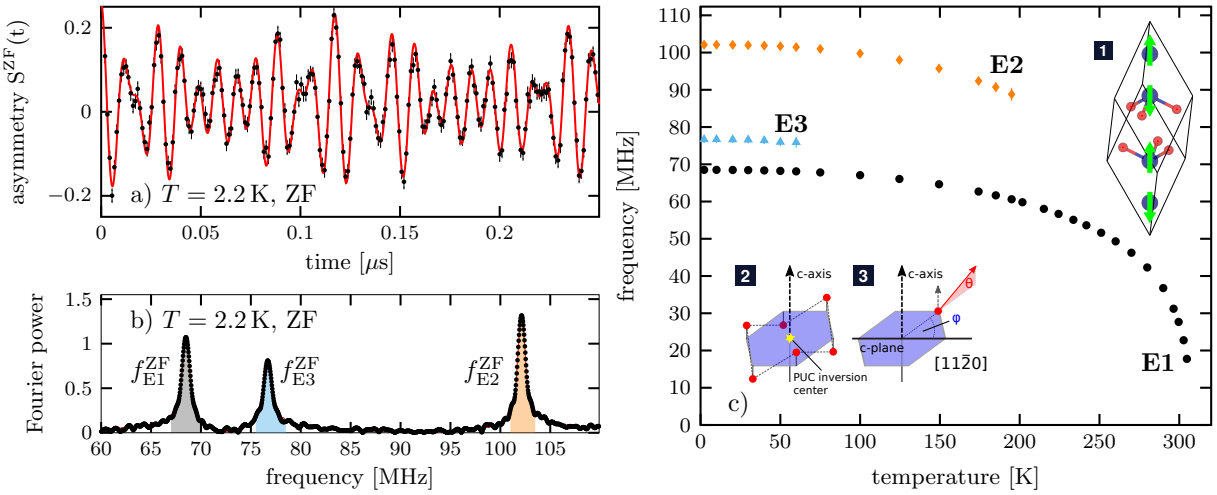

Figure 5.1: (a) ZF μSR time-domain spectrum at $T = 2.2$ K and (b) its Fourier transform. (c) Observed ZF precession frequencies assigned to three muon environments, E1-E3, as a function of temperature. Insets: (1) Primitive unit cell of Cr_2O_3 with 4 Cr atoms (blue) along the c-axis, and 6 oxygen atoms. Below $T_N = 307$ K, the Cr magnetic moments (green) align pairwise opposite along the c-axis. (2) Electrostatically equivalent stopping sites (red) form a hexagon when projected onto the c-plane through the inversion center. (3) Definition of angles describing the direction of the internal field at a given site. Adapted from Ref. [177]. CC BY 4.0

.

5.3.2 Zero external field

A ZF μSR spectrum showing the muon spin polarization as a function of time and its Fourier transform taken at $T = 2.2$ K are displayed in Figs. 5.1(a) and (b). Three ZF precession frequencies f^{ZF} are observed, indicating three distinct muon environments, termed E1-E3. With increasing temperature, certain frequencies disappear, see Fig. 5.1(c). The frequencies are assigned to the environments E1-E3 in order of appearance: the frequency observed up to T_N is called f^{ZF}_{E1}, whereas f^{ZF}_{E2} can only be seen up to ≈ 190 K and f^{ZF}_{E3} up to ≈ 60 K. All three precession frequencies increase with decreasing temperature, approximately tracking the sublattice magnetization.

The spectra contain both oscillating and non-oscillating components, and are fit with up to three damped cosines, Eq. (2.9), a non-relaxing component and a relaxing component (nonzero only above $\approx$160 K).

The fit results for the oscillatory components associated with E1-E3 are shown in Fig. 5.2. The amplitude A_{E1} is constant up to 200 K, above which it increases and approximately doubles at T_N. Both A_{E2} and A_{E3} are approximately constant. The relaxation rates λ_{E2} and λ_{E3} increase sharply when approaching the temperature where their associated ZF frequency vanishes. While both phases ϕ_{E2} and ϕ_{E3}, shown in Fig. 5.2(c), can be considered constant, there is a pronounced peak in ϕ_{E1} between 200 K and T_N. As discussed in Section 5.4.2, such a change in phase is indicative of a transition from another (so far unspecified) environment into E1, a hypothesis supported by the increase of A_{E1} at the same

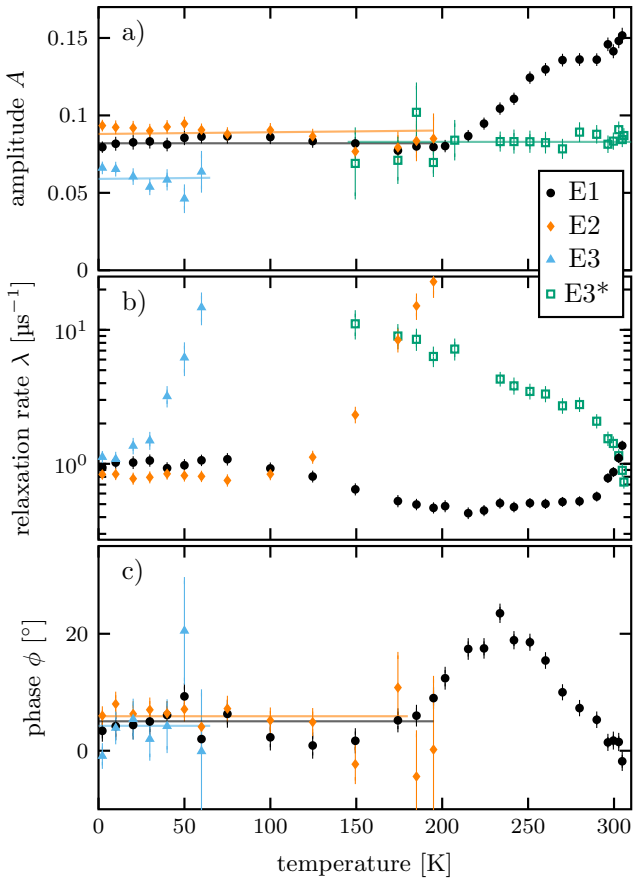

Figure 5.2: Fit results for the three ZF oscillatory signals E1-E3 as a function of temperature: (a) amplitudes A (b) relaxation rates λ (logarithmic y-axis) (c) phase ϕ. Note the pronounced peak at around 240 K in the E1 phase, indicating a transition process between muon environments. Lines are guides to the eye. Additionally, the amplitude and relaxation rate for E3* are shown, see Section 5.3.3. Adapted from Ref. [177].

temperature. Aside from the precession signals, there is a sizable non-oscillatory relaxing component that appears above ≈ 160 K (not shown). This is attributed to the E3* component discussed below in Section 5.3.3.

5.3.3 Weak external fields

There are two main effects caused by weak external magnetic fields ($\mathbf{B}_{ext} \ll \mathbf{B}_{int}$), (1) the degeneracy of $|\mathbf{B}_{int}|$ for electrostatically equivalent stopping sites within one environment is lifted, and (2) a component precessing in $\mathbf{B}_{ext}$ rather than $\mathbf{B}_{int}$ appears.

Orientation of the internal magnetic field

The internal field direction at a stopping site can be described by two angles; θ is defined as the smallest angle enclosed by $\mathbf{B}_{int}$ and the c-plane, and φ as the azimuthal angle (enclosed by $[11\bar{2}0]$ and the $\mathbf{B}_{int}$

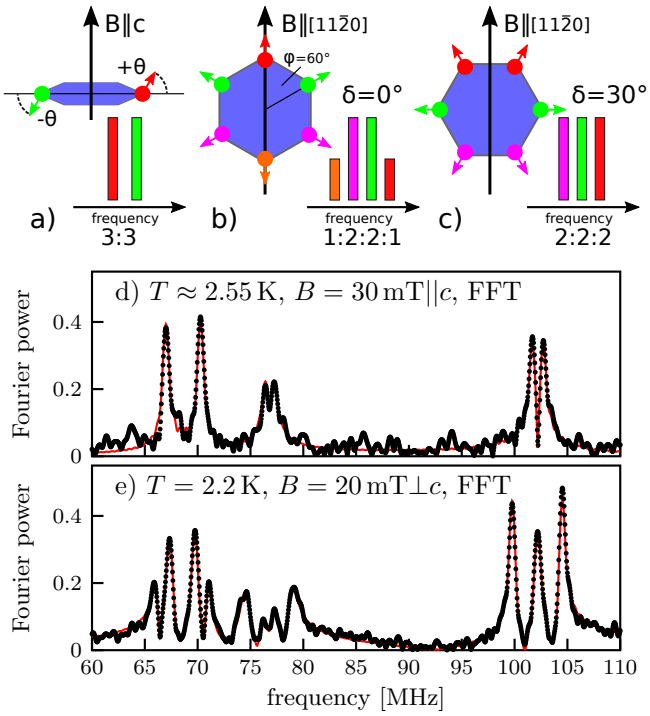

Figure 5.3: Schematic illustration of how an external magnetic field breaks the degeneracy of $|\mathbf{B}_{int}|$ for stopping sites with the same magnitude, but different directions of $\mathbf{B}_{int}$. Only those sites shown in the same color share the same magnitude of the vector sum $|\mathbf{B}_{int} + \mathbf{B}_{ext}|$, resulting in a multiplet splitting and amplitude ratio as depicted: (a) $\mathbf{B}_{ext}||c$ causes a doublet splitting, $\mathbf{B}_{ext}\perp c$ causes (b) a quadruplet ($\delta = 0$) and (c) a triplet splitting $\delta = \pm 30°$; (d) Fourier transform of μSR spectra in $B = 30\,\mathrm{mT}||c$ at $T = 2.55K$ and (e) Fourier transform of μSR spectra in $B = 20\,\mathrm{mT}||[1120]\perp c$ at $T = 2.2\,\mathrm{K}$ Adapted from Ref. [177].

.

projection onto the c-plane), see insets in Fig. 5.1. From symmetry, stopping sites forming a given environment can be projected onto the c-plane to form a hexagon. The six φ values of an environment are given by $\delta + 0°, \delta \pm 60°, \delta \pm 120°$ and $\delta + 180°$, with δ being the smallest angle enclosed by $[11\bar{2}0]$ and a hexagon corner. As noted above, the internal field magnitude at the stopping sites forming a given environment is the same, but its direction is not. While this is inconsequential in ZF, the relative orientations of $\mathbf{B}_{int}$ and $\mathbf{B}_{ext}$ matter in the presence of external fields, where the precession frequency is determined by the magnitude of the vector sum $|\mathbf{B}_{int} + \mathbf{B}_{ext}|$. Consequently, the application of $\mathbf{B}_{ext}$ lifts the degeneracy of the precession frequencies *within* an environment, causing multiplet splittings. This is schematically illustrated in Figs. 5.3 (a)-(c) both for $\mathbf{B}_{ext}||c$ and $\mathbf{B}_{ext}\perp c$. The Fourier transforms of the μSR spectra at low temperatures are shown in Fig. 5.3 for (d) $\mathbf{B}_{ext} = 30\,\mathrm{mT} \parallel c$ [2] and (e) $\mathbf{B}_{ext} = 20\,\mathrm{mT} \parallel [11\bar{2}0]\perp c$. Comparison with the ZF spectrum, Fig. 5.1(b), shows that for $\mathbf{B}_{ext} \parallel c$, the E1-E3 lines split into doublets, while for $\mathbf{B}_{ext}\perp c$, more complex multiplets are observed. The spectra were fit

[2] This measurement with $\mathbf{B}_{ext} = 30\,\mathrm{mT} \parallel c$ was taken in the Omni-Prime spectrometer rather than LAMPF. The Fourier transform is shown over the time range of $0.1 - 2\,\mu\mathrm{s}$.

Table 5.1: ZF precession frequencies f^{ZF}, θ and δ values describing the internal field orientation for E1-E3 at $T = 2.2\,\mathrm{K}$.

site	f^{ZF} [MHz]	θ [°]	δ [°]
E1	68.52 ± 0.01	24 ± 1	0 ± 3.5
E2	102.12 ± 0.01	6 ± 1	30 ± 3.5
E3	76.69 ± 0.01	5 ± 1	17.5 ± 2

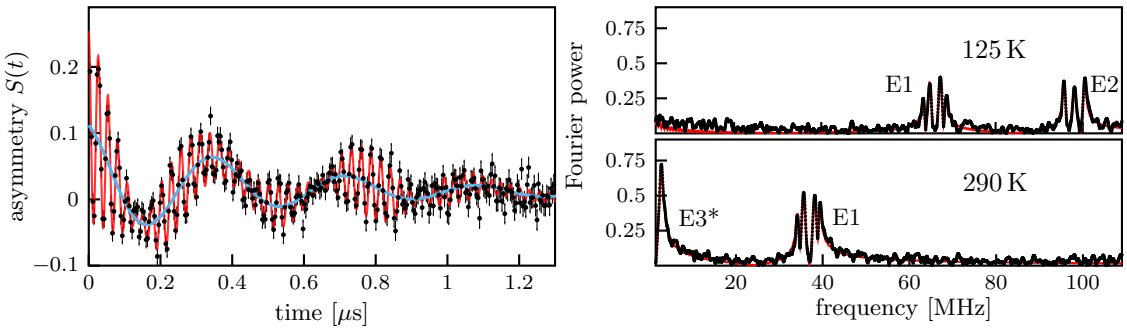

Figure 5.4: μSR spectrum taken in $\mathbf{B}_{ext} = 20\,\mathrm{mT} \perp c$ at $T = 290\,\mathrm{K}$. Besides the expected multiplet splittings, compare Fig. 5.3 (e), there is an additional component termed E3* that precesses at the (much lower) Larmor frequency of the applied field (blue line), indicating that some muons do not experience any internal field. (right): Fourier transform at $T = 125\,\mathrm{K}$ (top) and $T = 290\,\mathrm{K}$ (bottom). The E3* line corresponding to precession in B_{ext} is absent at lower temperatures. Adapted from Ref. [177].

with up to 12 oscillatory signals, Eq. (2.9), and a small non-oscillating signal. The obtained frequencies (f_{exp}) are shown in Table A.1 and A.2. Under the assumption that $\mathbf{B}_{ext}$ does not induce changes of $\mathbf{B}_{int}$, all multiplet frequencies can be consistently described by the vector sum $|\mathbf{B}_{int} + \mathbf{B}_{ext}|$, which allows extraction of the θ and δ values describing the orientation of $\mathbf{B}_{int}$ in E1-E3, see Table 5.1 for a summary and Appendix A.1 for details. The obtained angles provide stringent criteria for comparison with the internal field of candidate muon sites calculated with DFT, see Section 5.5.

Evidence for a signal component with zero internal field

Having discussed the effect of $\mathbf{B}_{ext}$ on the precession frequencies, we now turn our attention to the non-precessing component that appears in ZF above $\approx 160\,\mathrm{K}$. At coinciding temperatures and in both $\mathbf{B}_{ext} \perp c$ and $\mathbf{B}_{ext} \parallel c$ (not shown), there is a component of comparable amplitude that oscillates at the Larmor frequency of the *external* field ($f_{ext} = \gamma_\mu / 2\pi |\mathbf{B}_{ext}|$), which is absent below 150 K, see Fig. 5.4. Spin precession about $\mathbf{B}_{ext}$ rather than $\mathbf{B}_{int}$, in spite of ordered Cr moments, indicates that the muons giving rise to this signal are not subject to an internal field. The temperature dependence of the amplitude and relaxation rate of this signal, termed E3* in anticipation of its interpretation in Section 5.4.2, is shown in Fig. 5.2.

5.3.4 Large external fields

Here, we apply an external field of 4 T, which is significantly larger than the highest $\mathbf{B}_{int}$ as indicated by the ZF spectra (≈ 0.75 T), but lower than the so-called spin-flop field $\mathbf{B}_{sf}$, above which the Cr magnetic moments reorient into the c-plane ($\mathbf{B}_{sf} \approx 5.9$ T at 4.2 K and ≈ 12.5 T close to T_N [180]). The temperature dependence of the Fourier transforms of μSR spectra taken in $\mathbf{B}_{ext} = 4\,\mathrm{T}||c$ is shown in Fig. 5.5. Again, a doublet splitting is expected for each ZF frequency; however , since the position of $f^{\pm}$ with respect to f^{ZF} depends on the relative strength of $\mathbf{B}_{ext}$ to $\mathbf{B}_{int}$, and $\mathbf{B}_{ext} > \mathbf{B}_{int}$, f^{-} and f^{+} are distributed around f_{ext} rather than f^{ZF}, compare Figs. 5.3(d) with 5.5(a). At $T = 2.1$ K, five lines are observed. They can be assigned as follows: the two outer frequencies (colored in black) compose the E1 doublet $f^{\pm}_{\mathrm{E1}}$, while the second (orange) and third (blue) highest frequencies correspond to f^{+}_{E2} and f^{+}_{E3}, respectively. The remaining line (uncolored) is a superposition of both f^{-}_{E2} and f^{-}_{E3}, explaining its large amplitude. The temperature evolution follows mostly what is expected from the ZF results. With increasing temperature, the E1 doublet splitting decreases as $|\mathbf{B}_{int}|$ decreases. Above 200 K, its amplitude becomes larger, and the line broadens approaching T_N. Likewise, f^{+}_{E2} follows the decreasing $\mathbf{B}_{int}$, and disappears above $\approx$185 K. For all temperatures where f^{+}_{E2} is observed, the uncolored line has a contribution from f^{-}_{E2}. Above $\approx$170 K, a large component close to f_{ext} appears, and is, in accordance with Section 5.3.3, assigned to E3*. The E3 doublet is only observable below 50 K.

Remarkably, there is an additional component between 50 K and 170 K, termed E3′ (green in

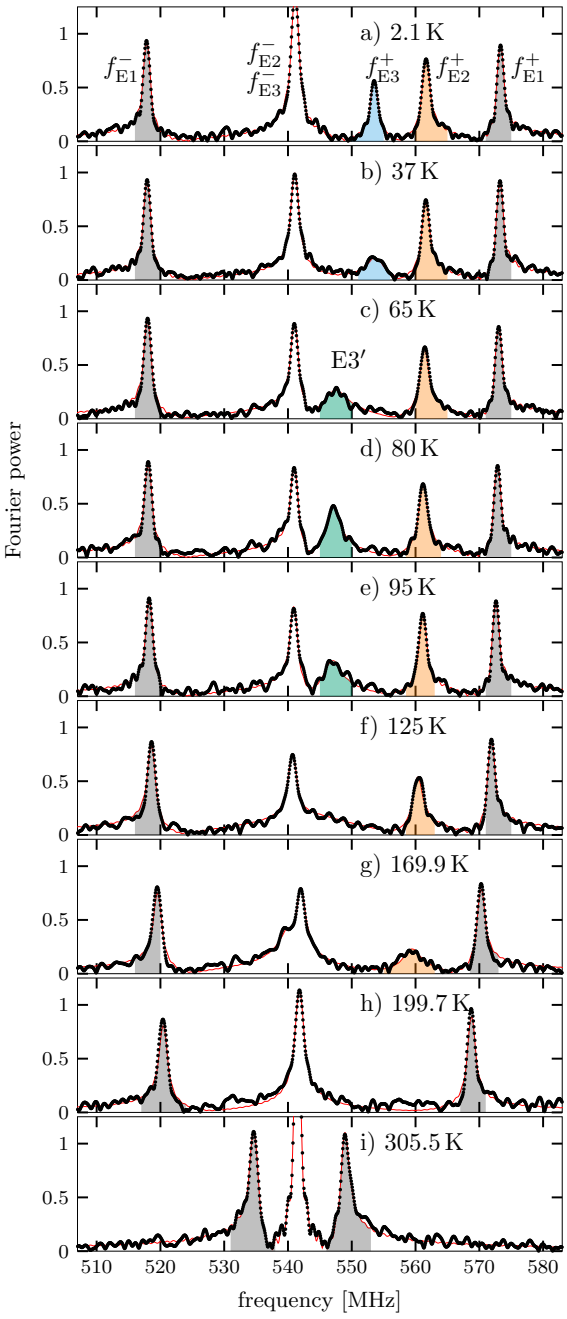

Figure 5.5: Temperature dependence of Fourier transforms of μSR spectra taken in $\mathbf{B}_{ext} = 4\,\mathrm{T}||c$. Adapted from Ref. [177].

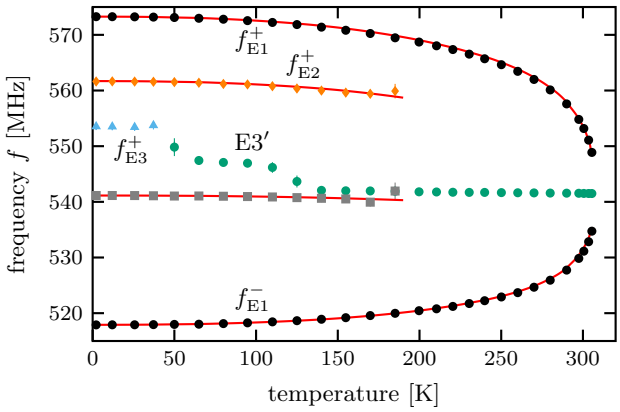

Figure 5.6: Temperature dependence of frequencies obtained in $\mathbf{B}_{ext} = 4\,\mathrm{T}||c$. Solid lines are calculated doublet frequencies $f^{\pm}_{E1}(T)$ and $f^{\pm}_{E2}(T)$ assuming constant θ. Adapted from Ref. [177].

Fig. 5.5). As will be discussed in Section 5.4.2, this additional line is strongly indicative of local hopping between adjacent E3 sites.

Details on the data analysis as well as fit results for the amplitudes can be found in Appendix A.2. From the multiplet splitting, θ values matching closely those obtained in low field are extracted, see Table A.3. This indicates that even in large $\mathbf{B}_{ext}$, $\mathbf{B}_{int}$ is not significantly affected (reasonable since the Cr Zeeman energy in 4 T is much smaller than the exchange coupling [181]), and the precession frequencies are well determined by vector addition. The fitted frequencies are shown in Fig. 5.6. The red lines represent calculated doublet frequencies $f^{\pm}_{E1}(T)$ and $f^{\pm}_{E2}(T)$ assuming constant θ, see Appendix A.2 for details. There is good overall agreement with the data, indicating that θ is largely temperature independent.

5.4 Experimental evidence for site metastability and dynamics

Three ZF frequencies are observed, see Fig. 5.1(c), and attributed to three distinct muon environments, E1-E3. Each environment contains a number of electrostatically equivalent sites with the same magnitude, but different directions, of $\mathbf{B}_{int}$. Above ≈160 K, a component E3* precessing in the *external* rather than the internal field is observed both in low and high field, indicating an environment characterized by zero internal field.

The E2 and E3 signals disappear at different temperatures, while E1 is observed over the complete temperature range, indicating that each environment has a distinct potential energy. At low temperatures, E1-E3 are all populated. Since site populations are determined by the epithermal implantation process rather than thermodynamic equilibrium, it is possible that a muon occupies metastable sites with higher energy than the ground state. If thermally activated transitions to a lower energy state are inaccessible within its short lifetime, the muon may remain in the metastable site and give rise to a distinct signal [168, 169]. However, with increasing temperature, site changes either within one, or into

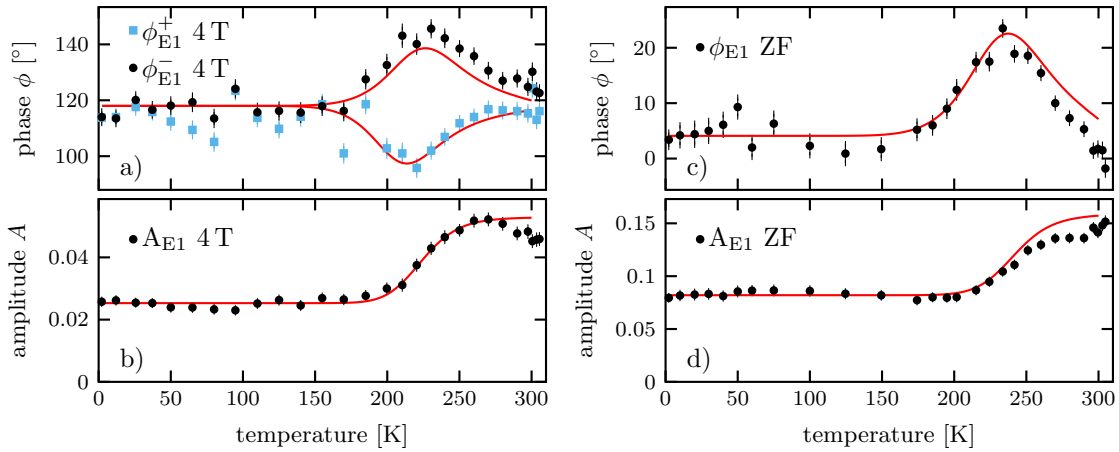

Figure 5.7: Comparison of experimental E1 phase and amplitude with the E2→E1 transition model for (a) ϕ_{E1} in 4 T, for f^+_{E1} (blue) and f^-_{E1} (black) (b) E1 amplitude, as obtained by a shared fit of the $f^\pm_{E1}$ doublet. (c) ZF ϕ_{E1} and (d) ZF amplitude. Solid lines are Eqs. (A.4) and (A.5) with shared model parameters $E_a = 180\,\text{meV}$ and $\nu_0 = 8 \times 10^{11}\,\text{Hz}$. Adapted from Ref. [177].

another environment may become possible.

Around 180 K, E1, E2 and E3* signals are observed and account for the full signal, see Fig. 5.2(a). Noting that the amplitudes of both E2 and E3* are approximately temperature independent in the respective regions where they are observed, we conclude that (1) muons in E2 do not transition into E3*, (2) thus the disappearance of E2 stems from a transition into E1 at sufficiently high temperatures and (3) consequently, by conservation of total amplitude, muons that stop in E3 below 50 K must give rise to E3* at higher temperatures.

In this section, we first present a model supporting the E2→E1 transition. Then, the evolution of muons from E3 into E3* is discussed in terms of local muon hopping between adjacent, electrostatically equivalent E3 sites.

5.4.1 E2 - E1 transition

Here, we show that the disappearance of the E2 signal around 200 K, and the subsequent increase in E1 amplitude is consistent with a metastable E2 environment that allows for transitions into E1. The following discussion is based on two assumptions: (1) The E2→E1 transition can be described by a thermally activated, exponential rate of the form $\Lambda(T) = \nu_0 \exp(-E_a/k_B T)$, where E_a and ν_0 are the activation energy and attempt frequency. (2) At the time of implantation, the probability for the muon to initially occupy a site in any of the three environments is temperature independent (i.e. at all temperatures, the same fraction of muons start out in E1, E2 and E3). This assumption is discussed in Section 5.6. While the initial fraction starting in E2 is independent of temperature, the actual time spent in this environment depends on the transition rate $\Lambda(T)$. If $\Lambda(T)$ is much smaller than f_{E2}, the E2 muons precess for many periods with f_{E2} before transitioning, and oscillatory signals from both E1 and E2 with

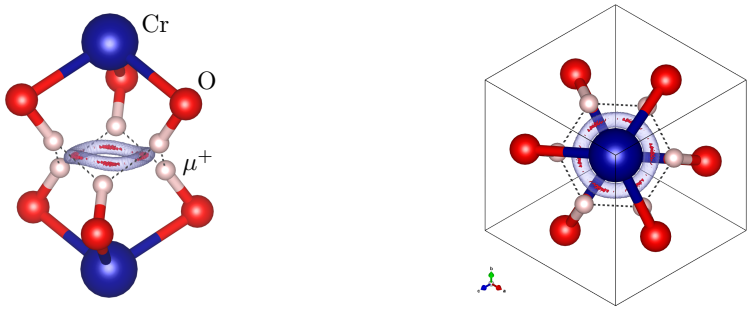

Figure 5.8: Example configuration of electrostatically equivalent muon sites, based solely on symmetry considerations and the constraint that muon stopping sites (white spheres) are located 1 Å away from oxygen (red spheres). The close proximity of nearby sites suggests localized hopping. The electrostatic potential isosurface of the *undistorted* crystal structure is shown in blue, with the red patches indicating local electrostatic minima, corresponding to the position of the so called Rodriguez (R) sites [44]. Figure made by J. K. Shenton using VESTA [182]. Adapted from Ref. [177].

amplitudes A_{E1} and A_{E2} can be detected. In contrast, if $\Lambda(T)$ is much larger than f_{E2}, the E2 muons change to E1 before the muon spin has a chance to precess with f_{E2}, and a single oscillatory signal at f_{E1} with a combined amplitude $\mathscr{A} = A_{\mathrm{E1}} + A_{\mathrm{E2}}$ can be observed. However, if $\Lambda(T)$ is comparable to f_{E2}, the E2 muons may precess at f_{E2} prior to the transition, and acquire a phase shift with respect to muons initially in E1. This results in a smaller apparent E1 amplitude $\mathscr{A}$ and an overall phase shift $\Phi(T)$. In Appendix A.3, a model accounting for such a transition and expressions for $\mathscr{A}(T)$ and $\Phi(T)$ are described. In Fig. 5.7, the E1 phase and amplitude data of both the ZF signal and the high-field doublet are compared with the transition model, with activation energy $E_a = 180\,\mathrm{meV}$ and attempt frequency $\nu_0 = 8 \times 10^{11}\,\mathrm{Hz}$ being *shared* parameters for the *complete* data set.

There is excellent qualitative agreement between the model and the data; the peak in the phase, including the opposite direction for the high field doublet, and the increase in amplitude are well described both in ZF and high field with the same parameter set. Thus the proposed E2→E1 transition with an estimated barrier $E_a = 180 \pm 40\,\mathrm{meV}$ provides a consistent explanation for the disappearance of the E2 signal, its associated increase in relaxation rate, and the subsequent increase in E1 signal amplitude.

5.4.2 Local hopping

Next, we show that both the E3 frequency observed below 50 K and the E3* signal precessing at the Larmor frequency of the external field arise from muons in the *same* environment. The appearance of E3* above $\approx 160\,\mathrm{K}$, see Figs. 5.4 and 5.5, indicates that a fraction of muons experience no internal field. This is surprising since the simultaneous observation of the E1 signal clearly shows the presence of ordered Cr magnetic moments. Although there are high-symmetry sites along the c-axis where the internal field precisely cancels, these sites are far ($\gg 1$ Å) from an oxygen and energetically unfavorable for an interstitial μ^+ site, as confirmed by DFT in Section 5.5. Instead, we consider in Fig. 5.8 an

example configuration of one environment comprised of six electrostatically equivalent muon stopping sites (white spheres), based solely on symmetry considerations (see Section 5.3.1), and a muon-oxygen distance of 1 Å. Given the close proximity of nearby electrostatically equivalent sites, thermally activated local hopping between adjacent sites seems plausible. For sufficiently fast intra-environment hopping, the effective internal field experienced by the dynamic muon is the average over all sites. Noting $\mathbf{B}_{int}(\mathbf{r}) = -\mathbf{B}_{int}(-\mathbf{r})$ and the symmetry of equivalent sites, it becomes clear that this average is *zero*. We hypothesize that muons stopping in E3 sites undergo such local hopping around a single hexagon at elevated temperatures, leading to the disappearance of the $f_{\mathrm{E3}}^{\mathrm{ZF}}$ signal, and the subsequent observation of the E3* signal in an external field.

This consistently explains the observed data: at low temperatures, muons stopping in E3 sites are quasi-static, i.e. no or only very slow hopping occurs, and each muon precesses predominately in the internal field of *one* site, giving rise to $f_{\mathrm{E3}}^{\mathrm{ZF}}$. Above $\approx 160\,\mathrm{K}$, a relaxing non-oscillatory component appears in ZF, consistent with a fraction of muons that are not subject to any field. In the intermediate temperature region $60-160\,\mathrm{K}$, no signal is observed, as the hopping is neither fast enough to efficiently average out the internal field, nor slow enough to allow for the observation of coherent E3 oscillations. External fields, both small and large, cause multiplet splittings of f_{E3} at low temperature, consistent with muons being quasi-static, while above $\approx 160\,\mathrm{K}$, a signal precessing in $\mathbf{B}_{ext}$ can be observed (E3*), since $\mathbf{B}_{int}$ is averaged to zero and does not contribute to the field magnitude. In high field, an additional signal, E3′, see Fig. 5.5, is observed in the intermediate temperature region.

In order to investigate the E3′ component, and obtain a better understanding of the dynamic behavior over the full temperature range, a Monte Carlo simulation of the muon depolarization function in $\mathbf{B}_{ext} = 4\,\mathrm{T} \parallel c$ assuming local hopping between adjacent sites was carried out. Stopping sites were arranged on a hexagon, with the in-plane component of $\mathbf{B}_{int}$ pointing radially outward, and the signs of θ alternating. An exponential correlation time $\tau = 1/\nu$, where ν is the average hop rate, was assumed. Polarization spectra were simulated in the range $\nu = 10^{-1} - 10^{5}\,\mathrm{MHz}$ for $1\,\mu\mathrm{s}$ with a time step $\Delta t = 0.0001\,\mu\mathrm{s}$ and 5000 repeats, using $f_{\mathrm{E3}} = 76.7\,\mathrm{MHz}$ for $|\mathbf{B}_{int}|$, $\theta = \pm 4.69°$, and $f_{ext} = 541.98\,\mathrm{MHz}$. Details on the general setup of the simulation can be found in Ref. [75]. The simulated spectra were fit to either a single oscillatory component, Eq. (2.9), for fast hopping, or to two oscillatory components with shared relaxation rate in the quasi-static regime. The resulting precession frequencies and relaxation rates are shown in Fig. 5.9(a) and (b).

Three temperature regions can be identified. (1) In the quasi-static low-T regime (shaded in blue), a frequency doublet $f_{\mathrm{E3}}^{\pm}$ is predicted, as expected from Section 5.3.4. For hop rates larger than the doublet beating frequency $\Delta f_{\mathrm{E3}}^{\pm} = f_{\mathrm{E3}}^{+} - f_{\mathrm{E3}}^{-}$ (dashed line), the doublet can no longer be resolved. (2) Instead, in the intermediate region (red), a single line at the average of the two doublet frequencies, $f_{\mathrm{E3}}^{avg} = (f_{\mathrm{E3}}^{+} + f_{\mathrm{E3}}^{-})/2$ is obtained. This average frequency f^{avg} is observed for hopping faster than $\Delta f_{\mathrm{E3}}^{\pm}$, however, for hop rates faster than f^{avg} (upper red line at $2 \cdot f_{\mathrm{E3}}^{avg}$), the contribution from the *internal* field starts to average out. (3) For $\nu \gg f_{\mathrm{E3}}^{avg}$, the internal field is canceled out, and a single frequency at f_{ext}, the Larmor frequency of the external field, is obtained. Between the intermediate and fast regime, the

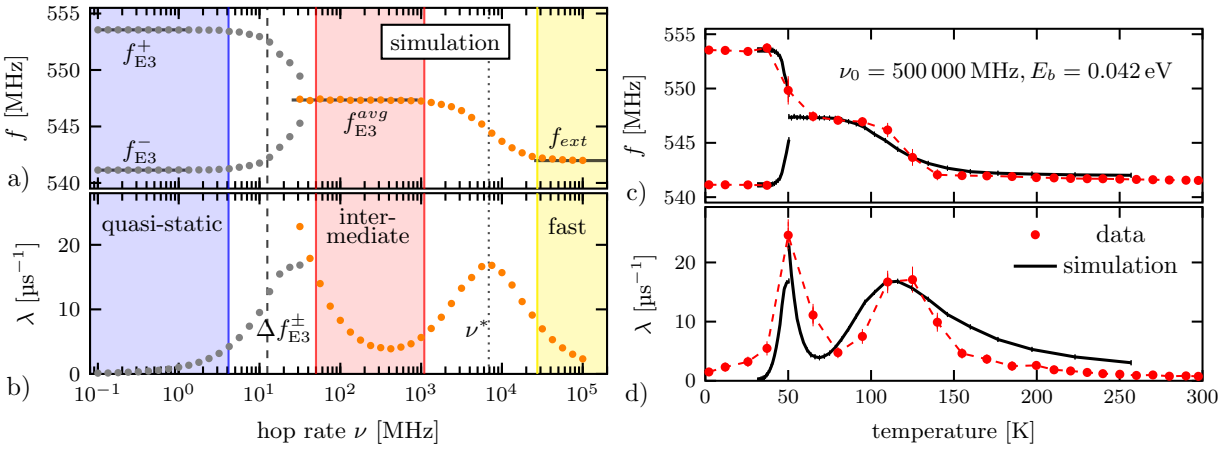

Figure 5.9: Simulation of (a) precession frequencies and (b) relaxation rate assuming hopping between adjacent muon sites arranged on a hexagon in 4 T, described by an exponential correlation time $\tau = 1/\nu$, where ν is the average hop rate. There are three different regimes: quasi-static (low hop rate), where the E3 doublet is observed, intermediate hop rates, where the average of the E3 doublet is observed, and fast hopping, where internal fields are completely averaged out and a component at f_{ext} is predicted. (c) and (d): Projection of the simulated values with an Arrhenius activation relation onto the obtained E3/E3′/E3* frequencies and relaxation rate. There is excellent qualitative agreement between the model and the data (see text for details). Adapted from Ref. [177].

relaxation rate peaks. This is attributed to a Redfield peak, with the dotted line, ν^* being within a factor of 2 of the Redfield criterion $\omega\tau \sim 1$ [82, 183].

For direct comparison, the simulation results are mapped onto the data assuming an Arrhenius-like activation $T = E_b/(k_B \ln[\nu_0/\nu])$, where E_b is an activation energy and ν_0 an attempt frequency. Fig. 5.9, displaying in red the experimental E3/E3′/E3* (c) frequencies and (d) relaxation rate obtained in 4 T, alongside the simulation results for $\nu_0 = 5 \times 10^5$ MHz and $E_b = 42$ meV, shows excellent qualitative agreement. The E3′ component is clearly identified as f^{avg}_{E3}. Note that due to the approximation of a fixed internal field, and neglect of susceptibility contributions, the model looses validity with increasing temperature. Both at the low and high temperature end of the data, the relaxation rate is not well described, indicating that a simple Arrhenius activation model is insufficient to fully describe the data.

Overall, local hopping within a *single* environment describes the E3/E3′/E3* signals in the combined data set taken in ZF, small and large $\mathbf{B}_{ext}$ very well. There is convincing evidence that E3* arises from muons undergoing thermally activated hopping between adjacent E3 sites, causing $\mathbf{B}_{int}$ to average to zero. This is strongly supported by the observation of E3′ in large $\mathbf{B}_{ext}$ and its identification as the average of the doublet frequencies f^{avg}_{E3}. Additionally, the energy barrier $E_b = 42 \pm 5$ meV between sites is estimated.

Already in the first μSR paper on antiferromagnets, local diffusion between electrostatically equivalent sites was considered a possibility in Fe_2O_3 [44]. Subsequently, local motion was speculated to occur in Cr_2O_3 [176], and is suspected [178, 184] and observed [185–187] in a range of materials. Here, we

conclusively show that local hopping indeed occurs in Cr_2O_3 by direct observation, identification and consistent description of the distinct signals that arise as a result of restricted motion in a system with broken magnetic inversion symmetry, a hop rate changing several orders of magnitude over the observed temperature range, and various applied fields.

We further note that muons in both E1 and E2 are, apart from the E2→E1 transition, site-stable, i.e. no intra-environment motion occurs. This is evident from the pronounced multiplet splitting that is observed at all temperatures where E1 and E2 signals are detected, see Figs. 5.4 and 5.5.

5.5 Identification of muon stopping sites with DFT

Thus far, using simple models describing a thermally activated E2→E1 transition and local hopping within the E3 environment, and without explicit knowledge of the stopping sites, we have explained the major features in the data. The coexistence of site-stable and highly mobile muons is intriguing, especially since there is no evidence for interexchange between dynamic E3 muons and static E1 or E2 muons, even in the presence of the E2→E1 transition. To gain deeper insight into this surprising behavior, we turn to DFT to identify muon stopping sites. With the recent increase in availability and capability of computing resources countering the large computational demands of first principles calculations, DFT has had great success in providing information about location and stability of muon stopping sites in a range of materials, and is developing into an important new tool for μSR (see Ref. [188] for a review, and Refs. [189, 190] for recent developments).

Since the inception of the μSR technique, knowledge of the location of the muon within the sample was of key importance. The main motivation for the early μSR studies on antiferromagnets, prompted by the first observation of ZF μSR signals in Fe_2O_3 [44] and its isomorph Cr_2O_3 [170], was to establish the muon as a sensitive and useful probe of the local magnetic properties of the host material by determining (1) where the muon stops and what its dynamic properties are with respect to site stability and diffusion and (2) if, and under what conditions muonium is formed in insulating (anti)ferromagnets. Based on simple electrostatic considerations, two sets of possible stopping sites were found for the Corundum structure, so called Rodriguez (R) sites [44] located in the Cr gap close to the inversion center, see Fig. 5.8, and Bates (B) sites [175] in (B0), or slightly above and below (B1) the oxygen basal plane, see Fig. 2 in Ref. [176]. The internal magnetic field in these sites was estimated by summing over the dipolar contributions from surrounding Cr moments. Additionally, covalency effects were considered, and attempts to assign ZF frequencies to specific sites yielded some partial and approximate agreements, although the overall results remained inconclusive [175, 176]. No evidence for Mu or a neutral charge state was identified.

The muon stopping sites in Cr_2O_3 were calculated by our collaborators at ETH Zurich using the Vienna ab initio Simulation Package [191–193]. We refer to the published paper [177] and its supplemental information for details. The positive muon was modeled as a hydrogen nucleus, embedded within an 80-atom $2 \times 2 \times 2$ rhombohedral supercell (SC) of Cr_2O_3. Two muon charge states were considered (1) the bare, positive muon, with a uniform charge background ensuring overall charge neutrality

CS	E	Site	d_{z^2}	f_{dip} [MHz]	f_c [MHz]	f_{tot} [MHz]	θ[°]	φ[°]	ΔE[meV]
	E3	D		94.1 ± 0.0	2.8 ± 4.4	93.9 ± 0.4	3.8 ± 2.9	4.5 ± 0.0	0
+		B0		28.2 ± 2.2	0.0 ± 0.0	28.2 ± 2.2	0.1 ± 0.0	29.5 ± 0.0	753
		C_O		99.1 ± 4.0	49.4 ± 14.0	55.9 ± 10.0	90.0 ± 0.0	1.3 ± 1.2	1565
		C_E		0.0 ± 0.0	0.0 ± 0.0	0.0 ± 0.0	90.0 ± 0.0	57.4 ± 0.0	1728
	E1	D1	↑	72.4 ± 0.3	35.6 ± 3.3	78.0 ± 1.0	-22.4 ± 2.5	35.8 ± 0.5	0
	E2	D2	↓	114.4 ± 0.2	3.9 ± 18.4	114.3 ± 1.4	0.0 ± 8.9	58.9 ± 0.7	116
		D3	↓	119.0 ± 0.8	1.6 ± 17.4	118.6 ± 6.8	-17.3 ± 7.8	5.5 ± 0.1	320
		D4	↑	100.9 ± 0.3	3.8 ± 3.2	100.4 ± 0.6	5.9 ± 2.1	58.3 ± 0.3	419
0		D5	↑	82.9 ± 0.4	34.7 ± 4.1	99.3 ± 2.2	-37.4 ± 2.5	39.7 ± 0.3	448
		B1		92.1 ± 0.2	430 ± 30	470 ± 30	-79.4 ± 0.7	24.0 ± 0.1	945
		B0		47.4 ± 1.8	0.2 ± 0.1	47.3 ± 1.8	-17.7 ± 0.8	30.3 ± 0.0	1157
		C_O		94.3 ± 1.2	581.3 ± 26.7	486.7 ± 25.5	-90.0 ± 0.0	-	355
		C_E		0.0 ± 0.0	0.0 ± 0.0	0.0 ± 0.0	90.0 ± 0.0	-	1206

Table 5.2: DFT results for various candidate sites and two charge states (CS): dipolar f_{dip} and contact contributions f_c giving rise to the combined f_{tot}, which spans the angles θ and φ as defined in 5.3.3. ΔE is the energy relative to the ground state of each charge state respectively, and d_{z^2} the spin state of the extra electron for $D1^0$-$D5^0$. Shaded rows indicate candidates for E1-E3.

and (2) a neutral muon state allowing for the extra electron.

The total hyperfine field $\mathbf{B}_{tot}$ at each site $\mathbf{r}_\mu$ has (1) a dipolar contribution $\mathbf{B}_{dip}$ mainly from the Cr $3d$ electrons, and (2) a Fermi contact term $\mathbf{B}_c$ from unpaired spin density $\rho_s(\mathbf{r}_\mu)$ at the muon stopping site. $\mathbf{B}_{dip}$ was calculated by embedding the distorted $2 \times 2 \times 2$ SC in a superstructure of undistorted SCs and summing over the dipolar contribution from the spin density grid points. Despite a fine grid spacing of 0.055 Å, the finite grid causes artifacts for points in close proximity to $\mathbf{r}_\mu$. This is mitigated by excluding grid points less than $R = 0.5$ Å away from $\mathbf{r}_\mu$. $\mathbf{B}_c$ is calculated by [189]

$$\mathbf{B}_c = \tfrac{2}{3}\mu_0\mu_B\rho_s(\mathbf{r}_\mu)\hat{c}, \tag{5.1}$$

where μ_0 is the vacuum permeability and μ_B the Bohr magneton. $\rho_s(\mathbf{r}_\mu)$ is approximated by projecting the spin density within a $R = 0.5$ Å sphere onto an s-wave state at the μ^+.

Results for both charge states (positive and neutral) are shown in Table 5.2. The structure files of all candidate stopping sites are included in the supplemental information of Ref. [177]. Calculated fields are given in units of frequency $f_i = \frac{\gamma_\mu}{2\pi}|\mathbf{B}_i|$. Note that f_{tot} is obtained by *vector* addition $|\mathbf{B}_{dip} + B_c\hat{c}|$. The energies ΔE are given with respect to the ground state and are only comparable within a given charge state. The stated uncertainties are estimated by varying the sphere radius R for both the contact and dipole term calculations in the range $0.3 - 0.7$ Å. We note that DFT local field predictions depend on the approximations of the exchange-correlation functional and the value of the effective on-site Coulomb interaction U_{eff}. By comparing various functionals with a reasonable range of U_{eff} corrections, we find variations in the predicted frequency magnitudes of ~ 15 %, in the θ angle of ~ 60% and in the ϕ angle

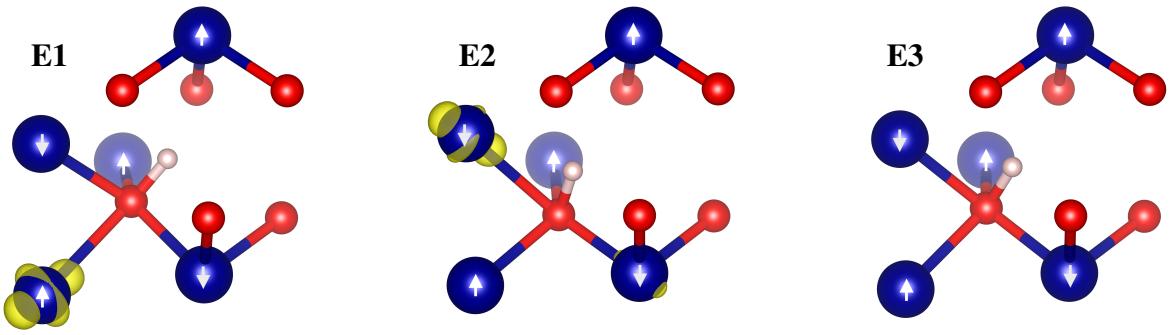

Figure 5.10: Candidate muon stopping sites for E1-E3 (white spheres) identified using DFT. Transparency indicates a location *behind* the solid atoms. Yellow isosurfaces indicate the spin density of the top-most occupied level (d_{z^2}) for the charge neutral E1 and E2 sites. Arrows indicate direction of magnetic moment. Figures made by J. K. Shenton using VESTA [182]. Adapted from Ref. [177].

of ~ 10 % with respect to the values shown in Table 5.2 (see Ref [177] for details). Furthermore, the zero-point motion of the muon is not taken into account.

For the positive charge state (superscripted +), the $B1^+$ site cannot be stabilized, and muons placed in the primitive unit-cell center (C sites) can be discounted as viable muon stopping sites based on magnitude and direction of $\mathbf{B}_{int}$, and large ΔE. For the same reasons, $B0^+$ is unlikely to represent a muon stopping site. Unless purposefully placed in a B^+ or C^+ site, muons relax into a position close to but distinct from the R-sites (the electrostatic minima of the undistorted lattice). We name this site D due to the doughnut-shaped potential energy surface formed by electrostatically equivalent sites. The difference between D and R arises predominantly from the muon-induced lattice distortion, which was not accounted for previously. The close proximity of adjacent D^+-sites makes them excellent candidates for the E3 environment. The discrepancy of 22 % between $f_{\mathrm{E3}}^{\mathrm{ZF}} = 76.7\,\mathrm{MHz}$ and the calculated value is attributed to uncertainties of the DFT calculations as discussed above.

While DFT calculations considering the positive muon can account for E3 muons undergoing local hopping, E1 and E2 are thus far unexplained, motivating a search for charge-neutral muon states. Results are shown in the bottom half of Table 5.2. $B0^0$, $B1^0$ and C_E^0 can be dismissed based on large ΔE, and C_O^0 based on the large f_{tot}. This leaves five variations of the D^0 site, labeled $D1^0$-$D5^0$. Comparison with Table A.2 and consideration of the calculated energies suggest that $D1^0$ and $D2^0$ are candidates for E1 and E2, respectively: the measured and calculated frequencies of for E1 (+14 %) and E2 (+12 %) and θ agree reasonably well and $\Delta\varphi$(E2-E1) is close to the expected 30°, compare Table 5.1. Additionally, consistent with the proposed E2→E1 transition, $D2^0$ has a larger energy than $D1^0$. The differences between $D1^0$-$D5^0$, and further aspects of the $D2^0$ →$D1^0$ transition are discussed below. Fig. 5.10 shows the positions of the E1-E3 candidate stopping sites $D1^0$, $D2^0$ and D^+.

A more detailed analysis of the charge-neutral D^0 states reveals that the extra electron localizes predominately on a nearby Cr, where it changes the valence from Cr^{3+} to Cr^{2+}, and singly occupies the initially orbitally degenerate e_g orbitals. This causes a Jahn-Teller distortion [173] by further elongating

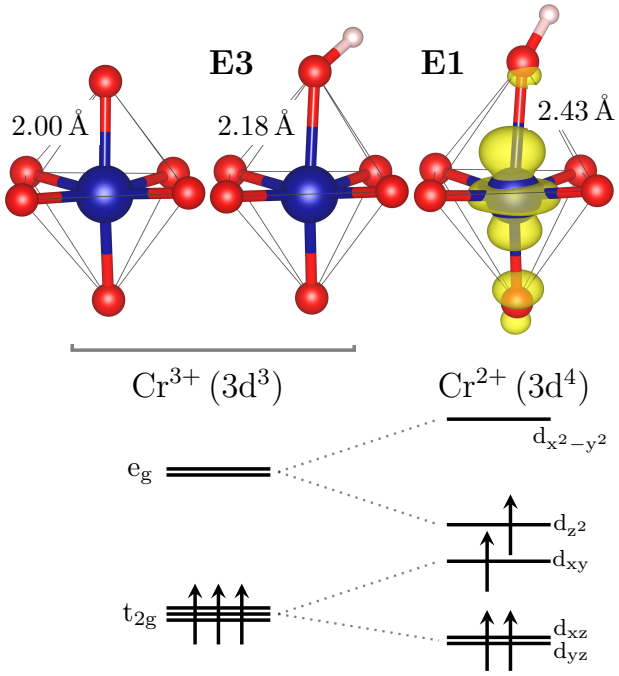

Figure 5.11: Top: Octahedrally coordinated Cr atom (1) without the muon, with (2) the positive muon and (3) a neutral charge state formed by the muon and an extra electron localized on the Cr, changing its valence state from Cr^{3+} to Cr^{2+}. The presence of the positive muon removes some electron density from its associated Cr-O bond, causing elongation from 2.00 Å to 2.18 Å. The localization of the extra electron arising from the Coulomb attraction of the muon and the energy gain from the lattice distortion further elongates the Cr-O bond to 2.43 Å and leads to the formation of a charge-neutral muon-polaron complex. Bottom: Schematic representation of the crystal field: the occupation of the degenerate e_g orbital by the extra electron leads to a Jahn-Teller distortion. The yellow isosurface shows the charge density of the top-most occupied band for the charge-neutral case, confirming that indeed the d_{z^2} level is occupied. Upper part of the figure made by J. K. Shenton using VESTA [182]. Adapted from Ref. [177].

the Cr-O bond of the oxygen the muon is bound to from 2.18 Å for the bare muon to 2.43 Å in the charge neutral case, see Fig. 5.11. The subsequent lowering of energy, see Fig. 5.11, stabilizes this charge-neutral complex of a negatively charged JT polaron [126, 174] and positive muon. This proposed mechanism is supported by the extra electron occupying the lowered e_g level d_{z^2}, see yellow isosurface representing the charge density of top-most occupied band in Fig. 5.11. We note the similarity to the paramagnetic Ti-O-Mu complex recently observed in (nonmagnetic) TiO_2 [47, 48], where an unpaired electron sits on a nearby Ti atom, and the oxygen-bound muon forms a complex with the resulting small polaron. Crucially, however, the muon-polaron complex reported on here is *not paramagnetic* and therefore *distinct from Mu*, since the bound electron is strongly coupled to the 3*d* electrons of the Cr host ion. This is discussed in detail in Section 5.6.

The $D1^0$-$D5^0$ states arise from the extra electron being localized on different Cr and small variations in the muon position. A transition between D^0 states is mainly characterized by a change in position of the extra electron rather than the muon. Note that the spin of the extra electron, being coupled to the 3*d* electrons of its Cr host, may be different for different D^0 states, as indicated in Table 5.2. We propose that the higher energy states $D3^0$-$D5^0$ are not occupied since they can easily transition into either $D1^0$ or $D2^0$ depending on their spin. However, going from $D2^0$ into the ground state $D1^0$ requires an electron spin flip assuming the muon stays stationary, i.e. an additional energy barrier has to be overcome. While the precise process for the E2→E1 transition is still under investigation, we tentatively attribute the observation of the metastable E2 environment to the existence of such a spin barrier.

In general, the energy barrier to move the joint muon-polaron complex is expected to be significantly larger than for the bare muon [127], providing a compelling explanation for the stability of E1 and E2, and the coexistence of site-stable muons and highly mobile muons in E3.

5.6 Discussion

Paramagnetic Mu centers are conventionally expected to be subject to fast relaxation in magnetic materials [41]. In the previous sections, we presented strong evidence for the formation of a charge-neutral muon-polaron complex in Cr_2O_3, that, while not exhibiting signatures conventionally expected from neutral charge states, significantly influences the muon behavior and contributes a well-resolved signal. In particular, rather than giving rise to a well-defined spectrum of typically two or four precession frequencies that are determined by a spin Hamiltonian involving the muon and electron Zeeman energies and a muon-electron hyperfine interaction [see Section 3.2], the precession signal for the muon-polaron complex in Cr_2O_3 consists of a single frequency much like the normal positive charge state, i.e. the bare μ^+ with no additional electron nearby. However, unlike charge-neutral centers in non-magnetic materials such as TiO_2 [Section 4.3], the muon-polaron complex in Cr_2O_3 is *not paramagnetic*, since its bound electron is strongly coupled to the 3*d* electrons of the Cr host ion, which themselves are antiferromagnetically coupled to the ordered network of magnetic ions of the host. This situation has similarities to the high-field limit for paramagnetic Mu, where the electron Zeeman term dominates over the muon-electron hyperfine interaction [Section 4.2]; in both cases, the z component of the electron spin is a good quantum number and its effect on the muon can be expressed as an effective field [Eq. (4.13)]. However, compared to paramagnetic Mu, where the unpolarized electron spin can either align along or opposite the applied field direction, giving rise to the characteristic paired Mu satellite lines, there are two crucial differences: (1) the spin state of the excess electron is determined by Hund's rules and depends on the spin state of its Cr host; consequently, there is only *one* frequency. (2) The spin state of the unpaired Cr electrons (and thus of the excess electron) is determined by the magnetic anisotropy of the material rather than the applied field (up to a limit); changing the direction of the applied magnetic field does not change the spin state of the excess electron. As a result, the charge-neutral complex in Cr_2O_3 does not exhibit the hallmark signatures of paramagnetic Mu, but mimics the behavior of the positive charge

state, thus "hiding" its presence.

The relevance of the discovery of a muon-polaron complex in Cr_2O_3 likely extends to other non-conductive magnetic materials, in particular transition metal oxides where, with the exception of the first (Sc) and last (Zn) element, all first row transition metals have at least two oxides where the metal ion is in a different valence state[3], showcasing a wealth of stable oxidation states. This is also the case for many higher-row TMs and lanthanides (Ln^{3+} and Ln^{2+} [194]), and extends beyond binary oxides. For example, we anticipate that in the antiferromagnetic perovskite $CaMnO_3$, where the Mn^{4+} ($3d^3$) ions are 6-fold coordinated by oxygen and have the same number of $3d$ electrons as Cr^{3+}, a muon-polaron complex analogous to Cr_2O_3 [Fig. 5.11] is formed. Intriguingly, multiple unexplained precession frequencies, consistent with such a charge-neutral state, have been reported [see Fig. 3 in Ref. [195]]. Furthermore, there is a wealth of μSR studies on transition metal oxides, including CuO [184, 196], Fe_2O_3 and $FeTiO_3$ [176], Fe_3O_4 [197], $LaMnO_3$ [198] and the orthoferrites [179], which report multiple zero-field precession frequencies that, while attributed to metastable sites, are not conclusively explained. In general, this study suggests that neutral charge states and their potential impact on the measured μSR signals should be carefully considered in all non-conductive magnetic materials; detailed DFT calculations may be required to fully explain the observed signals and separate out the intrinsic magnetic properties (i.e. without the muon). However, since the muon may occupy metastable states, the DFT formation energies alone are not sufficient to reliably predict the muon charge states in a given material, but transition barriers between charge states have to be taken into account as well. It is also worth noting that for Cr_2O_3, the charge-neutral E1 and E2 signals reflect the overall magnetic properties better than the positive-charge E3 signal, which disappears above 50 K due to local dynamics.

Regarding terminology, we propose that *any* charge-neutral muon-electron bound state can be referred to as such, i.e. a charge-neutral center or charge-neutral muon state, independent of the material it is formed in. The term muonium is reserved exclusively for *paramagnetic* centers, i.e. charge-neutral muon states in vacuum and non-magnetic compounds.

We emphasize that the present muon-polaron complex is very different from the controversial concept of a muon-induced magnetic polaron proposed by Storchak *et al* [199, 200] and disputed by others [201, 202], which invokes a localized electron bound to a muon mediating a ferromagnetic coupling between neighboring magnetic ions, resulting in a "ferromagnetic droplet" characterized by a gigantic local spin.

We speculate that muon-polaron complex formation in Cr_2O_3 occurs by a similar mechanism to Mu formation in semiconductors[4] [42]. Upon implantation, the muon slows down by creating electron-hole pairs. Towards the end of its ionization track it may capture an electron and subsequently form a charge-neutral complex. The Cr_2O_3 data are well described assuming that both the implantation and

[3]Ti: Ti_2O_3 (Ti^{3+}), TiO_2 (Ti^{4+}); V: e.g. V_2O_3 (V^{3+}), VO_2 (V^{4+}), V_2O_5 (V^{5+}); Cr: Cr_2O_3 (Cr^{3+}), CrO_2 (Cr^{4+}); Mn: e.g. MnO (Mn^{2+}), MnO_2 (Mn^{4+}); Fe: Fe_2O_3 (Fe^{3+}), Fe_3O_4 (Fe^{2+}/Fe^{3+}); Co: CoO (Co^{2+}), Co_3O_4 (Co^{2+}/Co^{3+}); Ni: NiO (Ni^{2+}), Ni_2O_3 (Ni^{3+}); Cu: Cu_2O (Cu^{1+}), CuO (Cu^{2+})

[4]Note that the precise process of Mu formation is subject of a current debate [203, 204].

electron capture processes are epithermal, and thus independent of sample temperature and thermodynamic equilibrium, which provides a plausible explanation for the previously stated hypothesis that E1-E3 are populated with the same ratio at all temperatures. Muons may stop and self-trap in metastable (charge) states with energies larger than the ground state, and only de-excite if thermally activated transitions, e.g. from E2 to E1, are accessible during the muon lifetime [168, 169].

Lastly, we propose that the observation of a charge-neutral muon state in antiferromagnetic Cr_2O_3 opens a route to use μSR to investigate the dopant behavior of interstitial hydrogen in *magnetic* oxides. A thorough understanding of hydrogen defects in such materials is crucial, since the majority of applications of magnetic oxides (including spintronics [205–209], dilute magnetic semiconductors [210], multiferroics [211] and superconductivity [212]) depend on a precise control of charge carriers. We will come back to this aspect in the next chapter.

5.7 Conclusions

In summary, we carried out a comprehensive μSR study of Cr_2O_3 under zero-field conditions and in applied magnetic fields. In zero field, we observe three spin precession frequencies, attributed to three distinct muon environments E1-E3 with different internal magnetic fields. Small applied magnetic fields along various symmetry directions split the observed frequencies into multiplets, providing detailed information on the orientation of the internal fields. The temperature dependence reveals a rich dynamic behavior that we explain in terms of a thermally activated transition between E2 and E1, and intra-E3 local muon hopping. Notably, we observe coexistence of highly dynamic E3 muons and site-stable muons in E1 and E2. Muon stopping sites and charge states for all three environments are determined using DFT, and the coexistence is explained by the formation of a charge-neutral, JT-stabilized muon-polaron complex. The identification of such a charge-neutral complex in the antiferromagnet Cr_2O_3 has implications for the interpretation of μSR data in other non-conductive magnetic materials, since the formation of muon-polaron complexes can significantly influence the stability and location of stopping sites, but its existence may be "hidden" since the behavior conventionally associated with neutral charge states is not displayed. Furthermore, this discovery opens up a route to study the dopant characteristics of interstitial hydrogen in magnetic oxides, where precise control of the carrier density may be critical for device functionalities.

Chapter 6

Local electronic structure and dynamics of muon-polaron complexes in Fe_2O_3

6.1 Introduction

α-Fe_2O_3 [213, 214] is another archetypical antiferromagnetic transition metal oxide whose magnetic properties are still actively studied [215–218]. Sharing the same crystal structure with Cr_2O_3, it is a natural candidate to test the prediction that charge-neutral muon states should form in other non-conductive transition metal compounds.

In this chapter, we report a detailed μSR study on α-Fe_2O_3. Supported by density functional theory (carried out by our collaborators at ETH Zurich), we identify several muon-polaron complex configurations that, in a key distinction to Cr_2O_3, are very close in energy and thus thermally accessible even at low temperatures. Expanding on early work [44, 170–172, 175, 176, 219–221], we are able to consistently interpret the complicated μSR spectra at low temperatures in terms of transitions between various complex configurations and local muon hopping. Our results show that muon-polaron complexes in Fe_2O_3 significantly influence the μSR signals, demonstrating that in order to relate experimental data to intrinsic magnetic properties, both muon and polaron dynamics have to be considered. Finally, the muon-polaron complex dissociates above $\sim 200\,\mathrm{K}$, strongly suggesting that analogous H centers may act as electron donors. These results may also have a more immediate and practical impact: As a semiconductor [222], Fe_2O_3 is a promising photoanode for solar water splitting [223–225] due to its natural abundance, non-toxicity and 2.1 eV bandgap that allows for efficient visible light absorption. However, photoelectric device performance is significantly hindered by the formation of small polarons: excess electrons localize on Fe ions and cause both a change in valence from Fe^{3+} to Fe^{2+} and a local lattice distortion [225–228]. As a result, conduction occurs via thermally activated polaron hopping [229–233] rather than efficient band-type transport. Efforts are being made to improve device performance by studying the impact of dopants such as Sn, Ti and Si on polaron transport [232–235], however, little consideration is given to *unintentional* dopants such as hydrogen (H). As noted previously, H is one of the

most ubiquitous impurities in semiconductors [36–38], and can significantly influence their electronic properties. By analogy between a μ^+ and a proton, the presence of polaronic muon centers strongly suggests that H impurities form analogous complexes at low temperatures. Then, the observed charge state transition, consistent with a dissociation of the muon polaron complex above $\sim 200\,\mathrm{K}$, suggests that analogous H polaron complexes are not stable at room temperature and that H impurities increase the charge carrier density (i.e. act as electron donors) while simultaneously lowering the polaron mobility since the H (μ^+) may act as a trap.

This chapter proceeds as follows. In Section 6.2, the experimental conditions of Fe_2O_3 are briefly summarized. Then, in Section 6.3, we report the results of a detailed μSR study under zero-field conditions, and consistently describe the temperature evolution of the μSR spectra in the context of transitions between various states. Next, in Section 6.4, the results of detailed DFT calculations are presented. Lastly, in 6.5, the significance for the donor behavior of hydrogen, as well as implications of charge-neutral states for the interpretation of μSR data are discussed.

The research presented in this chapter was published in Ref. [236].

6.2 Experimental details

α-Fe_2O_3 has the corundum structure (space group $R\bar{3}c$), is weakly ferromagnetic below $T_N = 948\,\mathrm{K}$, and becomes antiferromagnetic below the Morin temperature $T_M \sim 260\,\mathrm{K}$, with the magnetic moments associated with the Fe^{3+} $3d^5$ unpaired electrons aligning pairwise antiparallel along the rhombohedral 111 axis ($\hat{c}$ axis) [Fig. 6.1, inset 1] [213, 214]. Focusing on $T < T_M$, we carried out μSR experiments at $2.2 < T < 265\,\mathrm{K}$ in zero external magnetic field (ZF) in the LAMPF spectrometer at TRIUMF (Canada). Spin polarized, positively charged muons were implanted into a natural single crystal (SurfaceNet, Germany), with the initial muon polarization $\mathbf{P}_i$ aligned within 5° normal to the $\hat{c}$ axis.

6.3 Results

Due to spin precession in local magnetic fields $\mathbf{B}_i$ from ordered Fe moments surrounding various muon stopping sites, up to three coherent oscillation frequencies $f_i = \gamma_\mu/2\pi \cdot |\mathbf{B}_i|$ were observed, where $i = 1-3$ labels the signal components and $\gamma_\mu = 2\pi \cdot 135.5\,\mathrm{MHz/T}$ is the muon gyromagnetic ratio [Fig. 6.1 (a)]. f_1 (•) is detected at all T up to T_M, whereas f_2 (■) and f_3 (▲) are only observed up to 235 K and 90 K, respectively, indicating that each f_i originates from sites that are energetically inequivalent. Like Cr_3O_3 in the previous chapter, the spectra are fit to a sum of exponentially damped oscillatory signal components $S_i(t)$ [Eq. (2.9)]. Remarkably, none of the frequencies simply decrease with increasing T as they would if they followed the magnetic order parameter [237]. Instead, they display distinct step-like features. Likewise, the amplitudes and relaxation rates vary strongly with T [Fig. 6.1 (b) and (c)]. In the following, we explain the data by considering muon diffusion, site transitions and charge-neutral complexes.

First, we discuss the most stable signal, S_1 [Fig. 6.1 (•)], which we attribute to the positive charge

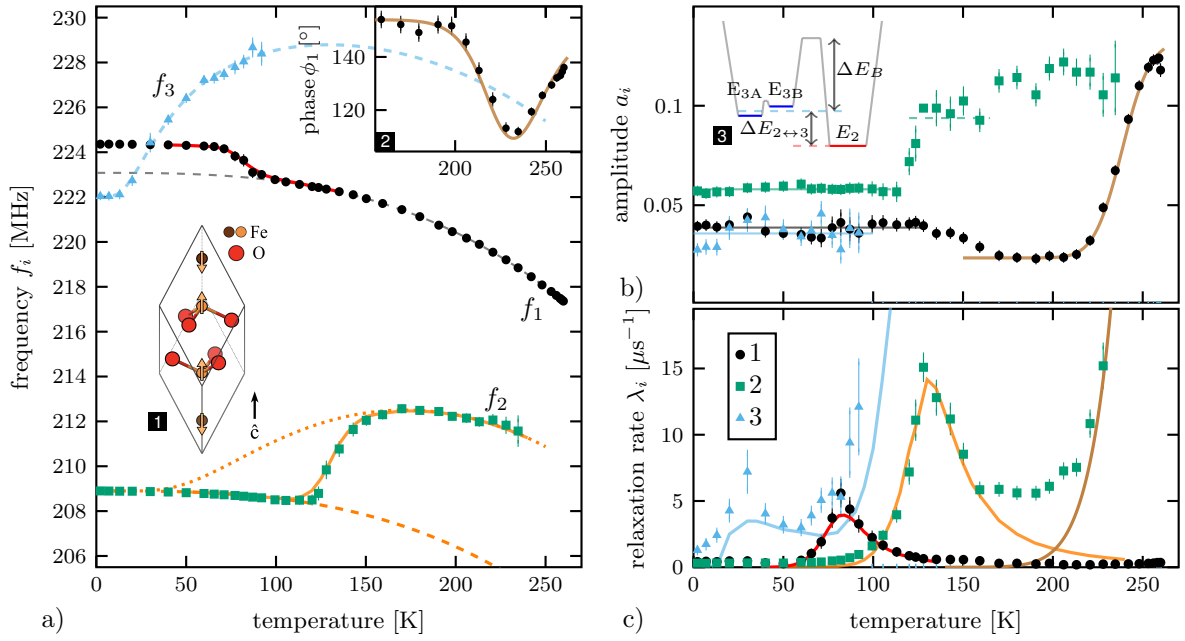

Figure 6.1: Results of fits of the ZF-μSR spectra to up to three oscillatory components $S_i(t)$ [Eq. (2.9)], with $i = 1$ (●), 2 (■), 3 (▲). Solid and dashed lines represent models as described in the main text. (a) frequencies f, (b) amplitudes a and (c) relaxation rates λ. Insets: (1) Primitive unit cell of Fe_2O_3. (2) Phase shift ϕ_1. (3) Proposed schematic energy landscape of the muon sites associated with f_2 and f_3 (not to scale). Crystal structure in inset (1) drawn by Kane Shenton. Adapted from Ref. [236]. Copyright ©2021, American Physical Society.

.

state. The discontinuity around 80 K in f_1 is explained in terms of local hopping on a ring of adjacent, electrostatically equivalent sites [Fig. 6.2 (a)]. This was also observed in isomorphic Cr_2O_3 [see Section 5.4.2] and has been proposed for Fe_2O_3 [44, 175, 220, 221]. In Cr_2O_3, the magnetic structure ($\uparrow\downarrow\uparrow\downarrow$) breaks the inversion symmetry ($\mathbf{B}(\mathbf{r}) = -\mathbf{B}(-\mathbf{r})$) such that sufficiently fast local hopping leads to a near-complete cancellation of the internal field and subsequent loss of the oscillatory signal, while in Fe_2O_3 ($\downarrow\uparrow\uparrow\downarrow$), $\mathbf{B}(\mathbf{r}) = \mathbf{B}(-\mathbf{r})$, and fast hopping only causes a cancellation of the radial in-plane component ($\perp \hat{c}$) [172], resulting in the drop in f_1 and the peak in λ_1 around 80 K. Our simulation of the muon polarization function [75, 177] based on (1) a simple parametrization $L(T)$ of the T-dependence of the order parameter[1] [Fig. 6.1 (a), gray dashed line] and (2) assuming local hopping between adjacent sites with Arrhenius-like activation (using an activation energy $E_1 = 55$ meV, prefactor $A_1 = 2 \times 10^{12}$ Hz and angle $\theta_1 = \angle(\mathbf{B}_1, \hat{c}) = 6.1°$) yields good agreement (solid red lines) with the step in f_1 and shape, position and magnitude of the peak in λ_1.

We attribute the remaining two signals, S_2 and S_3, to charge-neutral muon states, a scenario supported by DFT as outlined below. We analyze their more complex behavior with the simplifying as-

[1] $L(T) = (1-(T/T_c)^{\alpha})^{\beta}$, with $T_c = 948$ K. Fitting $f_1^L(T) = f_1^* \cdot L(T)$ to f_1 data in the range 105−250 K yields $\alpha = 2.92$, $\beta = 1.13$ and $f_1^* = 223.08$ MHz [Fig. 6.1 (a), gray dashed line].

sumptions that (1) the internal fields causing precession at f_2 and f_3 are oriented along the $\hat{c}$ axis, and (2) at a given site, the internal field follows $L(T)$. We propose that the unusual increase of f_3 with increasing T is due to a thermally excited state with frequency $f_{3\mathrm{B}}$. At 2.2 K, only the ground state with $f_{3\mathrm{A}} = 222.1\,\mathrm{MHz}$ is occupied; however, with rising T, the excited state becomes populated, with the mean occupation probability described by the energy difference $\Delta E_3 = E_{3\mathrm{B}} - E_{3\mathrm{A}}$ and a Boltzmann factor $P_{E3}(T) = \mathrm{e}^{(-\Delta E_3/k_B T)}/[1+\mathrm{e}^{(-\Delta E_3/k_B T)}]$ [47], leading to a mean frequency $f_3(T) = [(1-P_{E3}(T))f_{3\mathrm{A}} + P_{E3}(T)f_{3\mathrm{B}}]\cdot L(T)$. For $f_{3\mathrm{B}} = 241.7 \pm 1.0\,\mathrm{MHz}$ and $\Delta E_3 = 5.4 \pm 1.0\,\mathrm{meV}$, this expression yields good agreement with the data [Fig. 6.1 (a), dashed blue line], and allows for a prediction of the expected T-dependence beyond the temperatures where it is observed. The peak in λ_3 around 30 K is consistent with the proposed $f_{3\mathrm{A}} \leftrightarrow f_{3\mathrm{B}}$ transitions and indicates the presence of a small energy barrier $\sim 5\,\mathrm{meV}$.

Next, we address the disappearance of f_3 above 100 K, the upturn in f_2 above 120 K, and the increase in a_2. We propose that approaching 100 K from below, muons initially in f_3 are able to overcome a barrier ΔE_B and start to transition into the lower-energy f_2 state, causing f_3 to vanish. With further increasing T, the *reverse* transition from f_2 to f_3 also becomes accessible on the scale of τ_μ, resulting in a dynamic joint state of f_2 and f_3 [blue and orange dashed lines] with combined amplitude, increased relaxation and increasing (occupation-averaged) frequency [Fig. 6.1 (b), inset 3]. Finally, above $\sim 160\,\mathrm{K}$, the transition rate in both directions is sufficiently fast that a Boltzmann distribution is established, since ΔE_B, which suppresses transitions at lower T, is no longer relevant. We model the data in two steps. First, the data above 170 K is fit to a Boltzmann weighted frequency $\bar{f_{23}}(T) = [(1-P_{E23}(T))f_2 + P_{E23}(T)f_3(T)]$ [dotted orange line], from which $\Delta E_{2\leftrightarrow 3} = E_3 - E_2 = 16.5 \pm 2.0\,\mathrm{meV}$ is obtained. Then, ΔE_B is taken into account by simulating the muon polarization assuming a thermally activated $f_2 \leftrightarrow f_3$ transition with energy barrier $\Delta E_B = 95 \pm 25\,\mathrm{meV}$ and prefactor $A_{23} = 4.5 \times 10^{11}\,\mathrm{Hz}$, yielding excellent agreement with the frequency step and the associated peak in λ_2 [Fig. 6.1, solid orange lines].

Lastly, we address the pronounced dip in the phase ϕ_1 [Fig. 6.1 (a), inset 2], the increase in a_1, the disappearance of f_2, and the sharp increase in λ_2, all occurring around 225 K. Together, the features are clear evidence for a thermally activated transition of muons from f_2 to f_1. Assuming a transition rate of the form $\Lambda(T) = A_{2\to 1}\exp(-\Delta E_{2\to 1}/k_B T)$, the data are consistently described [Fig. 6.1, brown lines] using a simple transition model [[238], Eqs.(A.3)-(A.6)] with shared parameters $\Delta E_{2\to 1} = 0.35 \pm 0.05\,\mathrm{eV}$ and $A_{2\to 1} = 6 \times 10^{14}\,\mathrm{Hz}$.

With that, all the major features in Fig. 6.1 are explained in terms of local muon hopping, thermally accessible excited states, dynamic population of metastable states separated by a barrier, and, finally, a transition of metastable f_2 states to the apparent ground state f_1.

6.4 Identification of muon stopping sites with DFT

Now we turn to DFT to search for muon stopping sites consistent with the observed behavior. The DFT calculations were carried out by our theory collaborators at ETH Zurich using VASP [191–193, 239].

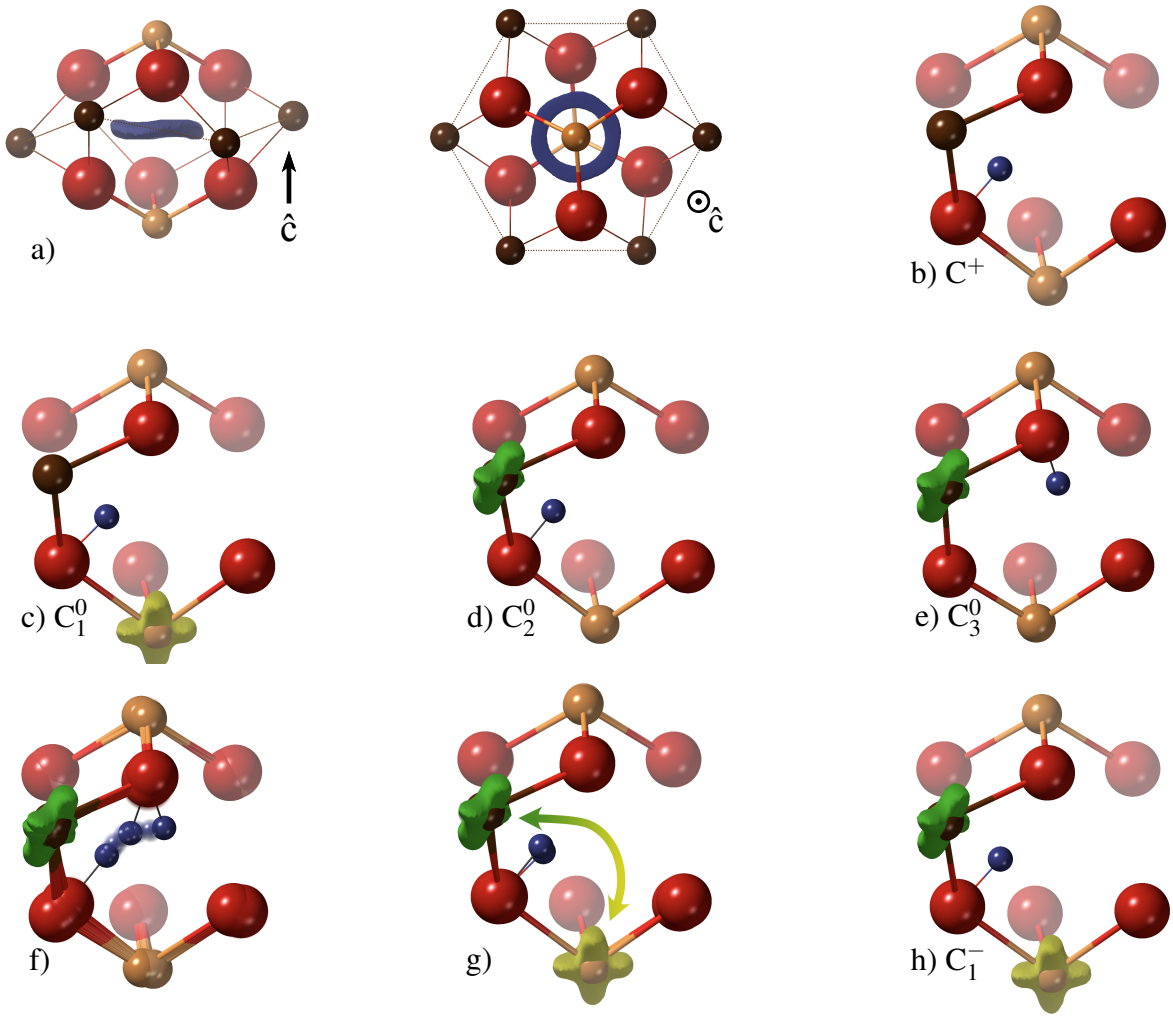

Figure 6.2: Candidate muon stopping sites identified using DFT. O (red), muon (blue), Fe (light / dark brown, shade indicating opposite spin direction). (a) visualization of a "muon cage", with the blue isosurface indicating the electrostatic minimum of the *undistorted* structure. (b) calculated site for the positive charge state C^+. (c)-(e) charge-neutral muon-polaron complexes in three different configurations. Isosurface of the spin density of topmost occupied level on the Fe ion where the polaron predominately localizes (yellow / green indicate opposite spin). Transition between (f) C_2^0 and C_3^0 and (g) C_1^0 and C_2^0. (h) Negative charge candidate site C_1^- with two polarons associated with the oxygen-bound muon. Figures made by J. K. Shenton. Adapted from Ref. [236]. Copyright ©2021, American Physical Society.

The μ^+ was modeled as a H nucleus, embedded within an 80-atom $2\times2\times2$ rhombohedral supercell. A site search procedure similar to Ref. [177] was carried out for both the positive and neutral charge states; additionally, negatively charged states were considered. We refer to the published paper [236] and its supplemental information for details and the structure files of all candidate stopping sites. For

CS	Site	f_{dft} [MHz]	$\theta[^\circ]$	ΔE[meV]	f_{exp} [MHz]
+	C^+	228.0	7.6	0	224.4 (f_1)
0	C_1^0	214.5	8.5	0	208.9 (f_2)
	C_2^0	225.9	7.3	12.5	222.0 (f_{3A})
	C_3^0	239.5	7.1	37.2	241.7 (f_{3B})
	C_4^0	259.1	6.7	50.6	
-	C_1^-	225.3	7.9	0	
	C_2^-	211.0	8.7	3.7	

Table 6.1: Candidate muon stopping sites C obtained with DFT for the positive, neutral and negative charge states (CS): calculated precession frequencies f_{dft}, angle $\theta = \angle(\mathbf{B}_i, \hat{c})$ and energy ΔE relative to the ground state of each charge state. f_{exp} lists observed frequencies next to proposed sites.

each energetically distinct candidate site (C) [2], the precession frequency f_{dft} in the combined hyperfine and dipolar fields as experienced in the distorted lattice was calculated [Table 6.1]. A single stable candidate site for the positive charge state (C^+), four possible sites for the charge-neutral state (C_1^0-C_4^0) and two configurations for the negative charge state (C_1^- & C_2^-) were obtained, all with the muon stopping ~ 1 Å away from an oxygen. Independent of the charge state, the muon localizes close to the electrostatic potential minimum of the undistorted cell [Fig. 6.2 (a), blue isosurface]. Note that despite rapid transitions between different sites, the muon does not leave the confinement of *one* such "muon cage" bounded by two 60° rotated oxygen triangles - a site change to an adjacent cage would result in a sign change of the local **B**, leading to a cancellation of internal field and subsequent signal loss, which is not observed for $T < T_M$ [3].

We associate S_1, the only signal observed up to T_M, with C^+ [Fig. 6.2 (b)], in good agreement with $f_{\text{dft}}^{C^+}$. Additionally, in analogy with Cr_2O_3 [E3 in Chapter 5], the close proximity of adjacent electrostatically equivalent sites strongly supports the T-dependence of f_1 being due to positive muons undergoing locally restricted motion within a given muon cage.

In μSR studies of magnetic materials, usually only the positive charge state is considered. However, it is clear that in Fe_2O_3, as in Cr_2O_3 [177], the single C^+ site can not explain the data and other charge states have to be taken into account. The neutral C_1^0-C_4^0 can be characterized as muon-polaron complexes: the bound electron predominantly localizes on a nearby Fe ion to form a small polaron, occupying an empty minority spin t_{2g} orbital and changing the Fe valence from Fe^{3+} ($3d^5$) to Fe^{2+} ($3d^6$) [Fig. 6.2 (c)-(e)]. The electron localization is aided by the presence of the positive muon bound to an adjacent oxygen, forming an overall charge-neutral muon-polaron complex $Fe^{2+}(O\mu)^-$ [4]. In contrast to non-magnetic materials, the spin of the bound electron is strongly coupled to the unpaired $3d$ electrons of the Fe host; as a result, the spin degree of freedom typical of paramagnetic Mu centers is lost, and only a single zero-field frequency, just like for the positive charge-state, is displayed.

[2] By symmetry, each site is part of an ensemble of six electrostatically equivalent sites per unit cell.

[3] Long range muon diffusion in Fe_2O_3 leading to signal cancellation *does* occur [172], however only above ~ 400 K.

[4] Charge-neutral relative to $Fe^{3+}O^{2-} + \mu^+$, i.e. the additional charge from the muon is compensated.

In a given muon cage, there are two distinct Fe positions belonging to different magnetic sublattices: axially above and below [Fig. 6.2 (a), light brown], or equatorially around the cage in a buckled plane [Fig. 6.2 (a), dark brown]. Each of the equatorial Fe is bound to two oxygens that make up the cage, with one bond slightly longer than the other. Focusing on the three lowest- energy C^0 sites, C_1^0-C_3^0 differ in both the position of muon and polaron: for C_1^0, the electron is predominantly localized on an axial Fe [Fig. 6.2 (c)], whereas for C_2^0 and C_3^0, the polaron is mainly on an equatorial Fe, with the muon bound either to the oxygen forming the long (C_2^0) [Fig. 6.2 (d)] or the short (C_3^0) bond [Fig. 6.2 (e)]. We propose that C_1^0-C_3^0 can explain the S_2 and S_3 signals as follows: transitions between C_2^0 and C_3^0 mainly correspond to the muon hopping between the two oxygens that are both bound to the Fe^{2+} (polaron) ion [Fig. 6.2 (f)]. Noting that the presence of the extra electron significantly distorts the lattice and decreases the distance and thus the barrier between the two sites, this provides a plausible mechanism for the low-T dynamics ($f_{3A} \leftrightarrow f_{3B}$), and renders C_2^0 and C_3^0 good candidate sites for f_{3A} and f_{3B}, jointly explaining S_3. C_1^0 is assigned to S_2, supported by its low energy and good agreement in measured and calculated frequency. Given the uncertainties inherent to DFT, there is good agreement between DFT and all observed frequencies [Table 6.1]. Considering the proposed $f_2 \leftrightarrow f_3$ transitions, this state assignment suggests that for $T >\sim 100\,\mathrm{K}$, transitions between C_1^0 and C_2^0 occur, implying that *polaron* dynamics rather than muon hopping drives this dynamic process [Fig. 6.2 (g)]. The energy barrier $\Delta E_B \approx 95 \pm 25\,\mathrm{meV}$ is attributed to both the small polaron hopping (aided by the presence of the muon for the two Fe ions involved) and a spin contribution (of the order of $\sim k_B T_N = 82\,\mathrm{meV}$ [240]), accounting for the polaron hopping between magnetic sublattices. Note that the energies of C_1^0 and C_2^0 are very close [Table 6.1], enabling the back-*and*-forth transitions postulated above, with the energy difference matching closely $\Delta E_{2\leftrightarrow 3}$.

Lastly, we discuss the negative (C^-) charge state, comprised of an oxygen-bound muon and *two* polarons, located on both axial and equatorial Fe ions [C_1^- shown in Fig. 6.2 (h)]. DFT in large (270-atom) supercells suggest that C_1^- is lower in energy than C_1^0 and a separated polaron; likewise, C_1^0 is lower in energy than C^+ and a separated polaron (see supplemental material in Ref. [236]), indicating that C^- is the lowest energy state *if* sufficient excess electrons are available. Also, $f_{\mathrm{dft}}^{C_1^-}$ is close to f_1, rendering C_1^- an alternative candidate for S_1. However, we consider the scenario where S_1 originates from C_1^- rather than C^+ unlikely, since (1) at low T, polarons are highly immobile, and while it is conceivable (and necessary to explain the data) that a thermalizing muon captures a single electron, it is implausible that all other muons capture two electrons to form C^- and no C^+ is formed at all. (2) Above 250 K, S_1 represents the complete signal, and while the Boltzmann factor favors C^-, the overwhelming degeneracy of free polaron states away from the muon is expected to dominate. Thus, we are confident in assigning S_1 to C^+.

6.5 Discussion

This assignment directly implies that the $f_2 \rightarrow f_1$ transition around 225 K corresponds to a charge-state transition from neutral to positive, which we characterize as a complex dissociation [130], i.e. a sep-

aration of the polaron and the oxygen-bound muon, rather than an ionization of the bound electron to the conduction band. Then, $\Delta E_{2\to1} \approx 0.35\,\mathrm{eV}$ corresponds to the barrier the polaron has to overcome to dissociate from the positive muon. Notably, $\Delta E_{2\to1}$ is larger than barrier estimates of $0.1 - 0.2\,\mathrm{eV}$ for "free" polaron hopping [225, 229, 233–235], indicating that the muon acts as a trap and thus lowers polaron mobility [235]. By the well established analogy between μ^+ and a proton [39–42] [see Section 4.1], these results indicate that isolated H impurities in Fe_2O_3 form corresponding $Fe^{2+}(OH)^-$ complexes. While the dynamic behavior, especially at low T, is expected to be different owing to the mass difference ($m_\mu \approx \frac{1}{9} m_p$), the electronic structure (which depends on the *reduced* electron mass) is almost identical. Likewise, the observed complex dissociation, characterized by the *polaron* hopping away, is expected to be comparable for H-polaron complexes, suggesting that at room temperature, interstitial H contributes "free" polarons and thus increases the carrier density, while simultaneously acting as a trap, decreasing overall carrier mobility. We note that the present result is particularly important since conventional spectroscopic methods such as electron spin resonance, which can be used to study hydrogen in nonmagnetic semiconductors and insulators, are not generally applicable in magnetic materials.

The results in Fe_2O_3 are in sharp contrast with Cr_2O_3, where the different complex configurations are well separated in energy [compare Tables 5.2 and 6.1], and neither unusual dynamics, nor frequencies deviating strongly from the order parameter are observed. The difference in energy separation (and consequently, dynamic behavior) is attributed to the strength of the polaron-induced Jahn-Teller (JT) distortion [173]; Cr^{2+} with $3d^4$ (high spin) is strongly JT-active, whereas Fe^{2+} with $3d^6$ (high spin) is only weakly JT-active. We note that the proposed transitions between complex configurations in Fe_2O_3 [Fig. 6.2 (g)] are conceptually very similar to polaron dynamics suggested for charge-neutral deuterium centers in TiO_2 [146].

In general, the observation of muon-polaron complexes in both Cr_2O_3 and Fe_2O_3 suggests that charge-neutral muon states and their potential impact on the μSR spectra should to be carefully considered in all non-conductive magnetic materials, in particular in transition metal oxides where multiple oxidation states for the metal ion are possible [see Section 5.6]. This has far-reaching implications for the interpretation of μSR results in a broad range of materials, and may be of particular relevance for compounds with more complicated spin and crystal structure; here, signals are usually broad and features unresolved, which makes them susceptible to misinterpretation if charge-neutral muon states are present but not identified. Likewise, studies of both slow magnetic fluctuations and heterogeneous ordering, areas where μSR is often the only available probe to investigate spin dynamics and phase coexistence, are potentially affected by the formation of muon polaron complexes; for example, polaron dynamics may be misinterpreted as intrinsic magnetic fluctuations.

6.6 Conclusion

In summary, we present a detailed μSR study of Fe_2O_3, and consistently explain the observed spectra by considering charge-neutral muon-polaron complexes, with different complex configurations providing an intuitive explanation for magnetically distinct sites that are close in energy. The unusual T-

dependences of the observed frequencies and relaxation rates are well described by transitions between these complex configurations, demonstrating that the presence of muon-polaron complexes in magnetic materials can alter the observed μSR signals such that they not only reflect the intrinsic magnetic properties, but also both muon and polaron dynamics. The identification of charge-neutral $Fe^{2+}(O\mu)^{-}$ complexes clearly shows that Cr_2O_3, the first magnetic material where muon-polaron complexes were observed [177], is not an isolated case. Analogous complexes with similarly inconspicuous signals likely exist in other insulating magnets, in particular in TMOs where the multivalent character of the TM ions facilitates polaron formation. Lastly, the presence of polaronic muon centers suggests that H impurities form analogous $Fe^{2+}(OH)^{-}$ complexes at low T, but dissociate at room temperature, indicating that interstitial H in Fe_2O_3 increases the charge carrier density while simultaneously lowering the polaron mobility.

Chapter 7

Charge-neutral muon center with large hyperfine coupling in MnF_2

7.1 Introduction

The discovery of charge-neutral muon-polaron complexes in Cr_2O_3 and Fe_2O_3, together with the previous observation by Uemura *et al.* of a high-frequency precession signal in antiferromagnetic MnF_2 that could only be explained by a charge-neutral center with a large contact interaction (comparable to that of Mu in vacuum and interstitial Mu in non-magnetic semiconductors) [45], demonstrates that muons implanted in insulating and semiconducting magnetic compounds may form charge-neutral states that are *observable* and can exist in *different* forms, analogous to Mu centers in non-magnetic materials.

In this chapter, we revisit and explore the prototypical antiferromagnet MnF_2 [241, 242], an insulating (band gap $\sim 9\,\mathrm{eV}$) transition-metal difluoride with rutile structure [243], whose spin-only (L=0) magnetic moments associated with the Mn^{2+} ($3d^5$) ions align antiferromagnetically along the tetragonal c-axis below its Néel temperature ($T_N \sim 67\,K$) [244], see inset in Fig. 7.1. The purpose of this study is to investigate the high-frequency charge-neutral center [45], and to compare it to the muon-polaron complexes discussed in the previous chapters. Since the muon is used extensively to probe its local magnetic environment, it is imperative to understand under what conditions charge-neutral states are formed in magnetic materials, what their signatures are, and how the observed μSR frequencies and damping rates can be used to infer the *intrinsic* properties of a magnetic material (i.e. without the muon present).

In addition, MnF_2 is also at the center of several current developments: the promise of both antiferromagnetic spintronic devices operating at THz frequencies and high density storage [205–209], alongside recent demonstrations of manipulation of antiferromagnetic domains [245], observation of coherent spin pumping [246] and theoretical advances towards momentum-dependent splitting of electrons into their spin components [247, 248] has led to a surge in research activity focused on antiferromagnets, and MnF_2 as a classic uniaxial antiferromagnet is featured prominently as a model system [245–250].

This chapter proceeds as follows: After a brief description of the experimental conditions in Section 7.2, the results of new detailed μSR measurements in MnF_2 that significantly expand the scope of early μSR studies [45, 251–255] are presented in Section 7.3. Two distinct zero-field oscillatory signals are observed below T_N, with frequencies at 3.8 K of 157(1) MHz and 1279.1(1) MHz, consistent with Ref. [45]. The origin of these components, as well as the remarkable observation that the two frequencies evolve differently with temperature and *neither* tracks the temperature dependence of the bulk magnetization, are discussed in Section 7.4. We demonstrate that in MnF_2, the magnetic properties measured by μSR and the charge-state of the muon are closely intertwined, and both aspects have to be considered when interpreting the data. Finally, we explore the implications of this study for other magnetic materials.

7.2 Experimental details

All μSR experiments were carried out at the Paul-Scherrer-Institute (Villigen, Switzerland). Two data sets were obtained: (1) a detailed temperature dependence in zero field with the initial spin polarization $\mathbf{P}_i$ perpendicular to the muon beam and parallel to the sample surface, acquired in the fast-timing HAL-9500 spectrometer which is capable of observing the high-frequency line, and (2) a coarse temperature dependence with the initial spin (almost) along the muon beam (i.e. perpendicular to the sample surface), acquired in the GPS spectrometer as a supporting measurement to aid with the interpretation of the HAL-9500 data. Additional measurements in applied fields (not discussed here) support the conclusion in Ref. [45, 253] that the internal field for both observed signal components is along the c-axis. We investigated a single crystal grown by collaborators at the University of Oxford (UK). Experiments were conducted under the assumption that the c-axis and thus the internal fields are perpendicular to the sample surface; however indications of a misorientation during the experiment motivated subsequent Laue measurements (by C. Mielke, PSI) that showed that the sample was instead cut along the $a-c$ diagonal. While this complicates the data analysis, we emphasize that the main results of this study, namely the detailed temperature dependence of the zero-field frequencies and the qualitative temperature behavior of the depolarization rates, are not affected.

7.3 Results

Fourier transforms of HAL-9500 μSR spectra at representative temperatures below T_N are shown in Fig. 7.1. Two distinct precession signals, labeled $S1$ and $S2$, are observable, with frequencies of 157(1) MHz and 1279.1(1) MHz at 3.8 K, consistent with Ref. [45]. The line widths of the two components exhibit opposite behavior: at low temperatures, the low-frequency $S1$ signal is very broad ($\approx 35\,\mu s^{-1}$) and $S2$ is extremely narrow ($< 1\,\mu s^{-1}$), whereas the reverse is true close to T_N. The spectra are fit to two exponentially damped oscillatory components [Eq. (2.9)] accounting for $S1$ and $S2$. The data suggests that the c-axis is almost perpendicular to the initial spin polarization $\mathbf{P}_i$, however since the exact in-plane orientation is not known, the fit includes a small non-oscillatory relaxing component [Eq. (2.10)] to

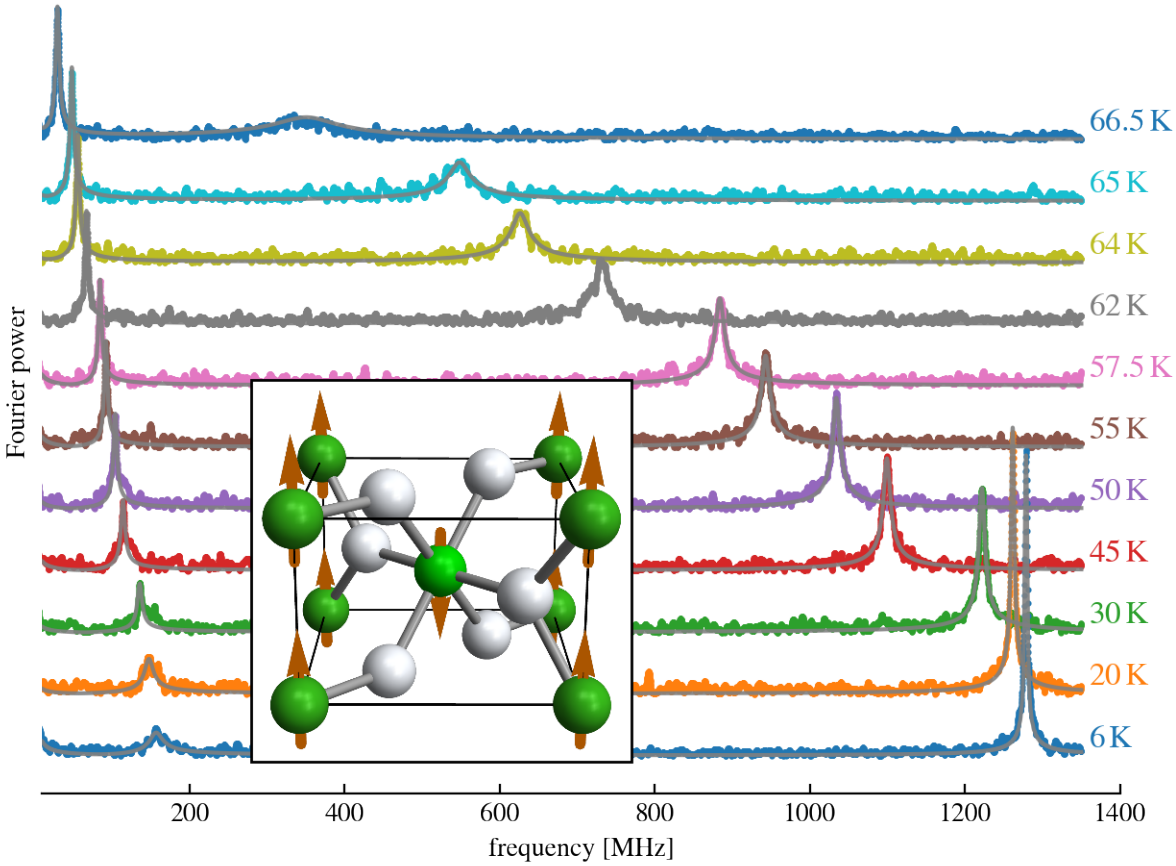

Figure 7.1: Fourier transforms of zero-field μSR spectra at representative temperatures below T_N. Inset: unit cell of MnF_2, with Mn in green, O in white and brown arrows representing the $Mn^{2+}(3d^5)$ magnetic moments.

account for a component of $\mathbf{P}_i$ along c. Additionally, there is a sizable component (amplitude $a \sim 0.077$) that is attributed to muons stopping in the silver sample plate, easily identified in the presence of external fields, where this component precesses at the Larmor frequency (above and below T_N) with little or no damping. The fit results for $S1$ and $S2$ are shown in Fig. 7.2. The data were fit in two different ways. First, the amplitudes of the oscillatory signal components were unconstrained [orange points in Fig. 7.2]. However, at somes temperature, the signals are strongly damped, resulting in a strong correlation between amplitude and damping rates. Therefore, the data were also fit with the amplitudes fixed to the values obtained in the temperature regions where the respective damping rate is lowest, and the signal (and thus the amplitude) is determined best [$4-10\,\mathrm{K}$ for $S1$ and $52-61\,\mathrm{K}$ for $S2$]; for the $S2$ signal, the time-resolution-related increase in observable amplitude with decreasing frequency was explicitly taken into account. Fixed amplitudes are justified under the assumption that the initial formation probability of various states and thus the fraction of $S1$ and $S2$ are temperature-independent, similar to the situation in Cr_2O_3 and Fe_2O_3. Results are shown as black points in Fig 7.2. Both models yield satisfactory fits;

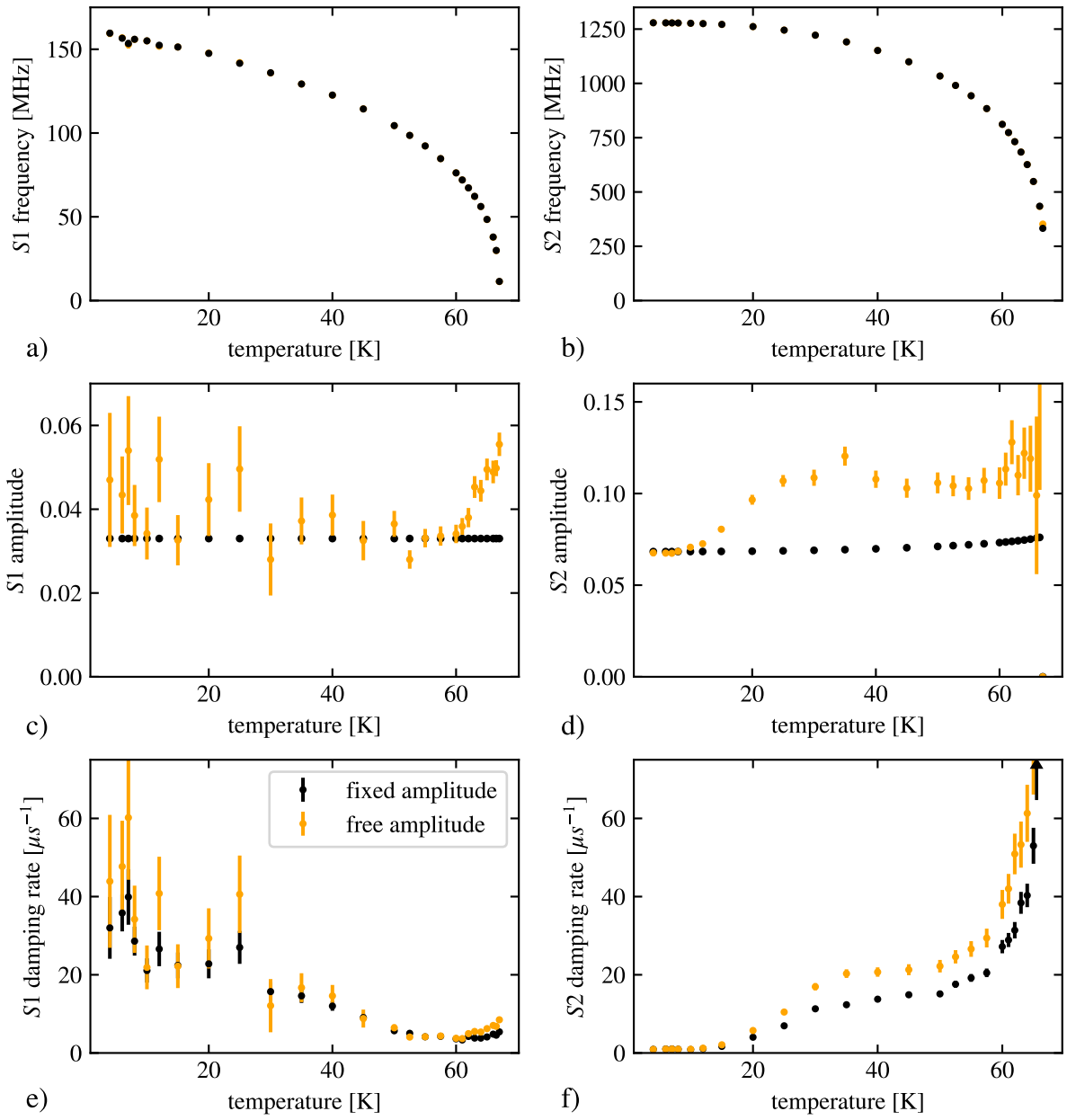

Figure 7.2: Temperature dependence of the fitted precession frequencies, amplitudes and damping rates for both signals obtained in MnF_2. The data were fit with both the amplitude unconstrained (orange points) and fixed (black points), see text for details.

crucially, the obtained frequencies are not dependent on the model (except very close to T_N); likewise, the qualitative behavior of the damping rates is the same.

As previously mentioned, the experimental results confirm that the internal fields for both $S1$ and $S2$ are along the c-axis to a good approximation. We now present the second data set, obtained in GPS with $\mathbf{P}_i$ perpendicular to the sample surface, i.e. with a large component of the initial polarization along the

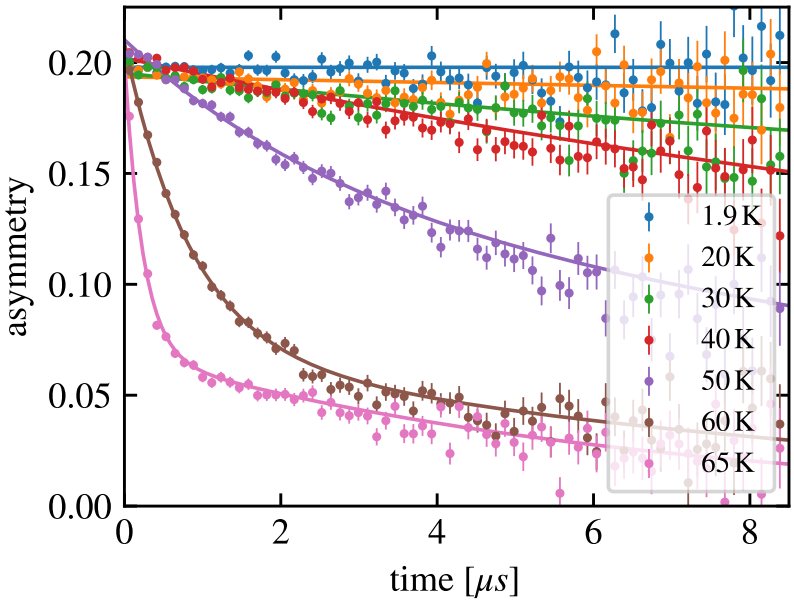

Figure 7.3: μSR spectra of the longitudinal component ($\mathbf{P}_i \parallel c$) at representative temperatures below T_N. No external magnetic field is applied, however each muon sees a substantial internal magnetic field from the ordered Mn^{2+} moments.

c-axis (which encloses an angle of 34° with the plane normal). Since $\mathbf{P}_i$ has components perpendicular and parallel to the internal field, there are both oscillatory (transverse) and non-oscillatory (longitudinal) signal contributions. However, the oscillatory contributions from $S1$ are strongly damped and from $S2$ are not observed (due to the limited timing resolution in GPS). Thus we focus exclusively on the non-oscillatory longitudinal contribution, where the signal decay is a direct measure of the spin-lattice relaxation. As evident from Fig. 7.3, there is very little spin relaxation at low temperatures ($< 0.1\,\mu s^{-1}$ for $T \leq 40\,K$). At 50 K and above, the signal can be separated into two components at an approximate 70:30 ratio, which are attributed to $S2$ and $S1$, respectively. In the context of the present study, the lack of relaxation at low temperatures is most relevant; we refer to Refs. [254, 255] for a detailed discussion of the spin-lattice relaxation over the whole temperature range.

7.4 Discussion

We now discuss the origin of the two signal components, starting with the high-frequency $S2$ signal. The $S2$ frequency is too high to be explainable by spin precession in only the dipolar field of ordered Mn moments; instead, in agreement with Ref. [45], we attribute $S2$ to a charge neutral muon state with a significant Fermi contact interaction. Supported by preliminary DFT calculations [by Kane Shenton (ETHZ), not shown], we propose that the electron is shared between the muon and a single nearby Mn^{2+} ($3d^5$) ion; in order to allow partial localization of the excess electron at the Mn, the electron spin must be opposite to the spins of the Mn host since all $3d$ orbitals are initially singly occupied.

Analogous to muon-polaron complexes in Cr_2O_3 and Fe_2O_3, the bound electron is not paramagnetic since its spin is strongly coupled to the Mn host, and for a given electron there is only *one* possible spin state; consequently, in spite of the large internal magnetic fields there is only a *single* frequency instead of the paired satellite lines that are characteristic for Mu in non-magnetic materials[1]. DFT predictions for the charge-neutral muon state in CoF_2 suggest that the dipolar contribution is about 70 MHz and *adds* to the contact contribution [256]. It is reasonable to assume that this prediction extends to MnF_2, which has the same crystal and magnetic structure; we can estimate the dipolar contribution in MnF_2 by scaling with the ratio of the magnetic moments [2.60(4) μ_B per Co ion in CoF_2 [257] compared to 5.04(6) μ_B per Mn ion in MnF_2 [258]] to be $\nu_{dip} \approx 140$ MHz. The S2 frequency can then be described as $\nu_{S2} \approx \nu_{dip} + \frac{A_{iso}}{2}$, indicating an isotropic contact contribution $A_{iso} \approx 2218$ MHz, i.e. about 50% of the vacuum value. It is interesting to note that similar isotropic couplings of the order of ~ 2 GHz were observed in highly covalent semiconductors including Si, Ge and GaAs [42]. This is consistent with the idea that the unpaired electron is shared between the muon and surrounding atoms, lowering the electron density at the muon site and thus the isotropic coupling constant. In contrast, in ionic insulators such as the alkali halides, no such sharing is expected, and isotropic couplings ~ 4.4 GHz close to the vacuum value are reported. MnF_2 clearly deviates from this trend; however, unlike for other ionic insulators, the Mn^{2+} ions in the transition metal compound MnF_2 are *not* in a closed-shell configuration, but multiple Mn valence states are possible, permitting electron-sharing with the muon and causing a dramatic reduction in the hyperfine coupling compared to many ionic insulators with filled shells such as KCl [259].

Next, we address the $S2$ linewidth [Fig. 7.2 (d)]. For a high-frequency signal, the $S2$ line is remarkably narrow ($< 1\,\mu s^{-1}$) at low temperatures, and increases for $T \geq 15$ K with increasing temperature up to ≈ 40 K, where it plateaus, only to sharply increase again on approach to T_N. The dominant process for the spin-lattice relaxation of the F^{19} nuclear spins is magnon scattering [260], and the marked decrease in linewidth at low temperatures, consistent with the MnF_2 magnon gap of ≈ 12 K [261], suggests that magnon scattering might also be a contributing factor to the linewidth. However, comparison with Fig. 7.3 clearly shows that spin-lattice relaxation only plays a minor role, and most of the damping rate of the oscillatory component is due to inhomogeneous broadening (dephasing), i.e. a distribution of effective magnetic fields [Fig. 2.2 (c)]. Minor sample inhomogeneities and defects as well as slight temperature variations can plausibly explain the linewidths. For example, the damping rate at 63 K is $38.4 \pm 2.8\,\mu s^{-1}$, which corresponds to a frequency distribution of width (FWHM) ≈ 12 MHz. Between 62 K and 64 K, the frequency changes by 105.5 MHz, i.e. ≈ 53 MHz/K, and a temperature variation of $\approx \pm 0.1$ K can cause a frequency distribution that fully accounts for the observed linewidth at 63 K. Since the rate of frequency change per temperature decreases with decreasing temperature, dephasing and thus the damping rate is lowered accordingly.

The normalized temperature dependence of the $S1$ (orange) and $S2$ (blue) frequencies, alongside the

[1] Technically, there *are* two frequencies, one for each magnetic sublattice (and thus with opposite sign), however the *magnitude* in zero external field is the same.

bulk magnetization (green) as obtained from X-ray diffraction [258] are shown in Fig. 7.4. Clearly, all three quantities evolve differently with temperature; *neither* of the two μSR frequencies tracks the (X-ray-obtained) magnetic order parameter[2]. The assignment of $S2$ to a charge-neutral center for which the excess electron is equally shared between the muon and a single Mn ion (designated Mn^{S2}) affords an intuitive explanation why the S2 frequency deviates from bulk magnetization: the S2 frequency is almost completely determined from the contact interaction with the unpaired electron, which in turn is directly proportional to the average spin $\langle S_z \rangle$ of the unpaired electrons of Mn^{S2}. However, with an extra electron, the orbital magnetic moment is no longer zero ($L \neq 0$) for Mn^{S2}, resulting in a larger magnetic anisotropy with a significant orbital contribution *for that particular Mn* ion. This provides a plausible explanation why the temperature dependence of the average spin for this "impurity ion", and consequently the $S2$ frequency, deviate from the bulk magnetization. It is interesting to compare these charge-neutral muon centers to the case of Fe^{2+} impurities in MnF_2 [262–264], since Fe^{2+} ($3d^6$) has an electronic configuration very similar to Mn^{S2} with its additional (shared) electron. Remarkably, the magnetization curve for the Fe^{2+} impurity spin [Fig. 7.4 (red diamonds), from Ref. [262]] is significantly different from the bulk magnetization, and maintains a larger average spin to higher temperatures in a similar manner as the $S2$ frequency. In addition, the proposal that the additional electron on Mn^{S2} locally modifies the magnetic anisotropy finds support in a recent investigation of the magnetic properties of hydrogen-doped Fe_2O_3, which explains significant changes to the magnetic properties with H-donated polarons changing the magnetic anisotropy of the affected Fe ions [265].

We now turn to the $S1$ signal. The most straight-forward assignment is the positive charge state, which in fluorides usually corresponds to a so-called $F\,\mu\,F$ state [266], for which the positive muon pulls two nearby F^- ions close together to form a molecule-in-a-crystal defect [256]. In non-magnetic materials, the strong dipolar interaction between muon and F nuclear spins leads to characteristic zero-field oscillations that have been used extensively to study such complexes [267]. However, in the ordered phase of a magnetic compound, the magnetic interactions dominate and the muon and F nuclear spins are decoupled, and no zero-field $F\,\mu\,F$ oscillations are expected in MnF_2 for $T < T_N$. However, linear $F\,\mu\,F$ states are found in two isomorphic fluorides, namely in (non-magnetic) ZnF_2 [267] and in the paramagnetic phase of antiferromagnetic CoF_2 [256]. In addition, de Renzi *et al.* observed paramagnetic frequency shifts in MnF_2 above T_N that are consistent with those obtained in CoF_2 [Fig. 9 in Ref. [252]], and interpreted as an indication that an analogous $F\,\mu\,F$ state forms in MnF_2. However, unlike for CoF_2, there are no published accounts of characteristic $F\,\mu\,F$ oscillations in MnF_2 in the paramagnetic phase, and our attempts to observe them at 72.5 K and 100 K were unsuccessful, possibly due to strong spin-lattice relaxation of the F nuclear spins [268, 269]. In CoF_2, which has the same magnetic structure as MnF_2, a zero-field frequency of ~ 31 MHz was observed [251]; scaling by the ratio of the magnetic moments, a $S1$ frequency of ≈ 60 MHz is anticipated for MnF_2 if an analogous $F\,\mu\,F$ state is formed. However, the observed $S1$ frequency of $157(1)$ MHz is about three times larger than expected,

[2]In general, all techniques have systematic uncertainties that give rise to different results. However, techniques that are sensitive to static order around an impurity or defect (i.e. local probes such as the muon) likely have larger systematic effects than reciprocal space probes like magnetic X-ray or neutron diffraction.

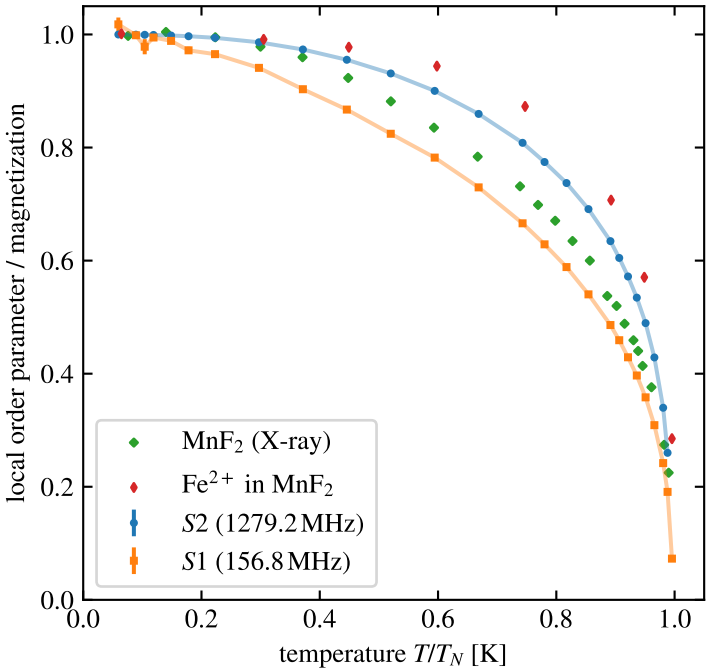

Figure 7.4: The normalized temperature dependence of the $S1$ (orange) and $S2$ (blue) frequencies, alongside the bulk magnetization (green) as obtained from X-ray diffraction [258] and the magnetization curve for Fe^{2+} impurities in MnF_2 (red) from Ref. [262].

indicating that if the muon adopts such a simple F μ F configuration, there must be an additional Fermi contact interaction (i.e. unpaired electronic spin density at the muon site) to account for the additional 100 MHz. We note that DFT calculations [by Kane Shenton (ETHZ)] so far find no indication of an additional contact term for a simple F μ F structure and predict precession frequencies of only ≈ 55 MHz, consistent with the F μ F estimate based on CoF_2.

The temperature dependence of the $S1$ line widths is significantly different from that of $S2$ [Fig. 7.2 (c) and (d)]. Close to T_N, $S1$ is fairly narrow ($\sim 5\,\mu s^{-1}$) compared to $S2$ ($> 100\,\mu s^{-1}$); due to its lower frequency, $S1$ is less susceptible to dephasing due to temperature gradients or sample small inhomogeneities since the rate of frequency change per temperature is about two orders of magnitudes lower. Below 60 K, the $S1$ damping rate increases and reaches $\approx 35\,\mu s^{-1}$ at low temperatures, in sharp contrast to the $S2$ component. The lack of spin-lattice relaxation at low temperatures [see Fig. 7.3] clearly indicates that the $S1$ linewidth is due to static inhomogeneous broadening. We can estimate the width of the field distribution (HWHM) to be ≈ 430 G or 6 MHz, roughly 4 % of the precession frequency. The origin of this broadening is not known. Both impurities and antiferromagnetic domain walls are expected to broaden both signals and can therefore be excluded as significant contributions. In addition, the decrease in line widths with increasing temperature cannot be due to motional narrowing, since such dynamic processes are expected to also affect the LF spectra [Fig. 7.3]. In the following, we present a speculative model that can explain these observations. We propose that the $S1$ signal may be

due to a F μ F state *plus* a nearby polaron, which can induce both lattice distortions and provide extra spin density at the muon site to account for the additional $\approx 100\,\mathrm{MHz}$. We attribute the low-temperature broadening of the $S1$ line to multiple polaron configurations that differ in both the location of the polaron and the magnitude of effective magnetic field on the muon. As a result, the muon experiences a static field distribution and the $S1$ signal thus represents the average of all configurations. It is reasonable to assume that each such configuration has a slightly different temperature dependence; this, possibly in combination with temperature-activated transitions into lower-energy configurations, can plausibly explain the temperature dependence of the line width. We note that this proposed F μ F-polaron complex is an overall charge-neutral muon state, just like $S2$; a speculative interpretation is that the muon undergoes a charge-exchange cycle in the deceleration process and either ends up with the electron (i.e. as the charge-neutral center with large hyperfine coupling, giving rise to the $S2$ signal), or looses the electron close to its final stopping site, and forms a F μ F state in close vicinity to the left-behind electron, which in turn localizes as a small polaron. While this model consistently explains the $S1$ signal, we note that at present, there is no evidence for such polaronic states in the DFT. A possible explanation is that the proposed overall multiple charge-neutral F μ F-polaron configurations are self-trapped metastable states far away from thermal equilibrium, which are challenging to accurately predict with DFT. Anecdotal support for the notion of $S1$ originating not simply from a F μ F state comes from a study from de Renzi *et al.* [252], which reports two oscillatory signals (with low signal-to-noise ratios) at 15 K, one at 67 MHz and one at 169 MHz; the former is consistent with expectations for the F μ F state, while the latter matches our observed $S1$ signal that we tentatively attribute to the F μ F-polaron complex.

Lastly, we discuss the deviation of the temperature dependence of the $S1$ frequency from both the $S2$ line and the bulk magnetization [Fig. 7.4]. Independent of the exact origin of the $S1$ signal, we expect that the presence of the muon, particularly in the F μ F state, causes significant lattice distortions. Since the dominant exchange coupling in MnF_2 is mediated via F ions [270], it is plausible and expected that muon-induced local distortion change the j-couplings in the immediate vicinity of the muon via modifications to wavefunction overlaps and bond angles. This in turn may significantly affect the effective order parameter measured by the muon and thus explain why S1 deviates from the bulk magnetization. We expect that the $S2$ signal is also affected but to a lesser extent, since the muon charge is partially screened by the tightly bound excess electron [256].

7.5 Conclusion

In summary, we carried out a detailed zero-field μSR study of the classic antiferromagnet MnF_2, and observed two oscillatory signals, $S1$ and $S2$, with frequencies at 3.8 K of 157(1) MHz and 1279.1(1) MHz. The high-frequency $S2$ line is attributed to a charge-neutral muon state with a large contact interaction, and the $S1$ signal is tentatively assigned to a F μ F-polaron complex; a detailed discussion of the candidate stopping sites within the unit cell, alongside DFT calculations, will be included in the planned publication.

The observation of S2, a charge-neutral center with a large Fermi contact interaction comparable to

that of Mu in vacuum clearly demonstrates that charge-neutral muon states can exist in different forms in magnetic compounds, analogous to the variety of Mu centers in non-magnetic materials [see Section 4.1]. We anticipate that MnF_2 may not be an isolated case; charge-neutral centers with large hyperfine couplings likely exist in other magnetic compounds. However, since most experiments on magnetic compounds are carried out in conventional spectrometers (which lack the required timing resolution to resolve the high frequencies), the signatures of charge-neutral states with large hyperfine couplings simply may have been missed. Importantly, even if the oscillatory signal itself is not observed, the charge-neutral center may still contribute to the signal in LF geometry (i.e. when there is a component of the initial muon spin along the effective magnetic field, see e.g. Fig. 7.3); if this signal is not recognized to originate from a charge-neutral center, it may lead to misinterpretation of μSR data. On the other hand, we note the possibility that charge-neutral centers with large hyperfine couplings may be easily identified *above* T_N (i.e. in the paramagnetic phase) by observing paramagnetic frequency shifts such as those reported in Ref. [252]; here, no fast-timing equipment is required.

Finally, the temperature dependence of the $S1$ and $S2$ frequencies clearly shows that the two signal components evolve differently with temperature, and comparison with the bulk magnetization shows that *neither* of the two frequencies tracks the bulk magnetic properties of the host as measured with X-rays [258]. While it is known that in principle μSR frequencies can deviate from the bulk magnetic order parameter [271, 272] and that muon-induced local distortions may modify the intrinsic behavior of the sample under certain circumstances [273], the present results are striking nonetheless; μSR is used extensively as a probe of magnetic materials, and observed frequencies are routinely used to monitor fluctuations and to some extent track the order parameter. We emphasize that our data do not indicate that the phase transition itself is influenced; therefore, the use of μSR to study phase diagrams, e.g. as a function of doping and pressure, does not appear to be affected. Nonetheless, the present data clearly demonstrate that at least in the case of MnF_2, the muon does not act as an "innocent" probe that passively measures the local magnetic environment; magnetic properties measured by μSR and the muon charge state and its electronic properties are closely intertwined, and both aspects have to be considered to make detailed statements about the nature of the ordered magnetic state. Charge-neutral muon centers, and in extension hydrogen impurities, do not only affect the *electronic* but also the *magnetic* properties of their host materials, and μSR is able to probe it locally. This may be particularly relevant since the study of the role of hydrogen as a magnetic impurity is a rapidly emerging field [265, 274–279], with effects reported in a range of different materials, displaying a wealth of mechanisms how hydrogen can modify magnetic properties. Lastly, we note that the detailed mechanisms of how the muon modifies the local magnetic environment in MnF_2 remain to be worked out and are very likely not limited to MnF_2. We therefore propose that a systematic study of the magnetic transition metal difluorides MF_2 (M =Cr, Mn, Fe, Co, Ni, Cu) [258, 280], which display a variety of different magnetic properties, should provide further insight.

Chapter 8

Summary and Outlook

In this thesis, we discussed the implications and applications of charge-neutral muon centers in a range of materials, with a particular focus on magnetic transition metal compounds. In Chapter 3, we introduced the concept of isotropic paramagnetic Mu in vacuum, a hydrogen-like bound state of a positive muon and an electron. As an example, we discussed vacuum-like Mu diffusing through the voids of an amorphous silica aerogel, where the measured isotropic hyperfine coupling reflects the dynamics associated with the binding and unbinding of Mu from the silica surface.

Then, in Chapter 4, we explored paramagnetic Mu inside non-magnetic materials. A variety of different centers can form, including deep interstitial Mu with a hyperfine coupling comparable to that of Mu in vacuum, shallow Mu with the bound electron spread out over many lattice sites, and more exotic configurations such as polaronic Mu and bond-centered Mu, where the electron is not centered on the muon. Since the electronic structures of Mu and charge-neutral hydrogen defects are virtually identical, paramagnetic Mu has been used extensively to investigate the dopant characteristics of isolated interstitial hydrogen impurities in a wide range of semiconductors and insulators [39–42]. We discussed the theory for anisotropic Mu and laid out the hallmark signatures of a paramagnetic Mu center, in particular in the decoupled regime where the electron Zeeman term is much larger than the muon-electron hyperfine interaction: since the bound electron is unpolarized and its spin is only weakly coupled to the lattice, the electron spin vector projects either along or opposite to the direction of the magnetic field; each Mu center gives rise to a characteristic pair of Mu satellite lines, with the line splitting determined by the *relative* orientation of the principal directions of the hyperfine tensor and the applied field. This orientation dependence was used to characterize the hyperfine coupling of the charge-neutral muon center in the transition metal oxide TiO_2. Previous μSR and ENDOR studies reported a paramagnetic muon-polaron center with the electron predominantly localizing on a Ti adjacent to the oxygen-bound muon (H) [46–48]. However, the hyperfine coupling expected from such a configuration is more than an order of magnitude larger than what is observed; additionally, the results for the H center measured with ENDOR and the muon center studied with μSR did not fully agree. While our study could not determine the precise nature of the muon-polaron complex in TiO_2 nor the reason for the apparent discrepancies

between μSR and ENDOR, we clearly showed that the hyperfine coupling of the charge-neutral muon (H) center is significantly more complicated than suggested by the previously proposed picture; several explanations and alternative models were considered, and an experiment to resolve the open questions was proposed.

Next, in Chapter 5, we turned our attention to magnetic materials. Prior to the work presented in this thesis, the antiferromagnetic transition metal difluoride MnF_2 was the only published case of a magnetic compound for which there was clear evidence for the presence of a charge-neutral muon center [45]. However, MnF_2 was mostly perceived as a curiosity rather than a template for other materials; charge-neutral muon centers were widely assumed to either simply not form or rapidly depolarize in the presence of magnetic moments, and were therefore rarely taken into consideration when analyzing μSR data from magnetic compounds. We carried out a detailed μSR investigation of the antiferromagnetic transition metal oxide Cr_2O_3, and observed three zero-field frequencies, attributed to three distinct muon environments E1-E3 with different internal magnetic fields. The temperature dependence revealed a rich dynamic behavior that we explained in terms of a thermally activated transition between E2 and E1, and intra-E3 local muon hopping. Notably, highly dynamic E3 muons and site-stable muons in E1 and E2 were observed at the same temperature. Supported by detailed density function theory calculations, this coexistence was consistently explained by the formation of a charge-neutral muon-polaron complex. Crucially, this charge-neutral center is *not paramagnetic* since the excess electron is strongly coupled to the unpaired $3d$ electrons of its Cr host. As a result, none of the characteristic features of paramagnetic Mu can be observed; the muon-polaron complex in Cr_2O_3 has characteristics that are very similar to the positive charge state, which is typically the only charge state considered relevant in magnetic compounds. However, despite its "hidden" nature, the formation of a charge-neutral muon-polaron complex can significantly alter how the muon interacts with its host material. Both the location and stability of muon stopping sites are changed, impacting the measured local magnetic fields and the *apparent* dynamical properties. The discovery of charge-neutral muon-polaron complexes in Cr_2O_3 suggests that analogous complexes with similarly inconspicuous signals likely exist in other semiconducting and insulating magnetic materials, in particular in transition metal compounds where the mulitvalent character of the transition metal ion may facilitate polaron formation.

Indeed, we observe similar charge-neutral muon states in antiferromagnetic Fe_2O_3 [Chapter 6]. The μSR spectra exhibit an unusually complicated temperature dependence, with three distinct muon spin precession frequencies that do not follow the magnetic order parameter, and relaxation rates that show several highly non-monotonic features. In conjunction with detailed density functional theory calculations, we explained the data with both local muon hopping, and, crucially, the presence of multiple charge-neutral muon-polaron complexes. In contrast to Cr_2O_3, several complex configurations are very close in energy and thus thermally accessible to the muon; as a result, rapid transitions between various complex configurations occur, driven by both muon and polaron dynamics, explaining the complicated temperature dependence of both precession frequencies and relaxation rates.

The observation of charge-neutral muon states in the antiferromagnets Cr_2O_3 and Fe_2O_3 demon-

strates that μSR can be used to investigate the dopant behavior of interstitial hydrogen in *magnetic* oxides. By analogy between the muon and proton, we provided, for the first time, detailed information on the electronic structure of isolated hydrogen complexes, and, in the case of Fe_2O_3, evidence for its donor behavior. This is important since conventional spectroscopic methods such as electron spin resonance, which can be used to study hydrogen in nonmagnetic semiconductors and insulators, are not generally applicable in magnetic materials.

Having established that charge-neutral centers *do* form in magnetic compounds and MnF_2 is not a curious isolated case, we revisited this classic uniaxial antiferromagnet in Chapter 7. We observed two zero-field signals with frequencies of 157(1) MHz and 1279.1(1) MHz at 3.8 K, consistent with previous results by Uemura *et al.* [45]. The high-frequency line is attributed to a charge-neutral center with a large Fermi contact coupling, comparable to that of deep interstitial Mu centers observed in e.g. Si [117] and in contrast to the relatively low hyperfine coupling of the muon-polaron complexes in Cr_2O_3 and Fe_2O_3. This demonstrates that charge-neutral muon centers in magnetic materials can exist in a variety of shapes, analogous to the multitude of paramagnetic Mu species in non-magnetic compounds. Remarkably, the two frequencies observed in MnF_2 do not have the same temperature dependence, and *neither* tracks the bulk magnetization. Evidently, at least in MnF_2, the muon does not act as a non-perturbative probe that passively measures its local magnetic environment; instead, we showed that the magnetic properties measured by μSR and the muon charge state and its electronic properties are closely intertwined, and both aspects have to be considered to make detailed statements about the nature of the ordered magnetic state. Consistent with a very recent study by Jani *et al.* [265], which shows that hydrogenation has a marked affect on the magnetic anisotropy in Fe_2O_3, our data suggest that charge-neutral muon centers, and in extension hydrogen impurities, have the ability to not only affect the *electronic* but also the *magnetic* properties of their host materials. Thus our results in MnF_2 indicate that μSR may be a powerful tool to investigate the role of hydrogen defects as *magnetic* impurities.

The combined results of our μSR studies in Cr_2O_3, Fe_2O_3 and MnF_2 [Chapters 5, 6 and 7] inform a general hypothesis: charge-neutral centers are as prevalent in magnetic compounds as they are in non-magnetic materials, and can form different species with a similar variety, including muon-polaron complexes and interstitial centers with large hyperfine coupling. At face value, this is not a surprising result; charge-neutral muon states form in virtually *all* non-magnetic semiconductors and insulators [39–42], and there is no apparent reason why they should not exist in their magnetic counterparts. However, contrary to the assumption that charge-neutral centers are automatically paramagnetic, the excess electron is strongly bound to the unpaired electrons of the magnetic host, which fully determines its spin state. As a result, there is only *one* frequency from the charge-neutral center in a magnetic material[1]; the effect of the electron on the muon can be expressed as an effective magnetic field, and

[1]Technically, there *are* two different spin states due to the two different magnetic sublattices, however the (absolute) frequencies are the same since the internal field changes sign concurrently with the spin state when changing to a different sublattice. If external fields are applied, these two spin states can be separated; however, the positive charge state *also* experiences two internal fields and splits in an applied field; unlike for non-magnetic materials in applied fields, there is no distinction between the two charge states.

the electron spin state is determined by the magnetic anisotropy rather than the applied magnetic field. We proposed the following terminology: *any* charge-neutral muon-electron bound state is referred to as such, independent of the material it is formed in. The term muonium is reserved exclusively for *paramagnetic* centers, i.e. charge-neutral muon states in vacuum and non-magnetic compounds where the spin of the excess electron is unpaired and only weakly coupled to the lattice.

The identification of charge-neutral muon states in magnetic materials can be challenging: Centers with a large Fermi-contact interaction can easily be identified by their high-frequency signal, but only *if it is observed.* This, however, requires specialized high-timing equipment so that such high frequency signals can be detected with reasonable amplitude; the general-purpose spectrometers that are typically used to study magnetic materials in zero or low magnetic fields lack the timing resolution and cannot resolve the fast oscillations. Therefore, it is possible that charge-neutral centers with large hyperfine couplings have simply been missed in a range of magnetic compounds. In contrast, the precession frequencies from muon-polaron complexes in magnetic compounds are comparable to those of the positive charge state, since the hyperfine coupling is predominantly dipolar and therefore comparatively low; as a consequence, these charge-neutral centers "hide in plain sight".

Despite their inconspicuous signals, the presence of charge-neutral centers in magnetic materials can have a profound impact on the μSR signals, and therefore significant implications for the interpretation of magnetism-related μSR spectra. The cases of Fe_2O_3 and MnF_2 demonstrate that charge-neutral muon states have the ability to not only affect the magnitude but also the temperature dependence of the precession signals such that they no longer reflect the intrinsic magnetic properties. Interestingly, the underlying mechanisms are very different: for Fe_2O_3, transitions between various muon-polaron complex configurations plausibly account for the temperature dependence, whereas for MnF_2, the excess electron, partially shared with a nearby Mn ion, changes the magnetic properties of that particular Mn ion in such a way that the observed frequency markedly diverge from the bulk magnetization. Depolarization rates are also affected: in Fe_2O_3, the damping rates of the frequency signals spike at temperatures where transitions between polaron configurations occur. A similar response is expected to be observable for measurements in LF geometry, i.e. with the initial spin along the direction of the internal field. Similarly, if a high-frequency center is present, it may contribute to the LF spectra [see e.g. Fig. 7.3] even if the high-frequency signal itself cannot be observed. In general, multi-component signals due to the multiple charge states appear especially relevant in compounds with more complicated spin and crystal structure, where precession signals are often rapidly damped or entirely unresolved.

The results and implications of this thesis present a challenge for μSR experiments in non-conductive magnetic materials, however we strongly emphasize that the discovery and characterization of charge-neutral muon states in magnetic materials also significantly *strengthens* the muon as a sensitive probe for magnetism - the better we understand how the muon interacts with its magnetic host, the more useful information we can extract. We note that in principle, both long-range magnetic order and quantum phase transitions can be equally well detected by both the charge-neutral and the positive muon charge state. The two different charge states provide complimentary information that would not be accessible

otherwise; for example, in MnF_2, the charge-neutral center allows direct insight into how hydrogen defects act as magnetic impurities. Density functional theory (DFT) has proven enormously helpful in the identification of plausible charge-neutral states, in particular muon-polaron complexes. However, as the case of the muon-polaron complex in TiO_2 shows, DFT is not (yet) a silver bullet and there remain significant challenges for the accurate prediction of metastable and polaronic states. These issues are currently the subject of intense research, and there are several promising developments (e.g. Refs [281, 282]); we anticipate that DFT will be able to accurately predict muon behavior in the future, and expect that detailed DFT calculations will become an integral part of μSR studies.

In essence, this thesis bridges the previously separate fields of magnetism and muonium research. However, the present results represent just the beginning. Going forward, the development of a deeper understanding of (1) the variety of types of charge-neutral states in magnetic compounds, (2) how they affect the μSR signal and (3) under what circumstances they form is critical. Considering both the results of this thesis and the extensive literature on Mu in non-magnetic materials [39–42], a combination of the electronic, magnetic and crystal structure is expected to play a role in the determination of the nature of charge-neutral muon (and hydrogen) states. What is needed is a comprehensive theory that can predict which muon charge-states form prior to experiment, and, in a second step, how both the electronic and magnetic structure are affected by simple hydrogenic impurities. This way, μSR can be used both to study the intrinsic magnetic properties as well as the effect of hydrogen as a magnetic and electronic impurity. A thorough understanding of unintentional hydrogen doping is particularly relevant for transition metal compounds, which form the basis for a large number of current developments in condensed matter physics (including spintronics [205–209], dilute magnetic semiconductors [210], metal-insulator transitions [283], multiferroics [211] and superconductivity [212]). We propose a systematic (re)examination of μSR results of binary magnetic first-row transition metal oxides, including repeats of some experiments considering that both sample growth procedures and experimental setups significantly improved since the early days of μSR. In addition, as the example of TiO_2 shows, muon-polaron complexes are not fully understood even in non-magnetic compounds, and further research is urgently required.

Bibliography

[1] R. L. Garwin, L. M. Lederman, and M. Weinrich, "Observations of the Failure of Conservation of Parity and Charge Conjugation in Meson Decays: The Magnetic Moment of the Free Muon," Physical Review **105**, 1415–1417 (1957).

[2] T. D. Lee and C. N. Yang, "Question of Parity Conservation in Weak Interactions," Physical Review **104**, 254–258 (1956).

[3] C. S. Wu, E. Ambler, R. W. Hayward, D. D. Hoppes, and R. P. Hudson, "Experimental Test of Parity Conservation in Beta Decay," Physical Review **105**, 1413–1415 (1957).

[4] I. Beltrami, H. Bukkard, R. Von Dincklage, W. Fetscher, H.-J. Gerber, K. Johnson, E. Pedroni, M. Salzmann, and F. Schenk, "Muon decay: Measurement of the integral asymmetry parameter," Physics Letters B **194**, 326–330 (1987).

[5] S. H. Neddermeyer and C. D. Anderson, "Note on the Nature of Cosmic-Ray Particles," Physical Review **51**, 884–886 (1937).

[6] J. Street and E. Stevenson, "New Evidence for the Existence of a Particle of Mass Intermediate Between the Proton and Electron," Physical Review **52**, 1003–1004 (1937).

[7] C. M. G. Lattes, H. Muirhead, G. P. S. Occhialini, and C. F. Powell, "Processes involving charged mesons," Nature **159**, 694–697 (1947).

[8] C. M. G. Lattes, G. P. S. Occhialini, and C. F. Powell, "Observations on the Tracks of Slow Mesons in Photographic Emulsions," Nature **160**, 453–456 (1947).

[9] G. Backenstoss, B. D. Hyams, G. Knop, P. C. Marin, and U. Stierlin, "Helicity of μ - Mesons from π - Meson Decay," Physical Review Letters **6**, 415–416 (1961).

[10] M. Bardon, P. Franzini, and J. Lee, "Helicity of μ - Mesons; Mott Scattering of Polarized Muons," Physical Review Letters **7**, 23–25 (1961).

[11] D. J. Griffiths, *Introduction to Elementary Particles*, 2nd ed., Physics Textbook (Wiley-VCH, Weinheim, 2011).

[12] S. J. Blundell, "Spin-polarized muons in condensed matter physics," Contemporary Physics **40**, 175–192 (1999).

[13] A. Yaouanc and P. Dalmas de Réotier, *Muon Spin Rotation, Relaxation, and Resonance* (Oxford University Press, 2011).

[14] A. Schenck and F. Gygax, "Chapter 2 Magnetic materials studied by muon spin rotation spectroscopy," in *Handbook of Magnetic Materials*, Vol. 9 (Elsevier, 1995) pp. 57–302.

[15] P. D. de Réotier and A. Yaouanc, "Muon spin rotation and relaxation in magnetic materials," Journal of Physics: Condensed Matter **9**, 9113–9166 (1997).

[16] Y. J. Uemura, G. M. Luke, B. J. Sternlieb, J. H. Brewer, J. F. Carolan, W. N. Hardy, R. Kadono, J. R. Kempton, R. F. Kiefl, S. R. Kreitzman, P. Mulhern, T. M. Riseman, D. L. Williams, B. X. Yang, S. Uchida, H. Takagi, J. Gopalakrishnan, A. W. Sleight, M. A. Subramanian, C. L. Chien, M. Z. Cieplak, G. Xiao, V. Y. Lee, B. W. Statt, C. E. Stronach, W. J. Kossler, and X. H. Yu, "Universal Correlations between T_c and n_s/ m_* (Carrier Density over Effective Mass) in High-T_c Cuprate Superconductors," Physical Review Letters **62**, 2317–2320 (1989).

[17] G. M. Luke, Y. Fudamoto, K. M. Kojima, M. I. Larkin, J. Merrin, B. Nachumi, Y. J. Uemura, Y. Maeno, Z. Q. Mao, Y. Mori, H. Nakamura, and M. Sigrist, "Time-reversal symmetry-breaking superconductivity in Sr_2 RuO_4," Nature **394**, 558–561 (1998).

[18] J. E. Sonier, J. H. Brewer, and R. F. Kiefl, "μSR studies of the vortex state in type-II superconductors," Rev. Mod. Phys. **72**, 43 (2000).

[19] J. E. Sonier, "Muon spin rotation studies of electronic excitations and magnetism in the vortex cores of superconductors," Reports on Progress in Physics **70**, 1717–1755 (2007).

[20] P. Carretta, R. De Renzi, G. Prando, and S. Sanna, "A view from inside iron-based superconductors," Physica Scripta **88**, 068504 (2013).

[21] A. Bhattacharyya, D. T. Adroja, M. Smidman, and V. K. Anand, "A brief review on μSR studies of unconventional Fe- and Cr-based superconductors," Science China Physics, Mechanics and Astronomy **61**, 127402 (2018).

[22] C. Niedermayer, C. Bernhard, T. Blasius, A. Golnik, A. Moodenbaugh, and J. I. Budnick, "Common Phase Diagram for Antiferromagnetism in $La_{2-x}Sr_xCuO_4$ and $Y_{1-x}Ca_xBa_2Cu_3O_6$ as Seen by Muon Spin Rotation," Physical Review Letters **80**, 3843–3846 (1998).

[23] H. Luetkens, H.-H. Klauss, M. Kraken, F. J. Litterst, T. Dellmann, R. Klingeler, C. Hess, R. Khasanov, A. Amato, C. Baines, M. Kosmala, O. J. Schumann, M. Braden, J. Hamann-Borrero, N. Leps, A. Kondrat, G. Behr, J. Werner, and B. Büchner, "The electronic phase diagram of the $LaO_{1-x}F_xFeAs$ superconductor," Nature Materials **8**, 305–309 (2009).

[24] A. V. Boris, Y. Matiks, E. Benckiser, A. Frano, P. Popovich, V. Hinkov, P. Wochner, M. Castro-Colin, E. Detemple, V. K. Malik, C. Bernhard, T. Prokscha, A. Suter, Z. Salman, E. Morenzoni, G. Cristiani, H.-U. Habermeier, and B. Keimer, "Dimensionality Control of Electronic Phase Transitions in Nickel-Oxide Superlattices," Science **332**, 937–940 (2011).

[25] J. S. Gardner, S. R. Dunsiger, B. D. Gaulin, M. J. P. Gingras, J. E. Greedan, R. F. Kiefl, M. D. Lumsden, W. A. MacFarlane, N. P. Raju, J. E. Sonier, I. Swainson, and Z. Tun, "Cooperative Paramagnetism in the Geometrically Frustrated Pyrochlore Antiferromagnet $Tb_2Ti_2O_7$," Physical Review Letters **82**, 1012–1015 (1999).

[26] M. J. P. Gingras and P. A. McClarty, "Quantum spin ice: A search for gapless quantum spin liquids in pyrochlore magnets," Reports on Progress in Physics **77**, 056501 (2014).

[27] P. Dalmas de Réotier, A. Maisuradze, and A. Yaouanc, "Recent μSR Studies of Insulating Rare-Earth Pyrochlore Magnets," Journal of the Physical Society of Japan **85**, 091010 (2016).

[28] Y. J. Uemura, T. Yamazaki, D. R. Harshman, M. Senba, and E. J. Ansaldo, "Muon-spin relaxation in *Au* Fe and *Cu* Mn spin glasses," Physical Review B **31**, 546–563 (1985).

[29] S. J. Blundell, "Molecular magnets," Contemporary Physics **48**, 275–290 (2007).

[30] G. Kalvius, D. Noakes, and O. Hartmann, "μSR studies of rare-earth and actinide magnetic materials," in *Handbook on the Physics and Chemistry of Rare Earths*, Vol. 32 (Elsevier, 2001) pp. 55–451.

[31] V. W. Hughes, D. W. McColm, K. Ziock, and R. Prepost, "Formation of Muonium and Observation of its Larmor Precession," Physical Review Letters **5**, 63–65 (1960).

[32] D. C. Walker, *Muon and Muonium Chemistry* (Cambridge University Press, Cambridge, 1983).

[33] D. G. Fleming, S. P. Cottrell, I. McKenzie, and K. Ghandi, "Rate constants for the slow Mu + propane abstraction reaction at 300 K by diamagnetic RF resonance," Physical Chemistry Chemical Physics **17**, 19901–19910 (2015).

[34] T. A. Claxton, "Aspects of muonium chemistry," Chemical Society Reviews **24**, 437 (1995).

[35] N. J. Clayden, "Muons in chemistry," Physica Scripta **88**, 068507 (2013).

[36] A. Shluger, "Defects in Oxides in Electronic Devices," in *Handbook of Materials Modeling*, edited by W. Andreoni and S. Yip (Springer International Publishing, Cham, 2019) pp. 1–22.

[37] S. J. Pearton, J. W. Corbett, and T. S. Shi, "Hydrogen in crystalline semiconductors," Applied Physics A Solids and Surfaces **43**, 153–195 (1987).

[38] C. G. Van de Walle and J. Neugebauer, "Universal alignment of hydrogen levels in semiconductors, insulators and solutions," Nature **423**, 626–628 (2003).

[39] K. Chow, B. Hitti, and R. Kiefl, "Chapter 4: μSR on Muonium in Semiconductors and Its Relation to Hydrogen," in *Semiconductors and Semimetals*, Vol. 51 (Elsevier, 1998) pp. 137–207.

[40] S. F. J. Cox, J. L. Gavartin, J. S. Lord, S. P. Cottrell, J. M. Gil, H. V. Alberto, J. P. Duarte, R. C. Vilão, N. A. de Campos, D. J. Keeble, E. A. Davis, M. Charlton, and D. P. van der Werf, "Oxide muonics: II. Modelling the electrical activity of hydrogen in wide-gap and high-permittivity dielectrics," Journal of Physics: Condensed Matter **18**, 1079–1119 (2006).

[41] S. F. J. Cox, J. S. Lord, S. Cottrell, J. M. Gil, H. V. Alberto, A. Keren, D. Prabhakaran, R. Scheuermann, and A. Stoykov, "Oxide muonics: I. Modelling the electrical activity of hydrogen in semiconducting oxides," Journal of Physics: Condensed Matter **18**, 1061–1078 (2006).

[42] S. F. J. Cox, "Muonium as a model for interstitial hydrogen in the semiconducting and semimetallic elements," Reports on Progress in Physics **72**, 116501 (2009).

[43] W. A. MacFarlane, R. F. Kiefl, S. Dunsiger, J. E. Sonier, J. Chakhalian, J. E. Fischer, T. Yildirim, and K. H. Chow, "Muon-spin-relaxation studies of the alkali-fulleride superconductors," Physical Review B **58**, 1004–1024 (1998).

[44] H. Graf, W. Hofmann, W. Kündig, P. F. Meier, B. D. Patterson, W. Reichhart, and A. Rodriguez, "Muon Spin Rotation (μSR) in α-Fe_2O_3," Hyperfine Interactions **4**, 452 (1978).

[45] Y. J. Uemura, R. Keitel, M. Senba, R. F. Kiefl, S. R. Kreitzman, D. R. Noakes, J. H. Brewer, D. R. Harshman, E. J. Ansaldo, K. M. Crowe, A. M. Portis, and V. Jaccarino, "μSR studies on pure MnF_2 and site-diluted $(Mn_{0.5}Zn_{0.5})F_2$," Hyperfine Interactions **31**, 313–318 (1986).

[46] A. T. Brant, N. C. Giles, and L. E. Halliburton, "Hydrogen donors and Ti^{3+} ions in reduced TiO_2 crystals," Journal of Applied Physics **110**, 053714 (2011).

[47] R. C. Vilão, R. B. L. Vieira, H. V. Alberto, J. M. Gil, A. Weidinger, R. L. Lichti, B. B. Baker, P. W. Mengyan, and J. S. Lord, "Muonium donor in rutile TiO_2 and comparison with hydrogen," Physical Review B **92**, 081202(R) (2015).

[48] K. Shimomura, R. Kadono, A. Koda, K. Nishiyama, and M. Mihara, "Electronic structure of Mu-complex donor state in rutile TiO_2," Physical Review B **92**, 075203 (2015) (2015).

[49] D. Dubbers and H.-J. Stöckmann, *Quantum Physics: The Bottom-Up Approach*, Graduate Texts in Physics (Springer, Berlin, Heidelberg, 2013).

[50] K. Dorenburg, M. Gladisch, D. Herlach, W. Mansel, H. Metz, H. Orth, G. zu Putlitz, A. Seeger, W. Wahl, and M. Wigand, "Trapping by vacancies and mobility of positive muons in neutron-irradiated aluminium," Zeitschrift für Physik B Condensed Matter **31**, 165–169 (1978).

[51] K. Jacobs, *Quantum Measurement Theory and Its Applications* (Cambridge University Press, Cambridge; New York, 2014).

[52] H. V. Alberto, A. Weidinger, R. C. Vilão, J. P. Duarte, J. M. Gil, J. S. Lord, and S. F. J. Cox, "Mechanisms of electron polarization of shallow muonium in CdTe and CdS," Physical Review B **81**, 245205 (2010).

[53] W. Liu, M. G. Boshier, S. Dhawan, O. van Dyck, P. Egan, X. Fei, M. Grosse Perdekamp, V. W. Hughes, M. Janousch, K. Jungmann, D. Kawall, F. G. Mariam, C. Pillai, R. Prigl, G. zu Putlitz, I. Reinhard, W. Schwarz, P. A. Thompson, and K. A. Woodle, "High Precision Measurements of the Ground State Hyperfine Structure Interval of Muonium and of the Muon Magnetic Moment," Physical Review Letters **82**, 711–714 (1999).

[54] S. Kanda, Y. Fukao, Y. Ikedo, K. Ishida, M. Iwasaki, D. Kawall, N. Kawamura, K. Kojima, N. Kurosawa, Y. Matsuda, T. Mibe, Y. Miyake, S. Nishimura, N. Saito, Y. Sato, S. Seo, K. Shimomura, P. Strasser, K. Tanaka, T. Tanaka, H. Torii, A. Toyoda, and Y. Ueno, "New precise spectroscopy of the hyperfine structure in muonium with a high-intensity pulsed muon beam," Physics Letters B **815**, 136154 (2021).

[55] C. J. Oram, J. M. Bailey, P. W. Schmor, C. A. Fry, R. F. Kiefl, J. B. Warren, G. M. Marshall, and A. Olin, "Measurement of the Lamb Shift in Muonium," Physical Review Letters **52**, 910–913 (1984).

[56] S. G. Karshenboim, "Precision physics of simple atoms: QED tests, nuclear structure and fundamental constants," Physics Reports **422**, 1–63 (2005).

[57] A. Antognini, P. Crivelli, T. Prokscha, K. S. Khaw, B. Barbiellini, L. Liszkay, K. Kirch, K. Kwuida, E. Morenzoni, F. M. Piegsa, Z. Salman, and A. Suter, "Muonium Emission into Vacuum from Mesoporous Thin Films at Cryogenic Temperatures," Physical Review Letters **108**, 143401 (2012).

[58] K. S. Khaw, A. Antognini, T. Prokscha, K. Kirch, L. Liszkay, Z. Salman, and P. Crivelli, "Spatial confinement of muonium atoms," Physical Review A **94**, 022716 (2016).

[59] S. G. Karshenboim and E. Y. Korzinin, "Theoretical prediction for the muonium hyperfine-structure interval and its accuracy," Physical Review A **103**, 022805 (2021).

[60] Y. Miyake, N. Nishida, J. Yoshino, W. Higemoto, E. Torikai, K. Shimomura, Y. Ikedo, N. Kawamura, P. Strasser, S. Makimura, H. Fujimori, K. Nakahara, A. Koda, Y. Kobayashi, K. Nishiyama, R. Kadono, T. Ogitsu, Y. Makida, K. Sasaki, T. Adachi, and K. Nagamine, "Ultra Slow Muon Microscopy for Nano-science," Journal of Physics: Conference Series **302**, 012038 (2011).

[61] P. Bakule, Y. Matsuda, Y. Miyake, K. Nagamine, M. Iwasaki, Y. Ikedo, K. Shimomura, P. Strasser, and S. Makimura, "Pulsed source of ultra low energy positive muons for near-surface μSR studies," Nuclear Instruments and Methods in Physics Research Section B: Beam Interactions with Materials and Atoms **266**, 335–346 (2008).

[62] M. Abe, S. Bae, G. Beer, G. Bunce, H. Choi, S. Choi, M. Chung, W. da Silva, S. Eidelman, M. Finger, Y. Fukao, T. Fukuyama, S. Haciomeroglu, K. Hasegawa, K. Hayasaka, N. Hayashizaki, H. Hisamatsu, T. Iijima, H. Iinuma, H. Ikeda, M. Ikeno, K. Inami, K. Ishida, T. Itahashi, M. Iwasaki, Y. Iwashita, Y. Iwata, R. Kadono, S. Kamal, T. Kamitani, S. Kanda, F. Kapusta, K. Kawagoe, N. Kawamura, B. Kim, Y. Kim, T. Kishishita, R. Kitamura, H. Ko, T. Kohriki, Y. Kondo, T. Kume, M. J. Lee, S. Lee, W. Lee, G. M. Marshall, Y. Matsuda, T. Mibe, Y. Miyake, T. Murakami, K. Nagamine, H. Nakayama, S. Nishimura, D. Nomura, T. Ogitsu, S. Ohsawa, K. Oide, Y. Oishi, S. Okada, A. Olin, Z. Omarov, M. Otani, G. Razuvaev, A. Rehman, N. Saito, N. F. Saito, K. Sasaki, O. Sasaki, N. Sato, Y. Sato, Y. K. Semertzidis, H. Sendai, Y. Shatunov, K. Shimomura, M. Shoji, B. Shwartz, P. Strasser, Y. Sue, T. Suehara, C. Sung, K. Suzuki, T. Takatomi, M. Tanaka, J. Tojo, Y. Tsutsumi, T. Uchida, K. Ueno, S. Wada, E. Won, H. Yamaguchi, T. Yamanaka, A. Yamamoto, T. Yamazaki, H. Yasuda, M. Yoshida, and T. Yoshioka, "A new approach for measuring the muon anomalous magnetic moment and electric dipole moment," Progress of Theoretical and Experimental Physics **2019**, 053C02 (2019).

[63] A. Adelmann, M. Backhaus, C. C. Barajas, N. Berger, T. Bowcock, C. Calzolaio, G. Cavoto, R. Chislett, A. Crivellin, M. Daum, M. Fertl, M. Giovannozzi, G. Hesketh, M. Hildebrandt, I. Keshelashvili, A. Keshavarzi, K. S. Khaw, K. Kirch, A. Kozlinskiy, A. Knecht, M. Lancaster, B. Markisch, F. M. Aeschbacher, F. Meot, A. Nass, A. Papa, J. Pretz, J. Price, F. Rathmann, F. Renga, M. Sakurai, P. Schmidt-Wellenburg, A. Schoning, M. Schott, C. Voena, J. Vossebeld, F. Wauters, and P. Winter, "Search for a muon EDM using the frozen-spin technique," arXiv , 2102.08838 (2021).

[64] G. A. Beer, Y. Fujiwara, S. Hirota, K. Ishida, M. Iwasaki, S. Kanda, H. Kawai, N. Kawamura, R. Kitamura, S. Lee, W. Lee, G. M. Marshall, T. Mibe, Y. Miyake, S. Okada, K. Olchanski, A. Olin, H. Ohnishi, Y. Oishi, M. Otani, N. Saito, K. Shimomura, P. Strasser, M. Tabata, D. Tomono, K. Ueno, E. Won, and K. Yokoyama, "Enhancement of muonium emission rate from silica aerogel with a laser-ablated surface," Progress of Theoretical and Experimental Physics **2014**, 91C01–0 (2014).

[65] E. Morenzoni, T. Prokscha, A. Suter, H. Luetkens, and R. Khasanov, "Nano-scale thin film investigations with slow polarized muons," Journal of Physics: Condensed Matter **16**, S4583–S4601 (2004).

[66] P. Strasser, Y. Ikedo, S. Makimura, J. Nakamura, K. Nishiyama, K. Shimomura, H. Fujimori, T. Adachi, A. Koda, N. Kawamura, Y. Kobayashi, W. Higemoto, T. U. Ito, T. Nagatomo, E. Torikai, R. Kadono, and Y. Miyake, "Design and construction of the ultra-slow muon beamline at J-PARC/MUSE," Journal of Physics: Conference Series **551**, 012065 (2014).

[67] A. P. Mills, J. Imazato, S. Saitoh, A. Uedono, Y. Kawashima, and K. Nagamine, "Generation of Thermal Muonium in Vacuum," Physical Review Letters **56**, 1463–1466 (1986).

[68] K. Nagamine, Y. Miyake, K. Shimomura, P. Birrer, J. P. Marangos, M. Iwasaki, P. Strasser, and T. Kuga, "Ultraslow Positive-Muon Generation by Laser Ionization of Thermal Muonium from Hot Tungsten at Primary Proton Beam," Physical Review Letters **74**, 4811–4814 (1995).

[69] A. Pant, K. Ishida, N. Kawamura, S. Matoba, A. Koda, S. Nishimura, and K. Shimomura, "Study of muonium behavior in n-type silicon for generation of ultra cold muonium in vacuum," Physica B: Condensed Matter **613**, 412997 (2021).

[70] G. Marshall, J. Warren, D. Garner, G. Clark, J. Brewer, and D. Fleming, "Production of thermal muonium in the vacuum between the grains of fine silica powders," Physics Letters A **65**, 351–353 (1978).

[71] R. F. Kiefl, J. B. Warren, C. J. Oram, G. M. Marshall, J. H. Brewer, D. R. Harshman, and C. W. Clawson, "Surface interactions of muonium in oxide powders at low temperatures," Physical Review B **26**, 2432 (1982).

[72] G. A. Beer, G. M. Marshall, G. R. Mason, A. Olin, Z. Gelbart, K. R. Kendall, T. Bowen, P. G. Halverson, A. E. Pifer, C. A. Fry, J. B. Warren, and A. R. Kunselman, "Emission of Muonium into Vacuum from a Silica-Powder Layer," Physical Review Letters **57**, 671–674 (1986).

[73] M. H. Dehn, D. J. Arseneau, M. D. Bridges, T. Buck, D. L. Cortie, S. P. Cottrell, D. G. Fleming, J. A. Kelly, W. A. MacFarlane, M. J. MacLachlan, G. D. Morris, I. McKenzie, J. Xiao, and R. F. Kiefl, "Spin Depolarization of Muonium in Mesoporous Silica," Journal of Physics: Conference Series **551**, 012006 (2014).

[74] M. H. Dehn, D. J. Arseneau, P. Böni, M. D. Bridges, T. Buck, D. L. Cortie, D. G. Fleming, J. A. Kelly, W. A. MacFarlane, M. J. MacLachlan, R. M. L. McFadden, G. D. Morris, P.-X. Wang, J. Xiao, V. M. Zamarion, and R. F. Kiefl, "Communication: Chemisorption of muonium on gold nanoparticles: A sensitive new probe of surface magnetism and reactivity," The Journal of Chemical Physics **145**, 181102 (2016).

[75] M. H. Dehn, D. G. Fleming, W. A. MacFarlane, M. J. MacLachlan, V. M. Zamarion, and R. F. Kiefl, "Dynamics of Anisotropic Muonium on Silica Surfaces Explained by Monte Carlo Simulation of the Muon Depolarization," Proc. 14th Int. Conf. on Muon Spin Rotation, Relaxation and Resonance (Journal of the Physical Society of Japan) **21**, 011032 (2018).

[76] M. H. Dehn, Y. Cao, P.-X. Wang, S. P. Cottrell, M. J. MacLachlan, D. G. Fleming, and R. F. Kiefl, "Direct observation of muonium reacting with uncapped gold nanoparticles in porous silica and nature of the final state," The Journal of Chemical Physics **152**, 184706 (2020).

[77] M. Tabata, I. Adachi, H. Kawai, T. Sumiyoshi, and H. Yokogawa, "Hydrophobic silica aerogel production at KEK," Nuclear Instruments and Methods in Physics Research Section A: Accelerators, Spectrometers, Detectors and Associated Equipment **668**, 64–70 (2012).

[78] A. Soleimani Dorcheh and M. Abbasi, "Silica aerogel; synthesis, properties and characterization," Journal of Materials Processing Technology **199**, 10–26 (2008).

[79] P. Bakule, G. A. Beer, D. Contreras, M. Esashi, Y. Fujiwara, Y. Fukao, S. Hirota, H. Iinuma, K. Ishida, M. Iwasaki, T. Kakurai, S. Kanda, H. Kawai, N. Kawamura, G. M. Marshall, H. Masuda, Y. Matsuda, T. Mibe, Y. Miyake, S. Okada, K. Olchanski, A. Olin, H. Onishi, N. Saito, K. Shimomura, P. Strasser, M. Tabata, D. Tomono, K. Ueno, K. Yokoyama, and S. Yoshida, "Measurement of muonium emission from silica aerogel," Progress of Theoretical and Experimental Physics **2013**, 103C01–103C01 (2013).

[80] J. Beare, G. Beer, J. H. Brewer, T. Iijima, K. Ishida, M. Iwasaki, S. Kamal, K. Kanamori, N. Kawamura, R. Kitamura, S. Li, G. M. Luke, G. M. Marshall, T. Mibe, Y. Miyake, Y. Oishi, K. Olchanski, A. Olin, M. Otani, M. A. Rehman, N. Saito, Y. Sato, K. Shimomura, K. Suzuki, M. Tabata, and G. Yasuda, "Study of muonium emission from laser-ablated silica aerogel," Progress of Theoretical and Experimental Physics **2020**, 123C01 (2020).

[81] M. H. Dehn, R. Scheuermann, P.-X. Wang, Y. Cao, M. J. MacLachlan, V. M. Zamarion, D. G. Fleming, and R. F. Kiefl, "Precision measurement of the muonium hyperfine interaction in mesoporous silica and aerogel," Physical Review Research **3**, 013029 (2021).

[82] C. P. Slichter, *Principles of Magnetic Resonance* (Springer, Berlin; Heidelberg, 1990).

[83] M. Bucher, "The electron inside the nucleus: An almost classical derivation of the isotropic hyperfine interaction," European Journal of Physics **21**, 19–22 (2000).

[84] R. P. Feynman, R. B. Leighton, M. Sands, M. A. Gottlieb, and R. Leighton, eds., *The Feynman Lectures on Physics*, definitive ed. ed., Vol. 3 (Pearson, Addison-Wesley, San Francisco, Calif., 2006).

[85] R. F. Kiefl, B. D. Patterson, E. Holzschuh, W. Odermatt, and D. R. Harshman, "Hyperfine splitting of muonium in SiO_2 powder," Hyperfine Interactions **18**, 563–566 (1984).

[86] S. Brunauer, P. H. Emmett, and E. Teller, "Adsorption of Gases in Multimolecular Layers," Journal of the American Chemical Society **60**, 309–319 (1938).

[87] R. F. Marzke, W. S. Glaunsinger, D. R. Harshman, E. J. Ansaldo, R. Keitel, M. Senba, D. R. Noakes, D. P. Spencer, and J. H. Brewer, "μ2SR measurement of the reaction rate of muonium with a supported platinum catalyst," Chemical physics letters **120**, 6–10 (1985).

[88] A. Suter and B. Wojek, "Musrfit: A Free Platform-Independent Framework for μSR Data Analysis," Physics Procedia **30**, 69–73 (2012).

[89] A. Adelmann, U. Locans, and A. Suter, "The Dynamic Kernel Scheduler—Part 1," Computer Physics Communications **207**, 83–90 (2016).

[90] U. Locans, A. Adelmann, A. Suter, J. Fischer, W. Lustermann, G. Dissertori, and Q. Wang, "Real-time computation of parameter fitting and image reconstruction using graphical processing units," Computer Physics Communications **215**, 71–80 (2017).

[91] U. Locans and A. Suter, "MUSRFIT –Real Time Parameter Fitting Using GPUs," Journal of the Physical Society of Japan **21**, 011051 (2018).

[92] P. Petit, M. Desaintfuscien, and C. Audoin, "Temperature Dependence of the Hydrogen Maser Wall Shift in the Temperature Range 295-395 K," Metrologia **16**, 7–14 (1980).

[93] E. Roduner, P. W. Percival, P. Han, and D. M. Bartels, "Isotope and temperature effects on the hyperfine interaction of atomic hydrogen in liquid water and in ice," The Journal of Chemical Physics **102**, 5989–5997 (1995).

[94] S. B. Crampton, "Resonance studies of H atoms adsorbed on frozen H_2 surfaces," Le Journal de Physique Colloques **41**, C7–249–C7–255 (1980).

[95] D. R. Harshman, R. Keitel, M. Senba, R. F. Kiefl, E. J. Ansaldo, and J. H. Brewer, "Diffusion and trapping of muonium on silica surfaces," Physics Letters A **104**, 472–476 (1984).

[96] E. Shukrun Farrell, Y. Schilt, M. Y. Moshkovitz, Y. Levi-Kalisman, U. Raviv, and S. Magdassi, "3D Printing of Ordered Mesoporous Silica Complex Structures," Nano Letters **20**, 6598–6605 (2020).

[97] S. Zhao, G. Siqueira, S. Drdova, D. Norris, C. Ubert, A. Bonnin, S. Galmarini, M. Ganobjak, Z. Pan, S. Brunner, G. Nyström, J. Wang, M. M. Koebel, and W. J. Malfait, "Additive manufacturing of silica aerogels," Nature **584**, 387–392 (2020).

[98] E. S. Farrell, N. Ganonyan, I. Cooperstein, M. Y. Moshkovitz, Y. Amouyal, D. Avnir, and S. Magdassi, "3D-printing of ceramic aerogels by spatial photopolymerization," Applied Materials Today **24**, 101083 (2021).

[99] S. Seeger, K. H. Hoffmann, and C. Essex, "Random walks on random Koch curves," Journal of Physics A: Mathematical and Theoretical **42**, 225002 (2009).

[100] V. Vattipalli, X. Qi, P. J. Dauenhauer, and W. Fan, "Long Walks in Hierarchical Porous Materials due to Combined Surface and Configurational Diffusion," Chemistry of Materials **28**, 7852–7863 (2016).

[101] M. A. Sadeghi, M. Aghighi, J. Barralet, and J. T. Gostick, "Pore network modeling of reaction-diffusion in hierarchical porous particles: The effects of microstructure," Chemical Engineering Journal **330**, 1002–1011 (2017).

[102] I. Gurevich, I. Ivanter, L. Makariyna, E. Mel'eshko, B. Nikol'sky, V. Roganov, V. Selivanov, V. Smilga, B. Sokolov, V. Shestakov, and I. Jakovleva, "Muonium in magnetic field," Physics Letters B **29**, 387–390 (1969).

[103] I. I. Gurevich, I. G. Ivanter, E. A. Meleshko, B. A. Nikol'Skii, V. S. Roganov, V. I. Selivanov, V. P. Smilga, B. V. Sokolov, and V. D. Shestakov, "Two-frequency Precession of Muonium in a Magnetic Field," Soviet Physics JETP **33**, 253 (1971).

[104] J. H. Brewer, K. M. Crowe, F. N. Gygax, R. F. Johnson, B. D. Patterson, D. G. Fleming, and A. Schenck, "Anomalous $\mu+$ Precession in Silicon," Physical Review Letters **31**, 143–146 (1973).

[105] E. Holzschuh, H. Graf, E. Recknagel, A. Weidinger, T. Wichert, and P. F. Meier, "Muonium states in germanium," Physical Review B **20**, 4391–4396 (1979).

[106] E. Holzschuh, W. Kündig, P. F. Meier, B. D. Patterson, J. P. F. Sellschop, M. C. Stemmet, and H. Appel, "Muonium in diamond," Physical Review A **25**, 1272–1286 (1982).

[107] R. F. Kiefl, J. W. Schneider, H. Keller, W. Kündig, W. Odermatt, B. D. Patterson, K. W. Blazey, T. L. Estle, and S. L. Rudaz, "Muonium centers in GaAs and GaP," Physical Review B **32**, 530–532 (1985).

[108] J. H. Brewer, D. P. Spencer, D. G. Fleming, and J. A. R. Coope, "Muonium hyperfine matrix in quartz," Hyperfine Interactions **8**, 405–408 (1981).

[109] E. Holzschuh, W. Kündig, and B. D. Patterson, "Direct measurement of the muonium hyperfine frequencies in quartz," Helvetica Physica Acta **54**, 552 (1981).

[110] S. Cox and M. Symons, "Molecular radical models for the muonium centres in solids," Chemical Physics Letters **126**, 516–525 (1986).

[111] T. L. Estle, S. Estreicher, and D. S. Marynick, "Bond-centered hydrogen or muonium in diamond: The explanation for anomalous muonium and an example of metastability," Physical Review Letters **58**, 1547–1550 (1987).

[112] R. F. Kiefl, M. Celio, T. L. Estle, S. R. Kreitzman, G. M. Luke, T. M. Riseman, and E. J. Ansaldo, "Si^{29} Hyperfine Structure of Anomalous Muonium in Silicon: Proof of the Bond-Centered Model," Physical Review Letters **60**, 224–226 (1988).

[113] Y. Gorelkinskii and N. Nevinnyi, "Electron paramagnetic resonance of hydrogen in silicon," Physica B: Condensed Matter **170**, 155–167 (1991).

[114] B. Bech Nielsen, K. Bonde Nielsen, and J. Byberg, "EPR Experiments on Hydrogen-Implanted Silicon Crystals: Annealing Properties of Bond Center Hydrogen," Materials Science Forum **143–147**, 909–914 (1993).

[115] Y. V. Gorelkinskii, "Electron Paramagnetic Resonance Studies of Hydrogen and Hydrogen-Related Defects in Crystalline Silicon," in *Semiconductors and Semimetals*, Vol. 61 (Elsevier, 1999) pp. 25–81.

[116] S. R. Kreitzman, B. Hitti, R. L. Lichti, T. L. Estle, and K. H. Chow, "Muon-spin-resonance study of muonium dynamics in Si and its relevance to hydrogen," Physical Review B **51**, 13117–13137 (1995).

[117] B. D. Patterson, "Muonium states in semiconductors," Reviews of Modern Physics **60**, 69–159 (1988).

[118] C. G. Van de Walle, "Universal alignment of hydrogen levels in semiconductors and insulators," Physica B: Condensed Matter **376–377**, 1–6 (2006).

[119] C. G. Van de Walle, "Hydrogen as a Cause of Doping in Zinc Oxide," Physical Review Letters **85**, 1012–1015 (2000).

[120] S. F. J. Cox, E. A. Davis, S. P. Cottrell, P. J. C. King, J. S. Lord, J. M. Gil, H. V. Alberto, R. C. Vilão, J. Piroto Duarte, N. Ayres de Campos, A. Weidinger, R. L. Lichti, and S. J. C. Irvine, "Experimental Confirmation of the Predicted Shallow Donor Hydrogen State in Zinc Oxide," Physical Review Letters **86**, 2601–2604 (2001).

[121] D. M. Hofmann, A. Hofstaetter, F. Leiter, H. Zhou, F. Henecker, B. K. Meyer, S. B. Orlinskii, J. Schmidt, and P. G. Baranov, "Hydrogen: A Relevant Shallow Donor in Zinc Oxide," Physical Review Letters **88**, 045504 (2002).

[122] Ç. Kılıç and A. Zunger, "*N*-type doping of oxides by hydrogen," Applied Physics Letters **81**, 73–75 (2002).

[123] P. W. Peacock and J. Robertson, "Behavior of hydrogen in high dielectric constant oxide gate insulators," Applied Physics Letters **83**, 2025–2027 (2003).

[124] K. Xiong, J. Robertson, and S. J. Clark, "Behavior of hydrogen in wide band gap oxides," Journal of Applied Physics **102**, 083710 (2007).

[125] K. Shimomura and T. U. Ito, "Electronic Structure of Hydrogen Donors in Semiconductors and Insulators Probed by Muon Spin Rotation," Journal of the Physical Society of Japan **85**, 091013 (2016).

[126] T. Holstein, "Studies of polaron motion," Annals of Physics **8**, 325–342 (1959).

[127] D. Emin, "Small polarons," Physics Today **35**, 34–40 (1982).

[128] C. Franchini, M. Reticcioli, M. Setvin, and U. Diebold, "Polarons in materials," Nature Reviews Materials (2021), 10.1038/s41578-021-00289-w.

[129] F. Filippone, G. Mattioli, P. Alippi, and A. Amore Bonapasta, "Properties of hydrogen and hydrogen–vacancy complexes in the rutile phase of titanium dioxide," Physical Review B **80**, 245203 (2009).

[130] T. U. Ito, W. Higemoto, A. Koda, and K. Shimomura, "Polaronic nature of a muonium-related paramagnetic center in $SrTiO_3$," Applied Physics Letters **115**, 192103 (2019).

[131] R. B. L. Vieira, R. C. Vilão, A. G. Marinopoulos, P. M. Gordo, J. A. Paixão, H. V. Alberto, J. M. Gil, A. Weidinger, R. L. Lichti, B. Baker, P. W. Mengyan, and J. S. Lord, "Isolated hydrogen configurations in zirconia as seen by muon spin spectroscopy and *ab initio* calculations," Physical Review B **94**, 115207 (2016).

[132] R. F. Kiefl, M. Celio, T. L. Estle, G. M. Luke, S. R. Kreitzman, J. H. Brewer, D. R. Noakes, E. J. Ansaldo, and K. Nishiyama, "Determination of the electronic structure of anomalous muonium in GaAs from nuclear hyperfine interactions," Physical Review Letters **58**, 1780–1783 (1987).

[133] G. A. Samara and P. S. Peercy, "Pressure and Temperature Dependence of the Static Dielectric Constants and Raman Spectra of TiO_2 (Rutile)," Physical Review B **7**, 1131–1148 (1973).

[134] J. Bonkerud, C. Zimmermann, P. M. Weiser, L. Vines, and E. V. Monakhov, *On the Dielectric Constant of Titanium Dioxide*, Preprint (In Review, 2021).

[135] F. A. Grant, "Properties of Rutile (Titanium Dioxide)," Reviews of Modern Physics **31**, 646–674 (1959).

[136] K. Nakata and A. Fujishima, "TiO_2 photocatalysis: Design and applications," Journal of Photochemistry and Photobiology C: Photochemistry Reviews **13**, 169–189 (2012).

[137] M. Malati and W. Wong, "Doping TiO_2 for solar energy applications," Surface Technology **22**, 305–322 (1984).

[138] K. Hara, K. Sayama, H. Arakawa, Y. Ohga, A. Shinpo, and S. Suga, "A coumarin-derivative dye sensitized nanocrystalline TiO_2 solar cell having a high solar-energy conversion efficiency up to 5.6%," Chemical Communications , 569–570 (2001).

[139] M. V. Reddy, G. V. Subba Rao, and B. V. R. Chowdari, "Metal Oxides and Oxysalts as Anode Materials for Li Ion Batteries," Chemical Reviews **113**, 5364–5457 (2013).

[140] A. Chatzichristos, R. M. L. McFadden, M. H. Dehn, S. R. Dunsiger, D. Fujimoto, V. L. Karner, I. McKenzie, G. D. Morris, M. R. Pearson, M. Stachura, J. Sugiyama, J. O. Ticknor, W. A. MacFarlane, and R. F. Kiefl, "Bi-Arrhenius Diffusion and Surface Trapping of Li^+ 8 in Rutile TiO_2," Physical Review Letters **123**, 095901 (2019).

[141] V. N. Bogomolov and D. N. Mirlin, "Optical Absorption by Polarons in Rutile (TiO_2) Single Crystals," Physica Status Solidi (b) **27**, 443–453 (1968).

[142] I. G. Austin and N. F. Mott, "Polarons in crystalline and non-crystalline materials," Advances in Physics **50**, 757–812 (2001).

[143] N. Rahimi, R. Pax, and E. M. Gray, "Review of functional titanium oxides. II: Hydrogen-modified TiO_2," Progress in Solid State Chemistry **55**, 1–19 (2019).

[144] M. Aono and R. R. Hasiguti, "Interaction and ordering of lattice defects in oxygen-deficient rutile TiO_{2-x}," Physical Review B **48**, 12406–12414 (1993).

[145] F. Herklotz, E. V. Lavrov, and J. Weber, "Infrared absorption of the hydrogen donor in rutile TiO_2," Physical Review B **83**, 235202 (2011).

[146] F. Bekisli, W. B. Fowler, and M. Stavola, "Small polaron characteristics of an OD center in TiO_2 studied by infrared spectroscopy," Physical Review B **86**, 155208 (2012).

[147] L.-B. Mo, Y. Wang, Y. Bai, Q.-Y. Xiang, Q. Li, W.-Q. Yao, J.-O. Wang, K. Ibrahim, H.-H. Wang, C.-H. Wan, and J.-L. Cao, "Hydrogen Impurity Defects in Rutile TiO_2," Scientific Reports **5**, 17634 (2015).

[148] H. Sezen, M. Buchholz, A. Nefedov, C. Natzeck, S. Heissler, C. Di Valentin, and C. Wöll, "Probing electrons in TiO_2 polaronic trap states by IR-absorption: Evidence for the existence of hydrogenic states," Scientific Reports **4**, 3808 (2015).

[149] E. V. Lavrov, T. Mchedlidze, and F. Herklotz, "Photoconductive detection of hydrogen in ZnO and rutile TiO_2," Journal of Applied Physics **120**, 055703 (2016).

[150] A. Hupfer, L. Vines, E. V. Monakhov, B. G. Svensson, and F. Herklotz, "Photoinduced small polarons bound to hydrogen defects in rutile TiO_2," Physical Review B **96**, 085203 (2017).

[151] A. J. Hupfer, E. V. Monakhov, B. G. Svensson, I. Chaplygin, and E. V. Lavrov, "Hydrogen motion in rutile TiO_2," Scientific Reports **7** (2017), 10.1038/s41598-017-16660-3.

[152] C. Zimmermann, J. Bonkerud, F. Herklotz, T. N. Sky, A. Hupfer, E. Monakhov, B. G. Svensson, and L. Vines, "Influence of annealing atmosphere on formation of electrically-active defects in rutile TiO_2," Journal of Applied Physics **123**, 161572 (2018).

[153] P. M. Weiser, C. Zimmermann, J. Bonkerud, L. Vines, and E. V. Monakhov, "Donors and polaronic absorption in rutile TiO_2 single crystals," Journal of Applied Physics **128**, 145701 (2020).

[154] P. Deák, B. Aradi, and T. Frauenheim, "Quantitative theory of the oxygen vacancy and carrier self-trapping in bulk TiO_2," Physical Review B **86**, 195206 (2012).

[155] T. S. Bjørheim, A. Kuwabara, and T. Norby, "Defect Chemistry of Rutile TiO_2 from First Principles Calculations," The Journal of Physical Chemistry C **117**, 5919–5930 (2013).

[156] A. G. Marinopoulos, R. C. Vilão, H. V. Alberto, and J. M. Gil, "Electronic structure and migration of interstitial hydrogen in the rutile phase of TiO_2," Journal of Physics: Condensed Matter **30**, 425503 (2018).

[157] M. O. Atambo, D. Varsano, A. Ferretti, S. S. Ataei, M. J. Caldas, E. Molinari, and A. Selloni, "Electronic and optical properties of doped TiO_2 by many-body perturbation theory," Physical Review Materials **3**, 045401 (2019).

[158] X. Han, N. Amrane, Z. Zhang, and M. Benkraouda, "Insights into the Characteristic Gap Level and n-Type Conductivity of Rutile TiO_2 from the Hybrid Functional Method," The Journal of Physical Chemistry C **123**, 2037–2047 (2019).

[159] A. Baumann, *The Role of Oxygen Vacancies on Muon-Polaron Complexes in TiO_2 from First Principles*, MSc thesis, ETH Zurich (2020).

[160] A. Janotti, C. Franchini, J. B. Varley, G. Kresse, and C. G. Van de Walle, "Dual behavior of excess electrons in rutile TiO_2," physica status solidi (RRL) - Rapid Research Letters **7**, 199–203 (2013).

[161] A. R. Elmaslmane, M. B. Watkins, and K. P. McKenna, "First-Principles Modeling of Polaron Formation in TiO_2 Polymorphs," Journal of Chemical Theory and Computation **14**, 3740–3751 (2018).

[162] S. Yang and L. E. Halliburton, "Fluorine donors and Ti^{3+} ions in TiO_2 crystals," Physical Review B **81**, 035204 (2010).

[163] A. T. Brant, N. C. Giles, M. A. R. Sarker, S. Watauchi, M. Nagao, I. Tanaka, D. A. Tryk, A. Manivannan, and L. E. Halliburton, "Ground state of the singly ionized oxygen vacancy in rutile TiO_2," Journal of Applied Physics **114**, 113702 (2013).

[164] A. T. Brant, E. M. Golden, N. C. Giles, S. Yang, M. A. R. Sarker, S. Watauchi, M. Nagao, I. Tanaka, D. A. Tryk, A. Manivannan, and L. E. Halliburton, "Triplet ground state of the neutral oxygen-vacancy donor in rutile TiO_2," Physical Review B **89**, 115206 (2014).

[165] C. W. M. Castleton, A. Lee, and J. Kullgren, "Benchmarking Density Functional Theory Functionals for Polarons in Oxides: Properties of CeO_2," The Journal of Physical Chemistry C **123**, 5164–5175 (2019).

[166] M. Kick, K. Reuter, and H. Oberhofer, "Intricacies of DFT+U, Not Only in a Numeric Atom Centered Orbital Framework," Journal of Chemical Theory and Computation **15**, 1705–1718 (2019).

[167] Z. Wang, C. Brock, A. Matt, and K. H. Bevan, "Implications of the DFT+U method on polaron properties in energy materials," Physical Review B **96**, 125150 (2017).

[168] A. M. Browne and A. M. Stoneham, "Impurity trapping effects in the localisation of muons in solids," Journal of Physics C: Solid State Physics **15**, 2709–2720 (1982).

[169] A. M. Stoneham, "Kinetics and dynamics of muon localisation and trapping," Hyperfine Interactions **17**, 53–62 (1984).

[170] K. Rüegg, C. Boekema, W. Hofmann, W. Kündig, and P. F. Meier, "μSR in antiferromagnetic Cr_2O_3 and α-Fe_2O_3," Hyperfine Interactions **6**, 99–101 (1979).

[171] K. Rüegg, C. Boekema, A. Denison, W. Hoffmann, and W. Kündig, "Muon spin rotation experiments in α-Fe_2O_3 and Cr_2O_3," Journal of Magnetism and Magnetic Materials **15–18**, 669 (1980).

[172] H. Graf, W. Hofmann, W. Kündig, P. F. Meier, B. D. Patterson, and A. Rodriguez, "μSR in antiferromagnetic α-Fe_2O_3," Solid State Communications **25**, 1079–1081 (1978).

[173] H. A. Jahn and E. Teller, "Stability of polyatomic molecules in degenerate electronic states - I—Orbital degeneracy," Proc. Roy. Soc. A **161**, 16 (1937).

[174] H. Nickisch, H. Thomas, and K.-H. Höck, "Jahn-Teller effect in ititnerant electron systems: The Jahn-Teller polaron," Helvetica Physica Acta **56**, 237–243 (1983).

[175] C. Boekema, K. Rüegg, and W. P. Hofmann, "Interpretation of the muon hyperfine interactions in α-Fe_2O_3 and Cr_2O_3," Hyperfine interactions **8**, 609–613 (1981).

[176] C. Boekema, A. B. Denison, and K. J. Rüegg, "Muon spin rotation in antiferromagnetic oxides," Journal of Magnetism and Magnetic Materials **36**, 111–114 (1983).

[177] M. H. Dehn, J. K. Shenton, S. Holenstein, Q. N. Meier, D. J. Arseneau, D. L. Cortie, B. Hitti, A. C. Y. Fang, W. A. MacFarlane, R. M. L. McFadden, G. D. Morris, Z. Salman, H. Luetkens, N. A. Spaldin, M. Fechner, and R. F. Kiefl, "Observation of a Charge-Neutral Muon-Polaron Complex in Antiferromagnetic Cr_2O_3," Physical Review X **10**, 011036 (2020).

[178] A. B. Denison, "Muon spin rotation in magnetic oxides (invited)," Journal of Applied Physics **55**, 2278–2283 (1984).

[179] E. Holzschuh, A. B. Denison, W. Kündig, P. F. Meier, and B. D. Patterson, "Muon-spin-rotation experiments in orthoferrites," Physical Review B **27**, 5294–5307 (1983).

[180] H. Wiegelmann, A. Jansen, J.-P. Rivera, H. Schmid, A. Stepanov, and I. Vitebsky, "Magnetoelectric studies of antiferromagnetic crystals in strong magnetic fields," Physica B: Condensed Matter **204**, 292–297 (1995).

[181] E. Samuelsen, M. Hutchings, and G. Shirane, "Inelastic neutron scattering investigation of spin waves and magnetic interactions in Cr_2O_3," Physica **48**, 13–42 (1970).

[182] K. Momma and F. Izumi, "*VESTA 3* for three-dimensional visualization of crystal, volumetric and morphology data," Journal of Applied Crystallography **44**, 1272–1276 (2011).

[183] A. G. Redfield, "On the Theory of Relaxation Processes," IBM Journal of Research and Development **1**, 19–31 (1957).

[184] V. N. Duginov, V. G. Grebinnik, K. I. Gritsaj, T. N. Mamedov, V. G. Olshevsky, V. Y. Pomjakushin, V. A. Zhukov, B. F. Kirillov, I. A. Krivosheev, A. V. Pirogov, and A. N. Ponomarev, "μSR investigation of cupric oxide," Hyperfine Interactions **85**, 317–322 (1994).

[185] A. Amato, D. Andreica, F. Gygax, M. Pinkpank, N. Sato, A. Schenck, and G. Solt, "Muon tunneling along a ring-shaped orbit in UNi_2Al_3," Physica B: Condensed Matter **289–290**, 447–450 (2000).

[186] A. M. Mulders, P. C. M. Gubbens, C. Kaiser, A. Amato, F. Gygax, A. Schenck, P. Dalmas de Réotier, A. Yaouanc, K. Buschow, F. Kayzel, and A. Menovsky, "Muon Spin Dynamics and Sites in $GdNi_5$," Hyperfine Interactions **133**, 197–201 (2001).

[187] J. W. Schneider, R. F. Kiefl, K. Chow, S. F. J. Cox, S. A. Dodds, R. C. DuVarney, T. L. Estle, R. Kadono, S. R. Kreitzman, R. L. Lichti, and C. Schwab, "Local tunneling and metastability of muonium in CuCl," Physical Review Letters **68**, 3196–3199 (1992).

[188] P. Bonfà and R. De Renzi, "Toward the computational prediction of muon sites and interaction parameters," Journal of the Physical Society of Japan **85**, 091014 (2016).

[189] I. J. Onuorah, P. Bonfà, and R. De Renzi, "Muon contact hyperfine field in metals: A DFT calculation," Physical Review B **97**, 174414 (2018).

[190] I. J. Onuorah, P. Bonfà, R. De Renzi, L. Monacelli, F. Mauri, M. Calandra, and I. Errea, "Quantum effects in muon spin spectroscopy within the stochastic self-consistent harmonic approximation," Physical Review Materials **3**, 073804 (2019).

[191] G. Kresse and J. Hafner, "*Ab Initio* molecular dynamics for liquid metals," Physical Review B **47**, 558–561 (1993).

[192] G. Kresse and J. Hafner, "*Ab Initio* molecular-dynamics simulation of the liquid-metal–amorphous-semiconductor transition in germanium," Physical Review B **49**, 14251–14269 (1994).

[193] G. Kresse and J. Furthmüller, "Efficient iterative schemes for *ab initio* total-energy calculations using a plane-wave basis set," Physical Review B **54**, 11169–11186 (1996).

[194] M. R. MacDonald, J. E. Bates, J. W. Ziller, F. Furche, and W. J. Evans, "Completing the Series of +2 Ions for the Lanthanide Elements: Synthesis of Molecular Complexes of Pr^{2+} , Gd^{2+} , Tb^{2+} , and Lu^{2+}," Journal of the American Chemical Society **135**, 9857–9868 (2013).

[195] R. H. Heffner, J. E. Sonier, D. E. MacLaughlin, G. J. Nieuwenhuys, G. M. Luke, Y. J. Uemura, W. Ratcliff, S.-W. Cheong, and G. Balakrishnan, "Muon spin relaxation study of $La_{1-x}Ca_xMnO_3$," Physical Review B **63**, 094408 (2001).

[196] K. Nishiyama, W. Higemoto, K. Shimomura, A. Koda, G. Maruta, S. W. Nishiyama, and X. G. Zheng, "Multiple Phase Transitions in CuO Studied by μSR," Hyperfine Interactions **136/137**, 289–294 (2001).

[197] M. Bimbi, G. Allodi, R. De Renzi, C. Mazzoli, and H. Berger, "Muon spin spectroscopy evidence of a charge density wave in magnetite below the Verwey transition," Physical Review B **77**, 045115 (2008).

[198] M. C. Guidi, G. Allodi, R. D. Renzi, G. Guidi, M. Hennion, L. Pinsard, and A. Amato, "Staggered magnetization, critical behavior, and weak ferromagnetic properties of $LaMnO_3$ by muon spin rotation," Physical Review B **64**, 064414 (2001).

[199] V. G. Storchak, O. E. Parfenov, J. H. Brewer, P. L. Russo, S. L. Stubbs, R. L. Lichti, D. G. Eshchenko, E. Morenzoni, T. G. Aminov, V. P. Zlomanov, A. A. Vinokurov, R. L. Kallaher, and S. von Molnár, "Direct observation of the magnetic polaron," Physical Review B **80**, 235203 (2009).

[200] V. G. Storchak, J. H. Brewer, R. L. Lichti, T. A. Lograsso, and D. L. Schlagel, "Electron localization into spin-polaron state in MnSi," Physical Review B **83**, 140404(R) (2011).

[201] R. F. Kiefl, "Comment on "Direct observation of the magnetic polaron"," Physical Review B **83**, 077201 (2011).

[202] A. Amato, P. Dalmas de Reotier, D. Andreica, A. Yaouanc, A. Suter, G. Lapertot, I. M. Pop, E. Morenzoni, P. Bonfà, F. Bernardini, and R. De Renzi, "Understanding the μSR spectra of MnSi without magnetic polarons," Physical Review B **89**, 184425 (2014).

[203] J. H. Brewer, V. G. Storchak, G. D. Morris, and D. Eshchenko, "Comment on "Role of the transition state in muon implantation" and "Thermal spike in muon implantation"," Physical Review B **101**, 077201 (2020).

[204] R. C. Vilão, H. V. Alberto, R. B. L. Vieira, J. M. Gil, and A. Weidinger, "Reply to "Comment on 'Role of the transition state in muon implantation' and 'Thermal spike in muon implantation'"," Physical Review B **101**, 077202 (2020).

[205] T. Jungwirth, X. Marti, P. Wadley, and J. Wunderlich, "Antiferromagnetic spintronics," Nature Nanotechnology **11**, 231–241 (2016).

[206] T. Jungwirth, J. Sinova, A. Manchon, X. Marti, J. Wunderlich, and C. Felser, "The multiple directions of antiferromagnetic spintronics," Nature Physics **14**, 200–203 (2018).

[207] V. Baltz, A. Manchon, M. Tsoi, T. Moriyama, T. Ono, and Y. Tserkovnyak, "Antiferromagnetic spintronics," Reviews of Modern Physics **90**, 015005 (2018).

[208] W. Yuan, J. Li, and J. Shi, "Spin current generation and detection in uniaxial antiferromagnetic insulators," Applied Physics Letters **117**, 100501 (2020).

[209] H. Bai, X. Zhou, Y. Zhou, X. Chen, Y. You, F. Pan, and C. Song, "Functional antiferromagnets for potential applications on high-density storage and high frequency," Applied Physics , 11 (2020).

[210] T. Dietl and H. Ohno, "Dilute ferromagnetic semiconductors: Physics and spintronic structures," Reviews of Modern Physics **86**, 187–251 (2014).

[211] N. A. Spaldin and R. Ramesh, "Advances in magnetoelectric multiferroics," Nature Materials **18**, 203–212 (2019).

[212] W. E. Pickett, "Electronic structure of the high-temperature oxide superconductors," Reviews of Modern Physics **61**, 433–512 (1989).

[213] F. J. Morin, "Magnetic Susceptibility of αFe_2O_3 and αFe_2O_3 with Added Titanium," Physical Review **78**, 819–820 (1950).

[214] C. G. Shull, W. A. Strauser, and E. O. Wollan, "Neutron Diffraction by Paramagnetic and Antiferromagnetic Substances," Physical Review **83**, 333–345 (1951).

[215] F. P. Chmiel, N. Waterfield Price, R. D. Johnson, A. D. Lamirand, J. Schad, G. van der Laan, D. T. Harris, J. Irwin, M. S. Rzchowski, C.-B. Eom, and P. G. Radaelli, "Observation of magnetic vortex pairs at room temperature in a planar α-Fe_2O_3/Co heterostructure," Nature Materials **17**, 581–585 (2018).

[216] D. L. Cortie, T. Buck, M. H. Dehn, V. L. Karner, R. F. Kiefl, C. D. P. Levy, R. M. L. McFadden, G. D. Morris, I. McKenzie, M. R. Pearson, X. L. Wang, and W. A. MacFarlane, "β-NMR Investigation of the Depth-Dependent Magnetic Properties of an Antiferromagnetic Surface," Physical Review Letters **116**, 106103 (2016).

[217] A. Sanson, I. Kantor, V. Cerantola, T. Irifune, A. Carnera, and S. Pascarelli, "Local structure and spin transition in Fe_2O_3 hematite at high pressure," Physical Review B **94**, 014112 (2016).

[218] S. Xu, A. H. Habib, S. H. Gee, Y. K. Hong, and M. E. McHenry, "Spin orientation, structure, morphology, and magnetic properties of hematite nanoparticles," Journal of Applied Physics **117**, 17A315 (2015).

[219] K. J. Rüegg, C. Boekema, W. Kündig, P. F. Meier, and B. O. Patterson, "Muon diffusion in α-Fe_2O_3," Hyper fine Interactions **8**, 547 (1981).

[220] K. B. Chan, *Localization and Local Motion of Muons in Antiferromagnetic Oxides: Vanadium Oxide and Iron Oxide*, MSc thesis, Texas Tech University (1986).

[221] K. C. Chan, *Muon Sites in Transition Metal Oxides*, Ph.D. thesis, Texas Tech University (1988).

[222] S. Lany, "Semiconducting transition metal oxides," Journal of Physics: Condensed Matter **27**, 283203 (2015).

[223] D. A. Grave, N. Yatom, D. S. Ellis, M. C. Toroker, and A. Rothschild, "The "Rust" Challenge: On the Correlations between Electronic Structure, Excited State Dynamics, and Photoelectrochemical Performance of Hematite Photoanodes for Solar Water Splitting," Advanced Materials **30**, 1706577 (2018).

[224] J. Zhang and S. Eslava, "Understanding charge transfer, defects and surface states at hematite photoanodes," Sustainable Energy & Fuels **3**, 1351–1364 (2019).

[225] E. Pastor, J.-S. Park, L. Steier, S. Kim, M. Grätzel, J. R. Durrant, A. Walsh, and A. A. Bakulin, "In situ observation of picosecond polaron self-localisation in α-Fe_2O_3 photoelectrochemical cells," Nature Communications **10**, 3962 (2019).

[226] L. M. Carneiro, S. K. Cushing, C. Liu, Y. Su, P. Yang, A. P. Alivisatos, and S. R. Leone, "Excitation-wavelength-dependent small polaron trapping of photoexcited carriers in α-Fe_2O_3," Nature Materials **16**, 819–825 (2017).

[227] J. Husek, A. Cirri, S. Biswas, and L. R. Baker, "Surface electron dynamics in hematite (α-Fe_2O_3): Correlation between ultrafast surface electron trapping and small polaron formation," Chemical Science **8**, 8170–8178 (2017).

[228] A. Kay, M. Fiegenbaum-Raz, S. Müller, R. Eichberger, H. Dotan, R. de Krol, F. F. Abdi, A. Rothschild, D. Friedrich, and D. A. Grave, "Effect of Doping and Excitation Wavelength on Charge Carrier Dynamics in Hematite by Time-Resolved Microwave and Terahertz Photoconductivity," Advanced Functional Materials , 1901590 (2019).

[229] K. M. Rosso, D. M. A. Smith, and M. Dupuis, "An *ab initio* model of electron transport in hematite (α-Fe_2O_3) basal planes," The Journal of Chemical Physics **118**, 6455–6466 (2003).

[230] N. Iordanova, M. Dupuis, and K. M. Rosso, "Charge transport in metal oxides: A theoretical study of hematite α-Fe_2O_3," The Journal of Chemical Physics **122**, 144305 (2005).

[231] J. Lee and S. Han, "Thermodynamics of native point defects in α-Fe_2O_3: An ab initio study," Physical Chemistry Chemical Physics **15**, 18906 (2013).

[232] A. J. E. Rettie, W. D. Chemelewski, D. Emin, and C. B. Mullins, "Unravelling Small-Polaron Transport in Metal Oxide Photoelectrodes," The Journal of Physical Chemistry Letters **7**, 471–479 (2016).

[233] A. J. E. Rettie, W. D. Chemelewski, B. R. Wygant, J. Lindemuth, J.-F. Lin, D. Eisenberg, C. S. Brauer, T. J. Johnson, T. N. Beiswenger, R. D. Ash, X. Li, J. Zhou, and C. B. Mullins, "Synthesis, electronic transport and optical properties of Si:α-Fe_2O_3 single crystals," Journal of Materials Chemistry C **4**, 559–567 (2016).

[234] B. Zhao, T. C. Kaspar, T. C. Droubay, J. McCloy, M. E. Bowden, V. Shutthanandan, S. M. Heald, and S. A. Chambers, "Electrical transport properties of Ti-doped Fe_2O_3 (0001) epitaxial films," Physical Review B **84**, 245325 (2011).

[235] T. J. Smart and Y. Ping, "Effect of defects on the small polaron formation and transport properties of hematite from first-principles calculations," Journal of Physics: Condensed Matter **29**, 394006 (2017).

[236] M. H. Dehn, J. K. Shenton, D. J. Arseneau, W. A. MacFarlane, G. D. Morris, A. Maigné, N. A. Spaldin, and R. F. Kiefl, "Local Electronic Structure and Dynamics of Muon-Polaron Complexes in Fe_2O_3," Physical Review Letters **126**, 037202 (2021).

[237] F. van der Woude, "Mössbauer Effect in α-Fe_2O_3," Physica Status Solidi (b) **17**, 417–432 (1966).

[238] P. F. Meier, "Spin dynamics of transitions between muon states," Physical Review A **25**, 1287–1294 (1982).

[239] G. Kresse and D. Joubert, "From ultrasoft pseudopotentials to the projector augmented-wave method," Physical Review B **59**, 1758–1775 (1999).

[240] D. Emin and N. L. H. Liu, "Small-polaron hopping in magnetic semiconductors," Physical Review B **27**, 4788–4798 (1983).

[241] L. J. De Jongh and A. R. Miedema, "Experiments on simple magnetic model systems," Advances in Physics **50**, 947–1170 (2001).

[242] Z. Yamani, Z. Tun, and D. H. Ryan, "Neutron scattering study of the classical antiferromagnet MnF_2: A perfect hands-on neutron scattering teaching course: Special issue on Neutron Scattering in Canada." Canadian Journal of Physics **88**, 771–797 (2010).

[243] M. Griffel and J. W. Stout, "Preparation of Single Crystals of Manganous Fluoride. The Crystal Structure from X-Ray Diffraction. The Melting Point and Density," Journal of the American Chemical Society **72**, 4351–4353 (1950).

[244] R. A. Erickson, "Neutron Diffraction Studies of Antiferromagnetism in Manganous Fluoride and Some Isomorphous Compounds," Physical Review **90**, 779–785 (1953).

[245] T. Higuchi and M. Kuwata-Gonokami, "Control of antiferromagnetic domain distribution via polarization-dependent optical annealing," Nature Communications **7**, 10720 (2016).

[246] P. Vaidya, S. A. Morley, J. van Tol, Y. Liu, R. Cheng, A. Brataas, D. Lederman, and E. del Barco, "Subterahertz spin pumping from an insulating antiferromagnet," Science **368**, 160–165 (2020).

[247] L.-D. Yuan, Z. Wang, J.-W. Luo, E. I. Rashba, and A. Zunger, "Giant momentum-dependent spin splitting in centrosymmetric low- Z antiferromagnets," Physical Review B **102**, 014422 (2020).

[248] S. A. Egorov and R. A. Evarestov, "Colossal Spin Splitting in the Monolayer of the Collinear Antiferromagnet MnF_2," J. Phys. Chem. Lett. **12**, 2363 (2021).

[249] S. M. Wu, W. Zhang, A. Kc, P. Borisov, J. E. Pearson, J. S. Jiang, D. Lederman, A. Hoffmann, and A. Bhattacharya, "Antiferromagnetic Spin Seebeck Effect," Physical Review Letters **116**, 097204 (2016).

[250] Ø. Johansen and A. Brataas, "Spin pumping and inverse spin Hall voltages from dynamical antiferromagnets," Physical Review B **95**, 220408 (2017).

[251] R. de Renzi, G. Guidi, P. Podini, R. Tedeschi, C. Bucci, and S. F. J. Cox, "Magnetic properties of MnF_2 and CoF_2 determined by implanted positive muons. II. Sublattice magnetization and phase transition," Physical Review B **30**, 197–204 (1984).

[252] R. De Renzi, G. Guidi, P. Podini, R. Tedeschi, C. Bucci, and S. F. J. Cox, "Magnetic properties of MnF_2 and CoF_2 determined by implanted positive muons. I. Localization studies," Physical Review B **30**, 186–196 (1984).

[253] R. F. Kiefl, G. M. Luke, S. R. Kreitzman, M. Celio, R. Keitel, J. H. Brewer, D. R. Noakes, Y. J. Uemura, A. M. Portis, and V. Jaccarino, "Muon level-crossing resonance in antiferromagnetic MnF_2," Physical Review B **35**, 2079–2082 (1987).

[254] A. Keren, "Dynamic spin relaxation processes of μ^+ in an antiferromagnet," Hyperfine Interactions **85**, 281–286 (1994).

[255] A. Keren, L. P. Le, G. M. Luke, W. D. Wu, and Y. J. Uemura, "Explaining μ^+ spin-lattice relaxation in MnF_2, below T_N, by scattering function," Hyperfine Interactions **85**, 363–368 (1994).

[256] J. S. Möller, D. Ceresoli, T. Lancaster, N. Marzari, and S. J. Blundell, "Quantum states of muons in fluorides," Physical Review B **87**, 121108 (2013).

[257] W. Jauch, M. Reehuis, and A. J. Schultz, "γ-ray and neutron diffraction studies of CoF_2 : Magnetostriction, electron density and magnetic moments," Acta Crystallographica Section A: Foundations of Crystallography **60**, 51–57 (2004).

[258] J. Strempfer, U. Rütt, S. P. Bayrakci, T. Brückel, and W. Jauch, "Magnetic properties of transition metal fluorides MF_2 (M = Mn , Fe, Co, Ni) via high-energy photon diffraction," Physical Review B **69**, 014417 (2004).

[259] R. F. Kiefl, E. Holzschuh, H. Keller, W. Kündig, P. F. Meier, B. D. Patterson, J. W. Schneider, K. W. Blazey, S. L. Rudaz, and A. B. Denison, "Decoupling of muonium in high transverse magnetic fields," Physical review letters **53**, 90 (1984).

[260] N. Kaplan, R. Loudon, V. Jaccarino, H. J. Guggenheim, D. Beeman, and P. A. Pincus, "Nuclear Spin-Lattice Relaxation of F^{19} in Antiferromagnetic MnF_2," Physical Review Letters **17**, 357–360 (1966).

[261] S. P. Bayrakci, "Spin-Wave Lifetimes Throughout the Brillouin Zone," Science **312**, 1926–1929 (2006).

[262] G. K. Wertheim, H. J. Guggenheim, and D. N. E. Buchanan, "Magnetization of Impurity Fe^{2+} Ions in MnF_2 and CoF_2," Journal of Applied Physics **40**, 1319–1321 (1969).

[263] A. Oseroff and P. S. Pershan, "Raman Scattering from Localized Magnetic Excitations in Ni^{2+} - and Fe^{2+} - Doped MnF_2," Physical Review Letters **21**, 1593–1596 (1968).

[264] O. de Alcantara Bonfim and M. Engelsberg, "Temperature dependence of magnon pair-mode energies in MnF_2:fe^{++}," Solid State Communications **21**, 175–177 (1977).

[265] H. Jani, J. Linghu, S. Hooda, R. V. Chopdekar, C. Li, G. J. Omar, S. Prakash, Y. Du, P. Yang, A. Banas, K. Banas, S. Ghosh, S. Ojha, G. R. Umapathy, D. Kanjilal, A. Ariando, S. J. Pennycook, E. Arenholz, P. G. Radaelli, J. M. D. Coey, Y. P. Feng, and T. Venkatesan, "Reversible hydrogen control of antiferromagnetic anisotropy in α-Fe_2O_3," Nature Communications **12**, 1668 (2021).

[266] J. H. Brewer, S. R. Kreitzman, D. R. Noakes, E. J. Ansaldo, D. R. Harshman, and R. Keitel, "Observation of muon-fluorine "hydrogen bonding" in ionic crystals," Physical Review B **33**, 7813–7816 (1986).

[267] D. Noakes, E. Ansaldo, S. Kreitzman, and G. Luke, "The (FμF)- ion in solid fluorides," Journal of Physics and Chemistry of Solids **54**, 785–792 (1993).

[268] R. G. Shulman and V. Jaccarino, "Nuclear Magnetic Resonance in Paramagnetic MnF_2," Physical Review **108**, 1219–1231 (1957).

[269] P. Heller and G. B. Benedek, "Nuclear Magnetic Resonance in MnF_2 Near the Critical Point," Physical Review Letters **8**, 428–432 (1962).

[270] G. G. Low, A. Okazaki, R. W. H. Stevenson, and K. C. Turberfield, "A Measurement of Spin-Wave Dispersion in MnF_2 at 4.2 K," Journal of Applied Physics **35**, 998–999 (1964).

[271] A. Sidorenko, G. Allodi, M. Cestelli Guidi, and R. De Renzi, "Comparison of NMR, μSR and neutron diffraction in $LaMnO_3$," Journal of Magnetism and Magnetic Materials **272–276**, 108–109 (2004).

[272] N. Nishida, K. Nagamine, R. S. Hayano, T. Yamazaki, D. G. Fleming, R. A. Duncan, J. H. Brewer, A. Ahktar, and H. Yasuoka, "The Local Magnetic Fields Probed by μ^+ in hcp Ferromagnets: Co and Gd," Journal of the Physical Society of Japan **44**, 1131–1141 (1978).

[273] F. R. Foronda, F. Lang, J. S. Möller, T. Lancaster, A. T. Boothroyd, F. L. Pratt, S. R. Giblin, D. Prabhakaran, and S. J. Blundell, "Anisotropic Local Modification of Crystal Field Levels in Pr-Based Pyrochlores: A Muon-Induced Effect Modeled Using Density Functional Theory," Physical Review Letters **114** (2015).

[274] C. H. Park and D. J. Chadi, "Hydrogen-Mediated Spin-Spin Interaction in ZnCoO," Physical Review Letters **94**, 127204 (2005).

[275] O. V. Yazyev and L. Helm, "Defect-induced magnetism in graphene," Physical Review B **75**, 125408 (2007).

[276] D. W. Boukhvalov, M. I. Katsnelson, and A. I. Lichtenstein, "Hydrogen on graphene: Electronic structure, total energy, structural distortions and magnetism from first-principles calculations," Physical Review B **77**, 035427 (2008).

[277] J. K. Park, K. W. Lee, S. Noh, H. Kim, and C. E. Lee, "Hydrogen shallow donors in Co-doped ZnO showing room-temperature ferromagnetism," Current Applied Physics **14**, 206–208 (2014).

[278] L. Hu, L. Zhu, H. He, and Z. Ye, "Unexpected magnetization enhancement in hydrogen plasma treated ferromagnetic (Zn,Cu)O film," Applied Physics Letters **105**, 072414 (2014).

[279] A. J. Tan, M. Huang, C. O. Avci, F. Büttner, M. Mann, W. Hu, C. Mazzoli, S. Wilkins, H. L. Tuller, and G. S. D. Beach, "Magneto-ionic control of magnetism using a solid-state proton pump," Nature Materials **18**, 35–41 (2019).

[280] T. Chatterji and T. C. Hansen, "Magnetoelastic effects in Jahn–Teller distorted CrF_2 and CuF_2 studied by neutron powder diffraction," Journal of Physics: Condensed Matter **23**, 276007 (2011).

[281] W. H. Sio, C. Verdi, S. Poncé, and F. Giustino, "Polarons from First Principles, without Supercells," Physical Review Letters **122**, 246403 (2019).

[282] T. D. Pham and N. A. Deskins, "Efficient Method for Modeling Polarons Using Electronic Structure Methods," Journal of Chemical Theory and Computation **16**, 5264–5278 (2020).

[283] M. Imada, A. Fujimori, and Y. Tokura, "Metal-insulator transitions," Rev. Mod. Phys. **70**, 225 (1998).

[284] P. F. Meier, "Spin dynamics of transitions between muon states," Physical Review A **25**, 1287 (1982).

Appendix A

Details on the Cr_2O_3 analysis

A.1 Orientation of the internal magnetic field

Under the assumption that $\mathbf{B}_{ext}$ does not induce changes of $\mathbf{B}_{int}$, the resulting frequency multiplets can be calculated by simple vector addition. For $\mathbf{B}_{ext}||c$, only θ is relevant, and we expect the ZF frequency f^{ZF} to be split into a doublet, see Fig. 5.3(a), with the frequencies $f^{\pm}$ given by

$$f^{\pm} = \left[\left(f_{ext} \pm f^{\mathrm{ZF}} \sin(\theta) \right)^2 + \left(f^{\mathrm{ZF}} \cos(\theta) \right)^2 \right]^{1/2}, \tag{A.1}$$

where $f_{ext} = \gamma_\mu/(2\pi) \cdot |\mathbf{B}_{ext}|$. Given the equal number of sites with $+\theta$ and $-\theta$, equal amplitudes for both doublet lines are expected (for $\mathbf{B}_{ext} \ll \mathbf{B}_{int}$).

For $\mathbf{B}_{ext}||[11\bar{2}0]\perp c$, the multiplet splitting, determined by both φ and θ, is given by

$$\begin{aligned} f(\theta,\varphi) = \Big[& (f^{\mathrm{ZF}} \sin(\theta))^2 + (f^{\mathrm{ZF}} \sin(\varphi)\cos(\theta))^2 \\ & + (f_{ext} + f^{\mathrm{ZF}} \cos(\varphi)\cos(\theta))^2 \Big]^{1/2} \end{aligned} \tag{A.2}$$

Only for $\delta = 0$ or $\pm 30°$, $\mathbf{B}_{ext}$ causes a multiplet splitting with less than six lines, but yields either a quadruplet for $\delta = 0$ or a triplet for $\delta = \pm 30°$, with an amplitude ratio of 1:2:2:1 and 2:2:2, respectively, see Figs. 5.3(b) and (c).

For $\mathbf{B}_{ext} \parallel c$, Eqn. (A.1) is used to calculate the expected doublet frequencies (f_{calc}) with f^{ZF} from Fig. 5.1(c). Minimizing $|f_{calc}(\theta) - f_{exp}(\theta)| + |f_{calc}(-\theta) - f_{exp}(-\theta)|$ yields θ values that produce excellent agreement between f_{calc} and f_{exp} for E1-E3, see Table A.1.

Using those θ values, Eqn. (A.2) is used to investigate the $\mathbf{B}_{ext} \parallel [11\bar{2}0]\perp c$ multiplet splittings. For E1 and E2, the measured frequencies are in very good agreement with the calculated values f_{calc} for $\delta = 0$ and 30°, respectively, see Table A.2. Furthermore, the amplitudes are close to the predicted 1:2:2:1 and 2:2:2 ratio. For E3, $\delta = \pm 17.5°$ yields a reasonable agreement between f_{calc} and f_{exp}, assuming that the outer two lines on either sides of the resulting sextet are not resolved, but appear at

Table A.1: Comparison of frequencies f_{exp} measured at 2.55 K in C2, 30 mT$||c$, and calculated values f_{calc}, obtained with Eqn. (A.1) using f^{ZF} from Fig. 5.1(c) and by optimizing θ to minimize $|f_{calc}(\theta) - f_{exp}(\theta)| + |f_{calc}(-\theta) - f_{exp}(-\theta)|$.

site	f^{ZF} [MHz]	f_{exp} [MHz]	f_{calc} [MHz]	θ [°]
E1	68.53 ± 0.01	66.98 ± 0.01	66.98	-24.0
		70.28 ± 0.01	70.28	+24.0
E2	102.12 ± 0.01	101.78 ± 0.01	101.78	-6.0
		102.62 ± 0.01	102.63	+6.0
E3	76.71 ± 0.01	76.46 ± 0.03	76.46	-5.0
		77.18 ± 0.04	77.17	+5.0

Table A.2: Comparison of frequencies f_{exp} measured at 2.2 K in C1, 20 mT$\perp c$, and calculated values f_{calc}, obtained with Eqn. (A.2) using f^{ZF} from Fig. 5.1(c), θ from Table A.1, φ given by $0° + \delta, \pm 60° + \delta, \pm 120° + \delta$ and $180° + \delta$ with $\delta = 0°$ for E1, $\delta = 30°$ for E2 and $\delta = 17.5°$ for E3. Bold values correspond to the average of vertically adjacent values.

site	f^{ZF} [MHz]	θ [°]	f_{exp} [MHz]	f_{calc} [MHz]	φ_{calc} [°]
E1	68.52 ± 0.01	24	66.08 ± 0.03	66.05	180
			67.38 ± 0.01	67.32	± 120
			69.76 ± 0.01	69.80	± 60
			71.00 ± 0.03	71.00	0
E2	102.12 ± 0.01	6	99.80 ± 0.01	99.79	± 150
			102.16 ± 0.01	102.15	± 90
			104.45 ± 0.01	104.46	± 30
E3	76.69 ± 0.01	5		74.11	$+162.5$
			74.51 ± 0.07	**74.42**	–
				74.72	-137.5
			76.15 ± 0.09	76.15	$+102.5$
			77.25 ± 0.07	77.32	-77.5
				78.70	$+42.5$
			78.89 ± 0.05	**78.98**	–
				79.27	-17.5

their average frequency (shown in bold in Table A.2) with twice the amplitude. From that, an amplitude ratio of 2:1:1:2 is expected, which is indeed observed. Considering crystal alignment and the observed frequencies and amplitude ratios, we estimate the uncertainties to be $\pm 1°$ for all θ values, $\pm 3.5°$ for δ_{E1} and δ_{E2}, and $\pm 2°$ for δ_{E3}.

Table A.3: Comparison of frequencies f_{exp} measured at $T = 2.1\,\mathrm{K}$, $\mathbf{B}_{ext} = 4\,\mathrm{T}||c$, and calculated values using Eqn. (A.1), $f_{ext} = 541.98\,\mathrm{MHz}$, and θ values that minimize $|f_{calc}(\theta) - f_{exp}(\theta)| + |f_{calc}(-\theta) - f_{exp}(-\theta)|$. Note that 541.14 MHz is listed twice in f_{exp}, as f^{-}_{E2} and f^{-}_{E3} overlap.

site	f^{ZF} [MHz]	f_{exp} [MHz]	θ [°]	f_{calc} [MHz]
E1	68.53	517.90 ± 0.01	-24.01	517.90
		573.26 ± 0.01	+24.01	573.30
E2	102.12	541.14 ± 0.01	-5.88	541.14
		561.62 ± 0.02	+5.88	561.71
E3	76.71	541.14 ± 0.01	-4.69	541.14
		553.54 ± 0.02	+4.69	553.56

A.2 Details on data taken in large external fields

The μSR spectra are analyzed over the first 1 µs [1] with the following models: Below 50 K, where f^{-}_{E2} and f^{-}_{E3} overlap, six components are considered; all three doublets share amplitude, and the overlapping line is fit to two components with the same phase and frequency, but share amplitude and relaxation rate with f^{+}_{E2} and f^{+}_{E3}, respectively. At and above 50 K, the data are fit to up to five exponentially damped oscillatory functions, with shared amplitudes for the E1 and E2 doublets, but separate relaxation rates.

Additionally, for the spectra at $T = 50,\ 110 - 155\,\mathrm{K}$, the amplitude of the E3′ component, see Fig. 5.5, is fixed to 0.0365, a value obtained by averaging over the amplitude of surrounding temperature points. This constraint is necessary in order to get a meaningful measure of the relaxation rate of this strongly damped component.

The fitted amplitudes of E1 and E2 are shown in Fig. A.1(a). The temperature dependence tracks largely the ZF behavior: E2 is constant in amplitude, and E1 starts to increase above 200 K.The displayed values are the amplitudes of one of the doublets; the total amplitude of muons in either E1 or E2 is twice that. The remaining amplitudes, associated with E3, E3′ and E3* are displayed in Fig. A.1(b). The points with a thick horizontal bar indicate temperature points where the amplitude was constrained. The E3 doublet amplitude accounts for only one of the doublets; the dashed line indicates the total (double) value for reference.

The frequencies obtained from fitting to five exponentially damped oscillatory components are shown in Table A.3. Using Eqn. (A.1), f_{calc} is calculated for the θ value that minimizes $|f_{calc}(\theta) - f_{exp}(\theta)| + |f_{calc}(-\theta) - f_{exp}(-\theta)|$, yielding very good agreement with the data, and θ values matching closely those obtained in low field, see Table A.1.

The temperature dependence of $f^{\pm}_{\mathrm{E1}}$ and $f^{\pm}_{\mathrm{E2}}$ is modeled by Eqn. (A.1) with θ from Table A.3, and

[1] A small sample misalignment of less than 1° seems to cause a further splitting of the line at times longer than 1 µs. This sub-splitting affects the various multiplet frequencies differently and has a small temperature dependence which is not fully understood. Limiting the analysis (and the depicted Fourier transform) to the first 1 µs effectively smooths out the substructure; however a separate relaxation rate for the E1 doublet is required and attributed to broadening caused by this misalignment sub-splitting.

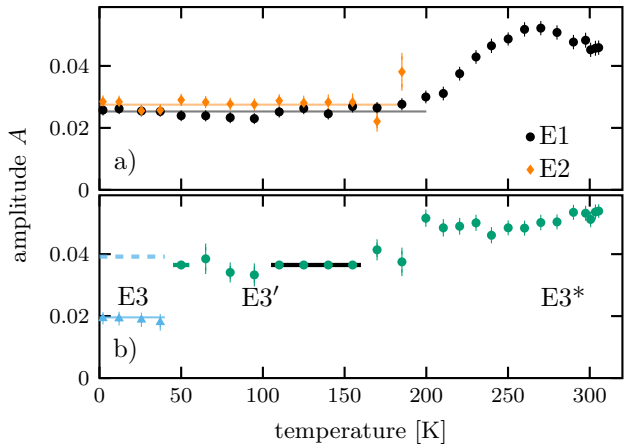

Figure A.1: Fit results for 4 T$||c$ spectra: amplitudes for (a) E1 and E2, and (b) for E3, E3′ and E3*. The black bar indicates that the value was fixed to 0.0365.

an interpolated temperature dependence of $f_{\mathrm{E1}}^{\mathrm{ZF}}(T)$ in Fig. 5.1(c). $f_{\mathrm{E2}}^{\mathrm{ZF}}(T)$ was further approximated by scaling $f_{\mathrm{E1}}^{\mathrm{ZF}}(T)$ by the low temperature E2/E1 frequency ratio $f_{\mathrm{E2}}^{\mathrm{ZF}}/f_{\mathrm{E1}}^{\mathrm{ZF}}|_{2.2\,\mathrm{K}} = 1.49$. The red lines in Fig. 5.6(c) represent the calculated doublet frequencies $f_{\mathrm{E1}}^{\pm}(T)$ and $f_{\mathrm{E2}}^{\pm}(T)$. There is good agreement with the data, indicating that θ is largely temperature independent. A small but consistent deviation from the predicted line is observed for the E1 doublet between $200-300\,\mathrm{K}$, and discussed in Sec. 5.6.

A.3 Details on the E2→E1 transition

Here we describe a model for the E2→E1 transition assuming a thermally activated, exponential rate of the form $\Lambda(T) = \nu_0 \exp(-E_a/k_B T)$, where E_a and ν_0 are activation energy and attempt frequency. The following expression describes the observable signal precessing at f_{E1} (compare [74, 284]):

$$\begin{aligned} S_{\mathrm{E1}}(t) &= A_{\mathrm{E1}} \cos(2\pi f_{\mathrm{E1}} t) \\ &+ A_{\mathrm{E2}} \int_0^t \Lambda \mathrm{e}^{-\Lambda t'} \cos\left(2\pi f_{\mathrm{E1}}(t-t') + 2\pi f_{\mathrm{E2}} t'\right) \mathrm{d}t' \\ &= \mathscr{A} \cos(2\pi f_{\mathrm{E1}} t + \Phi). \end{aligned} \tag{A.3}$$

Muons starting out in E1 are described by the first term, whereas the second describes the E2→E1 transition taking into account the phase acquired while evolving in E2. For $t \gg \Lambda^{-1}$, the resultant combined amplitude $\mathscr{A}$ and phase Φ can be expressed as

$$\mathscr{A} = \sqrt{\frac{A_{\mathrm{E2}}^2 + 2A_{\mathrm{E2}}A_{\mathrm{E1}}}{\zeta(T)^2+1} + A_{\mathrm{E1}}^2} \tag{A.4}$$

$$\Phi = -\arctan\left[\frac{A_{\mathrm{E2}}\zeta(T)}{A_{\mathrm{E2}} + A_{\mathrm{E1}}(1+\zeta(T)^2))}\right], \tag{A.5}$$

where

$$\zeta(T) = \frac{2\pi[f_{\mathrm{E1}}(T) - f_{\mathrm{E2}}(T)]}{\nu_0 \exp(-E_a/k_B T)}. \tag{A.6}$$

The expressions above assume that $\mathbf{B}_{int}$ in E1 and E2 are parallel and perpendicular to the initial spin polarization $\mathbf{P}_i$. In order to compare this model to data taken in both ZF and large $\mathbf{B}_{ext}$, small modifications, outlined below, are necessary.

In general, $\mathbf{B}$ is not perpendicular to the initial polarization $\mathbf{P}_i$, causing the component of $\mathbf{B}||\mathbf{P}_i$ to act as a holding field. The polarization signal can be decomposed into oscillating and non-oscillating components, see Eq. (2.6)

$$S(t) \propto \cos(\theta)^2 \cos\left(\gamma_\mu |\mathbf{B}| t\right) + \sin(\theta)^2; \tag{A.7}$$

note that here, we use $90° - \theta$ as the angle enclosed by $\mathbf{B}$ and $\mathbf{P}_i$.

Zero field. Here, $\mathbf{P}_i||c$, and for both E1 and E2, the internal field $\mathbf{B}_{int}$ encloses an angle θ with the c-plane, see Table A.1. Thus $\mathbf{B}_{int} \cdot \mathbf{P}_i \neq 0$, resulting in a non-oscillatory signal component.The oscillatory f_{E1} signal amplitude represents only a fraction of $\cos(\theta_{\mathrm{E1}} = 24°)^2 = 0.83$ of muons in E1, while for E2, $\cos(\theta_{\mathrm{E2}} = 6°)^2 = 0.99$, and virtually the complete E2 component is oscillating. Thus if the complete E2 component with observed amplitude A_{E2} coherently transfers to E1, the transferred amplitude observed at f_{E1} is only $(\cos(\theta_{\mathrm{E1}})/\cos(\theta_{\mathrm{E2}}))^2 A_{\mathrm{E2}}$. Strictly, this is only valid for $\Lambda^{-1} \ll 1/f_{\mathrm{E2}}$; furthermore, a change $\Delta\varphi = 30°$ of the internal field direction upon transition is neglected. A calculation addressing both issues was carried out and yielded slight improvements but no major deviations from the simple model, and was not included for clarity. The temperature dependence of $f_{\mathrm{E1}}^{\mathrm{ZF}}(T)$ and $f_{\mathrm{E2}}^{\mathrm{ZF}}(T)$ is obtained by interpolating $f_{\mathrm{E1}}^{\mathrm{ZF}}$ shown in Fig. 5.1 (c).

High field. As $\mathbf{B}_{ext} \perp \mathbf{P}_i > \mathbf{B}_{int}$, the resultant internal field is in good approximation perpendicular to $\mathbf{P}_i$. $\mathbf{B}_{ext}$ causes a frequency splitting, see Section 5.3.4. The doublet frequencies, compare red lines in Fig. 5.6, are given by Eqn. (A.1). Here, only transitions without sign change of θ, i.e. $f_{\mathrm{E2}}^{+} \rightarrow f_{\mathrm{E1}}^{+}$ and $f_{\mathrm{E2}}^{-} \rightarrow f_{\mathrm{E1}}^{-}$, are considered. Note that the phase shift Φ has opposite direction for the two doublet frequencies due to a sign change of ζ, see Eqns. (A.5) and (A.6). The model predicts slightly different temperature dependences $\mathscr{A}(T)$ for the $f_{\mathrm{E2}}^{+} \rightarrow f_{\mathrm{E1}}^{+}$ and $f_{\mathrm{E2}}^{-} \rightarrow f_{\mathrm{E1}}^{-}$ transitions. Since the experimental frequency doublet was fit to a common amplitude, the model curve shown in Fig. 5.7(b) is the average of both contributions.

For a quantitative analysis, the following parameters (as obtained in the Section 5.3) were used: in ZF, $A_{\mathrm{E1}} = 0.082$ and $A_{\mathrm{E2}} = 0.090$, in high field $A_{\mathrm{E1}} = 0.0253$ and $A_{\mathrm{E2}} = 0.0275$. The derivation of Eqns. (A.4) and (A.5) does not consider initial phases ($\phi_{\mathrm{E1}} = \phi_{\mathrm{E2}} = 0$). This was accounted for by shifting the model curves by the E1 initial phase obtained at low temperatures.